

GAS-PHASE SYNTHESIS OF SEMICONDUCTOR NANOCRYSTALS AND ITS  
APPLICATIONS

By

Rajib Mandal

A DISSERTATION

Submitted to  
Michigan State University  
in partial fulfillment of the requirements  
for the degree of

Mechanical Engineering–Doctor of Philosophy

2016

## ABSTRACT

### GAS-PHASE SYNTHESIS OF SEMICONDUCTOR NANOCRYSTALS AND ITS APPLICATIONS

By

Rajib Mandal

Luminescent nanomaterials is a newly emerging field that provides challenges not only to fundamental research but also to innovative technology in several areas such as electronics, photonics, nanotechnology, display, lighting, biomedical engineering and environmental control. These nanomaterials come in various forms, shapes and comprises of semiconductors, metals, oxides, and inorganic and organic polymers. Most importantly, these luminescent nanomaterials can have different properties owing to their size as compared to their bulk counterparts. Here we describe the use of plasmas in synthesis, modification, and deposition of semiconductor nanomaterials for luminescence applications.

Nanocrystalline silicon is widely known as an efficient and tunable optical emitter and is attracting great interest for applications in several areas. To date, however, luminescent silicon nanocrystals (NCs) have been used exclusively in traditional rigid devices. For the field to advance towards new and versatile applications for nanocrystal-based devices, there is a need to investigate whether these NCs can be used in flexible and stretchable devices. We show how the optical and structural/morphological properties of plasma-synthesized silicon nanocrystals (Si NCs) change when they are deposited on stretchable substrates made of polydimethylsiloxane (PDMS). Synthesis of these NCs was performed in a nonthermal, low-pressure gas phase plasma reactor. To our knowledge, this is the first demonstration of direct deposition of NCs onto stretchable substrates.

Additionally, in order to prevent oxidation and enhance the luminescence properties, a silicon nitride shell was grown around Si NCs. We have demonstrated surface nitridation of Si NCs in a single step process using non-thermal plasma in several schemes including a novel dual-plasma synthesis/shell growth process. These coated NCs exhibit  $\text{SiN}_x$  shells with composition depending on process parameters. While measurements including photoluminescence (PL), surface analysis, and defect identification indicate the shell is protective against oxidation compared to Si NCs without any shell growth.

Gallium Nitride (GaN) is one of the most well-known semiconductor material and the industry standard for fabricating LEDs. The problem is that epitaxial growth of high-quality GaN requires costly substrates (*e.g.* sapphire), high temperatures, and long processing times. Synthesizing freestanding NCs of GaN, on the other hand, could enable these novel device morphologies, as the NCs could be incorporated into devices without the requirements imposed by epitaxial GaN growth. Synthesis of GaN NCs was performed using a fully gas-phase process. Different sizes of crystalline GaN nanoparticles were produced indicating versatility of this gas-phase process. Elemental analysis using X-ray photoelectron spectroscopy (XPS) indicated a possible nitrogen deficiency in the NCs; addition of secondary plasma for surface treatment indicates improving stoichiometric ratio and points towards a unique method for creating high-quality GaN NCs with ultimate alloying and doping for full-spectrum luminescence.

Copyright by  
RAJIB MANDAL  
2016

*Dedicated to my beloved parents.....*

## ACKNOWLEDGMENTS

This dissertation is the result of all the help and support that I have received from all my professors, colleagues, lab mates, friends and family. Firstly, I thank my advisor, Professor Rebecca Anthony, for her constant encouragement, untiring help and invaluable suggestions. I am incredibly grateful for her guidance regarding both my professional and personal life. I would also like to thank all my committee members, Professor Andre Benard, Professor Junghoon Yeom and Professor Benjamin Levine for their time, fruitful discussions, and ideas regarding my dissertation.

Many thanks to Professor Richard Lunt from Chemical Engineering and Materials Science department for his invaluable suggestions and also for allowing me to use his instrument for my research. I would like to thank Professor Sara Roccabianca and Professor Rémi Beaulac for the helpful discussions and suggestions. My sincere thanks also go to Prof. John McCracken for helping us with EPR measurement.

These years of study were made much easier and extremely entertaining with the help and support of my lab mates at Plasmas and Nanomaterials Laboratory. I would also like to thank all the students from High Temperature and Plasma Lab at University of Minnesota for their help and advice with lab equipment and experimentation. Before starting our lab here, I got my first hands on experience with Plasma processing at High Temperature and Plasma Lab.

Many collaborators have helped me a great deal during my research project and I would like to specifically thank Karthik Padmanabhan, Ragnar Zhang, Peggy Young, and Pei Chen. I am extremely grateful to Dr. Per Askeland (The Composite Materials and Structures Center), Dr.

Xudong Fan (Center For Advanced Microscopy), Dr. Baokang Bi (W. M. Keck Microfabrication Facility) and Dr. Richard J. Staples (Center for Crystallographic Research) for their help and training with the characterization instruments. I am appreciative of the help and suggestions from Gregg Mulder (Electrical Engineering Shop) and Roy Bailiff (Mechanical Engineering Shop) during our experimental setup.

I would like to thank all my friends at Michigan State University for making my stay enjoyable, for all their support and encouragement. A special thanks to (Dr.) Pritha Dutta for being always there for me, for supporting me from day one and motivating me to succeed. Last but not the least; I want to thank my parents and sister for their unconditional love and support throughout my academics.

## TABLE OF CONTENTS

LIST OF TABLES.....	x
LIST OF FIGURES.....	xi
KEY TO SYMBOLS AND ABBREVIATIONS.....	xvi
CHAPTER 1.....	1
Introduction.....	1
1.1 Motivation for studying semiconductor nanocrystal based light emission.....	1
1.2 Different types of LEDs.....	3
1.3 Overview of Silicon Nanocrystals.....	4
1.4 Photoluminescence and Quantum Confinement.....	5
1.5 Outline of Presented Work.....	9
CHAPTER 2.....	12
Synthesis of Semiconductor Nanocrystals using Non-Thermal Plasma.....	12
2.1 Synthesis of Semiconductor Nanocrystals.....	12
2.2 Synthesis of Gallium Nitride (GaN) Nanocrystals.....	18
2.3 Nanoparticle Characterization.....	18
2.3.1 Scanning Electron Microscopy (SEM).....	19
2.3.2 Transmission Electron Microscopy (TEM).....	20
2.3.3 X-ray Diffraction (XRD).....	20
2.3.4 X-ray Photoelectron Spectroscopy (XPS).....	21
2.3.5 Photoluminescence Spectra and Quantum Yield (PL & QY).....	22
2.3.6 Fourier Transform Infrared Spectroscopy (FTIR).....	23
2.3.7 Raman Spectroscopy.....	23
2.3.8 Electron Paramagnetic Resonance (EPR).....	24
CHAPTER 3.....	25
Stretchable Luminescent films of Silicon Nanocrystals.....	25
3.1 Introduction.....	25
3.2 Experimental Details.....	26
3.3 Results and Discussions.....	29
3.4 Conclusions.....	41
CHAPTER 4.....	43
Gas-Phase Synthesis of Gallium Nitride (GaN) Nanocrystals using Non-Thermal Plasma Reactor.....	43
4.1 Introduction.....	43
4.2 Experimental Details.....	45
4.3 Results and Discussions.....	48

4.3.1 Transmission Electron Microscopy (TEM) Analysis .....	48
4.3.2 X-Ray Diffraction (XRD) Analysis .....	51
4.3.3 Raman Vibrational Spectroscopy .....	52
4.3.4 X-Ray Photoelectron Spectroscopy (XPS) Analysis .....	54
4.3.5 Fourier Transform Infrared Spectroscopy (FTIR) Analysis .....	57
4.3.6 Photoluminescence Spectra and Quantum Yield .....	59
4.3.7 Size-Tuning of GaN Nanocrystals using Plasma Reactor .....	60
4.4 Dual Plasma Synthesis .....	66
4.5 Conclusions .....	74
 CHAPTER 5 .....	 75
Surface Nitridation of Silicon Nanoparticles using a Non-Thermal Plasma .....	75
5.1 Introduction .....	75
5.2 Experimental Details .....	77
5.3 Results and Discussions .....	79
5.4 Dual Plasma Synthesis .....	91
5.5 Conclusions .....	101
 APPENDICES .....	 103
APPENDIX A: Collaborative Projects .....	104
APPENDIX B: Plasma-induced Crystallization of Gallium Nitride (GaN) Nanoparticles .....	112
APPENDIX C: Nucleation and Crystal Growth in Gas-Phase Process .....	117
 BIBLIOGRAPHY .....	 120

## LIST OF TABLES

Table 4.1 Physical properties of different crystal structure of GaN.....	51
Table 4.2 Composition analysis of GaN nanocrystals.....	57
Table 4.3: Residence Time Calculation.....	61
Table 4.4: Nanoparticle size distribution for different cases.....	64
Table 5.1: PL peak shifting data along with nanoparticle size for different samples.....	99

## LIST OF FIGURES

Figure 1.1: U.S. Electricity Consumption for Lighting by Sector and Lamp Type for the year 2010 (Adapted from the 2010 U.S. Lighting Market Characterization report <sup>3</sup> ).....	2
Figure 1.2: Luminous efficacy of different types of white light lamps over the years. (Adapted from Narukawa et al. <sup>4</sup> ).....	2
Figure 1.3: Band structure of bulk and nano silicon. (Adapted from Olivier Debieu Dissertation <sup>30</sup> ).....	5
Figure 1.4: Depiction of electrons from the conduction band recombining with the holes from the valance band of a semiconductor. (Adapted from Martin Wölz Dissertation <sup>33</sup> and E. Fred Schubert (Second Edition, 2006) <sup>34</sup> ).....	8
Figure 1.5: Band structure of a direct-bandgap semiconductor (GaN) showing electron-hole recombination in momentum space. (Adapted from Martin Wölz Dissertation <sup>33</sup> and E. Fred Schubert (Second Edition, 2006) <sup>34</sup> ).....	8
Figure 2.1: The Plasma Reactor (a) Schematic (b) Experimental setup.....	15
Figure 2.2: Photograph (Top View) and schematic of the matching network.....	16
Figure 2.3: Schlenk line setup for functionalization of Si NCs.....	17
Figure 2.4: Typical X– ray diffraction setup (Adapted from ref. 80).....	21
Figure 3.1: SEM image of a typical PDMS surface.....	27
Figure 3.2: Stretching stage coupled with the push rod.....	28
Figure 3.3: X-ray diffraction patterns from silicon nanoparticles.....	29
Figure 3.4: Raman vibrational spectroscopy from silicon nanoparticles.....	30
Figure 3.5: High resolution TEM images showing Si NCs.....	30
Figure 3.6: FTIR spectra from Si NCs.....	31
Figure 3.7: Photoluminescence spectra (a) different substrate (b) different stretching ratio of PDMS (c) different thickness of PDMS films.....	33
Figure 3.8: SEM images of Si NC films: (a) & (c) on Silicon wafer, (b) & (d) on PDMS.....	34

Figure 3.9: SEM images (Top-down view) of Si NC films on PDMS with different stretching ratio.....	35
Figure 3.10: Photoluminescence spectra from oxidation dependence experiment.....	37
Figure 3.11: Comparison of FTIR spectra analysis (a) sample from glove bag (b) sample from open air. Oxidation peak (Si-O-Si) is located at $\sim 1050\text{ cm}^{-1}$ . ....	38
Figure 3.12: (a) SEM images of a Si NC film on PDMS in different conditions, (b) a cartoon showing wrinkling formation in PDMS films.....	39
Figure 3.13: Oxidation dependence experiment with cartoon.....	40
Figure 3.14: Flowchart showing different steps of this experiment.....	41
Figure 4.1: The Plasma Reactor (a) Schematic (b) Photo of Experimental setup.....	46
Figure 4.2: Glass tubes with different dimensions used for the plasma reactor.....	47
Figure 4.3: TEM images of a cluster of GaN nanoparticles at different supplied power. (a) and (b) shows low level of crystallinity at 110W. (c) and (d) shows high level of crystallinity at 130W. The inset in (b) and (d) shows the SAED pattern.....	49
Figure 4.4: (b) FFT and (c) Profile plot of a Single crystal GaN from TEM image (a).....	50
Figure 4.5: XRD pattern from GaN NCs (with inset (A) from ref. 121,123 showing XRD pattern for zinc blende GaN NCs with similar range of nanoparticle size and inset (B) from ref. 124 showing XRD pattern of hexagonal GaN NCs with bigger size).....	52
Figure 4.6: Raman vibrational spectra of as-synthesized nanocrystalline GaN.....	53
Figure 4.7: X-ray photoelectron spectroscopy signals of (a) Ga-2p <sub>3/2</sub> (with inset from ref. 134 showing difference in Ga-2p peak position for GaN and Ga <sub>2</sub> O <sub>3</sub> in terms of binding energy) and (b) N-1s from the as produced GaN nanocrystals (with inset showing deconvolution of N-1s spectra using two Gaussian lineshapes, N-1s spectra is shown in orange and overall fit is shown in blue).....	55
Figure 4.8: X-ray photoelectron spectroscopy signals of Carbon (C-1s) and oxygen (O-1s).....	56
Figure 4.9: FTIR spectra from as-prepared GaN NCs (the inset image shows a possible configuration of GaN NCs).....	58
Figure 4.10: FTIR spectra from as-prepared GaN NCs (before and after heating).....	58
Figure 4.11: Absorption spectra from GaN NCs.....	60

Figure 4.12: TEM images of a cluster of GaN nanoparticles with Ar = 85 sccm, NH <sub>3</sub> = 95 sccm, TMGa = 2 sccm and 125W (150W) RF power (for Case 2). The inset is showing the selected-area electron diffraction (SAED) pattern.....	62
Figure 4.13: Nanoparticle size distribution (a) Case 1: Ar = 60 sccm, NH <sub>3</sub> = 65 sccm, TMGa = 1 sccm and 114W (130W) RF power; (b) Case 2: Ar = 85 sccm, NH <sub>3</sub> = 95 sccm, TMGa = 2 sccm and 125W (150W) RF power.....	63
Figure 4.14: XRD pattern from GaN NCs for (a) Case 1 and (b) Case 2 (with inset (A) from ref. 121,123 showing XRD pattern for zinc blende GaN NCs with similar range of nanoparticle size and inset (B) from ref. 124 showing XRD pattern of hexagonal GaN NCs with bigger size).....	66
Figure 4.15: Schematic of the dual plasma reactor for the synthesis of GaN NCs.....	67
Figure 4.16: XPS signals of Ga-2p <sub>3/2</sub> and N1s from as produced GaN NCs synthesized using straight tube dual (a) & (b) without N <sub>2</sub> through the side arm, (c) & (d) with 50 sccm N <sub>2</sub> through the side arm.....	69
Figure 4.17: TEM images of GaN NCs synthesized from dual plasma reactor with varying secondary plasma power: (a) & (b) 20W and (c) & (d) 40W. The inset in (b) and (d) shows the corresponding SAED pattern.....	71
Figure 4.18: EPR spectra from GaN NCs synthesized using Single Plasma and Dual Plasma.....	72
Figure 4.19: EPR spectra of Single Plasma synthesized GaN NCs at different temperatures.....	73
Figure 5.1: Schematic of the Plasma Reactor with (a) case 1 and (b) case 2.....	78
Figure 5.2: Comparison of FTIR spectra from Si nanoparticles (a) without any gas injection through the side arm, (b) 100 sccm H <sub>2</sub> through the side arm and (c) 100sccm N <sub>2</sub> through the side arm.....	80
Figure 5.3: Evolution of FTIR spectra for three different cases.....	81
Figure 5.4: Deconvolution of the FTIR spectra for Si-N-Si-HX stretching vibrations region using five Gaussian lineshapes for Si NCs synthesized using 120 sccm N <sub>2</sub> flown through the side arm for the plasma reactor shown in Figure 4.1 (b).....	82
Figure 5.5: FTIR spectra showing Si-N-Si stretching band for SiN <sub>x</sub> coated Si NCs.....	84
Figure 5.6: PL spectra from SiN <sub>x</sub> coated Si NCs synthesized with 100sccm of N <sub>2</sub> through the sidearm into the SiH <sub>4</sub> /Ar plasma.....	84
Figure 5.7: Evolution of PL peaks for different samples.....	86

Figure 5.8: XPS measurements of (a) & (b) SiNCs synthesized with 120 sccm of N <sub>2</sub> , (c) & (d) SiNCs without any additional gas injection.....	88
Figure 5.9: Schematic showing possible bonding configurations near a Si–N bond. (a) without hydrogen (SiN <sub>x</sub> group), and (b) with SiH and NH bonds (SiN <sub>x</sub> (H) group). (Adapted from Hasegawa et al. <sup>207</sup> ).....	89
Figure 5.10: TEM images of SiN <sub>x</sub> coated SiNCs synthesized with 120 sccm N <sub>2</sub> using reactor design shown in Figure 5.1(b). The inset shows the SAED pattern.....	89
Figure 5.11: Comparison of EPR signals from SiNCs with SiN <sub>x</sub> coated SiNCs. (Note: the signals were acquired under different microwave frequency, accounting for the large offset in magnetic field.).....	91
Figure 5.12: Schematics of the dual plasma reactor for (a) Case 1 and (b) Case 2.....	92
Figure 5.13: Comparison of FTIR spectra for two different reactor configurations.....	94
Figure 5.14: Comparison of FTIR spectra with different flow rates for case 1.....	95
Figure 5.15: XPS measurements of SiN <sub>x</sub> coated SiNCs from straight tube dual plasma (a) & (b) 50 sccm N <sub>2</sub> through the side arm, (c) & (d) 50 sccm N <sub>2</sub> with 10 sccm SiH <sub>4</sub> through the side arm.....	96
Figure 5.16: Evolution of PL peak for samples with varying N <sub>2</sub> flow rates.....	97
Figure 5.17: Evolution of PL peak for samples with different reactor configurations.....	98
Figure 5.18: Comparison of EPR spectra for three different samples.....	100
Figure A.1: (a) Photoluminescence spectra and (b) absorption spectra from three different types of SiNC films.....	106
Figure A.2: FTIR spectra from three different types of Si NC films.....	106
Figure A.3: SEM images of Octahedron Polymer Nanolattices on Si wafer: (a) and (b) before Si NC deposition, (c) and (d) after coated with Si NCs.....	108
Figure A.4: Flow chart diagram showing different steps of Deposition and Masking. (Figure Credit: Ryan Ng, Caltech).....	110
Figure A.5: Steps of surface functionalization of Si NCs with 1-decene <sup>49,58</sup> . (Figure Credit: Dr. Rebecca Anthony).....	111
Figure B.1: Effect of electron temperature on nanoparticle temperature.....	113

Figure B.2: Effect of ion density on nanoparticle temperature.....	114
Figure B.3: Effect of reactor pressure on nanoparticle temperature.....	114
Figure B.4: Effect of hydrogen density on nanoparticle temperature.....	115
Figure B.5: Effect of hydrogen density on the nanoparticle temperature. The ion density is the most important parameter; changing H <sub>2</sub> density did not make large changes in the nanoparticle temperature.....	116
Figure C.1: Gallium Nitride synthesis route (Adapted from Parikh et al. <sup>250</sup> ).....	118

## KEY TO SYMBOLS AND ABBREVIATIONS

kWh — kilowatt-hours

SSL — Solid-State Lighting

CFL — Compact Fluorescent Lamp

LED — Light Emitting Diode

nm — nanometer

TEM — Transmission Electron Microscopy

XRD — X-ray Diffraction

SEM — Scanning Electron Microscopy

FTIR — Fourier Transform Infrared Spectroscopy

XPS — X-ray Photoelectron Spectroscopy

PL — Photoluminescence

QY — Quantum Yield

EPR — Electron Paramagnetic Resonance

# CHAPTER 1

## Introduction

### 1.1 Motivation for studying semiconductor nanocrystal based light emission

Carbon-based energy sources are declining and energy cost is increasing day by day. The effect of this carbon based energy on our global climate is becoming clear. The average temperature of earth has increased due to the emission of greenhouse gas into the atmosphere mostly due to human activities. In order to curb the greenhouse gas emission and maintain our environment, the focus has shifted in using innovative technologies that are inexpensive and uses least possible energy. One of the major areas to look for reduction in energy is lighting technology. According to the U.S. Energy Administration (EIA)<sup>1</sup>, the electricity consumed by the residential and commercial sector of the United States for lighting purpose was approximately 412 billion kilowatt-hours (kWh) for the year 2014, which is approximately 15% of the total energy consumed by these sectors and represents 11% of the total electricity consumption in U.S. Therefore, developing efficient and clean lighting technology like solid-state lighting would not only save energy but also can have a huge impact in environment. The U.S. Department of Energy has a Research and Development (R&D) program specifically designed for Solid-State Lighting (SSL)<sup>2</sup>. Figure 1.1 shows the U.S. lighting electricity consumption by sector and lamp type in 2010<sup>3</sup>. With increased demand for light, the lighting stock has become more efficient over the past decade. This rise in efficacy is largely due to the major development in lighting technology over the years. The move from incandescent to compact fluorescent lamps (CFLs) has helped in achieving higher efficiency. Figure 1.2 shows a comparison study of luminous efficacy for different types of white light lamps<sup>4</sup>. Compared to incandescent lamps, both CFL and LED lamps has better performance. But, due to the presence

of toxic materials such as mercury in fluorescent bulbs, it would lead to disposal problems. On the contrary, LEDs can be made with non-toxic materials and could also be made smaller than the fluorescent and incandescent bulbs that too with higher efficiency.

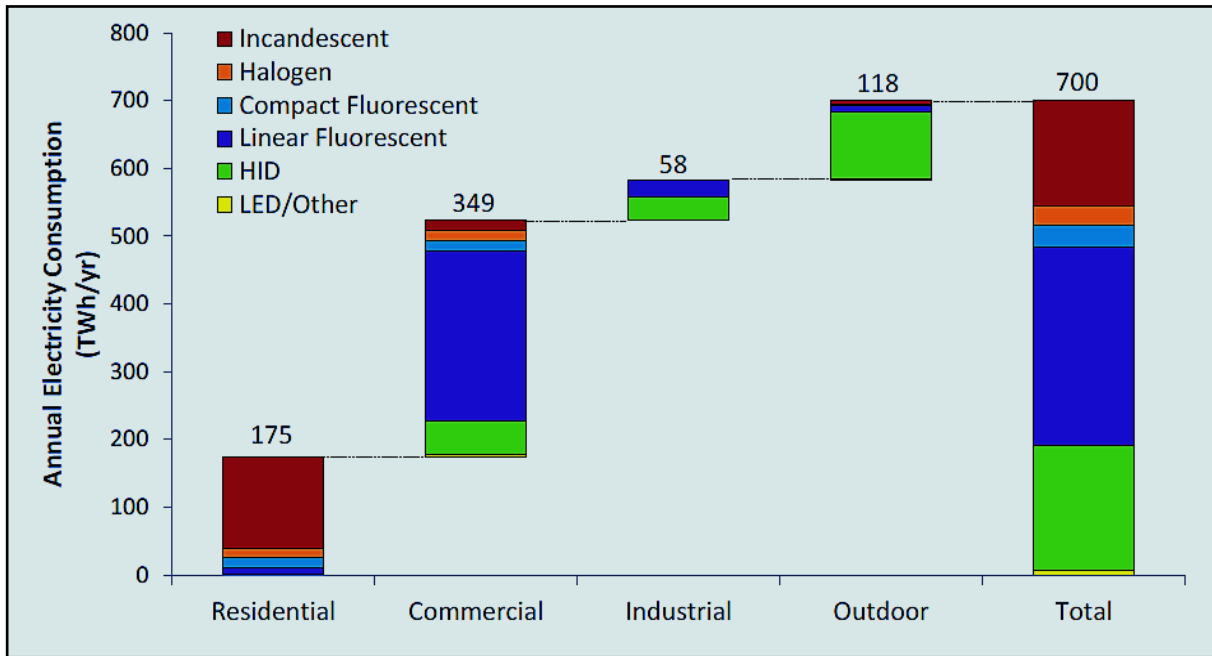


Figure 1.1: U.S. Electricity Consumption for Lighting by Sector and Lamp Type for the year 2010 (Adapted from the 2010 U.S. Lighting Market Characterization report<sup>3</sup>)

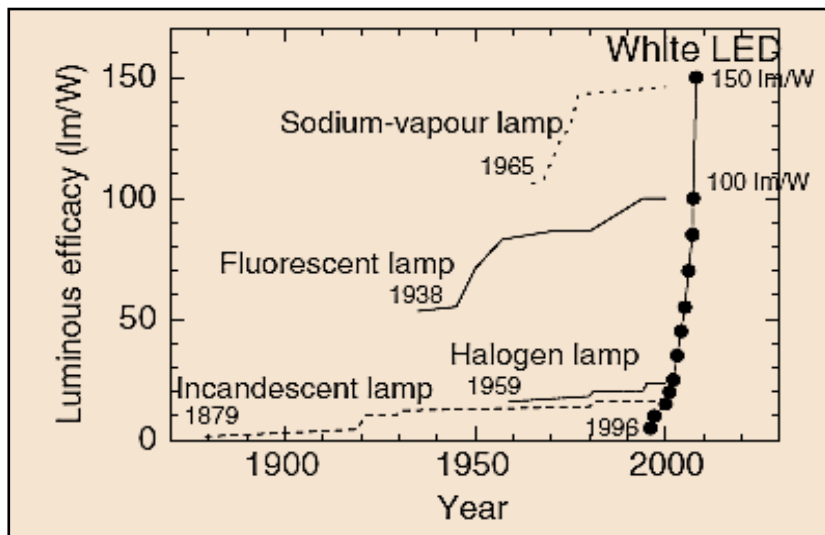


Figure 1.2: Luminous efficacy of different types of white light lamps over the years. (Adapted from Narukawa et al.<sup>4</sup>)

We have seen a significant growth of LED lighting over the last decade but we are yet to achieve its full potential and impact. To make it more penetrative and energy saving, this technology will need further research and marketing support.

## **1.2 Different types of LEDs**

There are mainly two types of LEDs based on the type of light-emitting materials used: inorganic and organic LEDs. Having potential for higher efficiency, longer lifetimes, exceptional control over color tuning, both organic and inorganic light-emitting diodes (LEDs) offer new dimensions for lighting technology. Being both economically and energy efficient, it would have more demand in our everyday lives. They do not necessarily contain any heavy metals and use of any toxic materials can also be avoided. The working principle of LEDs is that some materials (like semiconductor NCs, bulk inorganic materials etc.) can emit light when a voltage is applied across the device. Although conventional LEDs uses bulk semiconductor materials like gallium nitride (GaN) and gallium arsenide (GaAs) as the light emission source, these bulk materials have some spectral limitations. Furthermore, these bulk materials are hard to fabricate using thin or flexible substrates. In view of these limitations, the best alternative is to use films of organic molecules and inorganic semiconductor NCs.

Semiconductors can absorb and emit light at certain wavelengths based on its bandgap and the light emission process in this manner is referred to as electroluminescence. Silicon (Si) is one of the popular semiconductor materials and the basis for integrated circuits. Gallium arsenide (GaAs), aluminum gallium arsenide ( $\text{Al}_x\text{Ga}_{1-x}\text{As}$ ), gallium phosphide (GaP), and gallium arsenide phosphide ( $\text{GaAs}_x\text{P}_{1-x}$ )<sup>5-8</sup> were used as semiconductor materials for making first high-efficiency light emitting devices and its was done in 1960s . GaAs and AlGaAs based LED emit in the infrared wavelengths, ~850 nanometers (nm) while light in the green and red wavelengths<sup>9</sup> was

achieved by using GaP based LEDs. Efficient blue light LEDs started to appear in early 1990's and were based on III-nitride materials (such as aluminum nitride (AlN), gallium nitride (GaN), Indium Nitride (InN))<sup>10-13</sup>. Group IV nanomaterials like silicon have not been studied extensively for the purpose of making LEDs partly due to its indirect-bandgap nature. In addition, wet chemistry synthesis mechanisms was not that successful in terms of synthesizing narrowly size-dispersed Group IV NCs, although, some research have been done in the past decades on silicon in view of its application in LEDs<sup>14-16</sup>. In this thesis, we have studied gas-phase synthesis of silicon and GaN NCs along with surface modification in order to enhance their luminescence properties for applications in LEDs.

### **1.3 Overview of Silicon Nanocrystals**

Silicon is one of the most common semiconductor materials and has many advantages over the other semiconductor materials: inexpensive, nontoxicity, abundancies, and decades of experience in purification, growth and device fabrication. Bulk silicon is considered to be the main material of today's microelectronic<sup>17-19</sup>, photonics<sup>20-22</sup> and solar-photovoltaic<sup>23-26</sup> technologies. However, bulk crystalline silicon is not suitable for optoelectronic applications due to its indirect energy gap. By bringing down the size of silicon crystal to nanoscale levels, we can obtain new properties and functionalities. These Si NCs have opened the way for new and interesting applications in photovoltaic, photonic, microelectronic and nano-biotech industries<sup>27-29</sup>. These Si-NCs are fully compatible with the existing technologies and that makes them even more attractive. Hence, Si NCs have a huge technological and scientific interest. It is important to know the physical and chemical properties of Si NCs, its production methods, applications and characterization.

## 1.4 Photoluminescence and Quantum Confinement

Optical properties of Si NCs came into limelight and became an important research topic when the luminescence from Si NCs was realized. Various models have been used to explain the luminescence mechanism of Si NCs, including quantum confinement, surface states, defects in silicon oxide, and others. Among these, quantum confinement is the most generally accepted theory that accurately describes the size-tunable luminescence from silicon nanostructures.

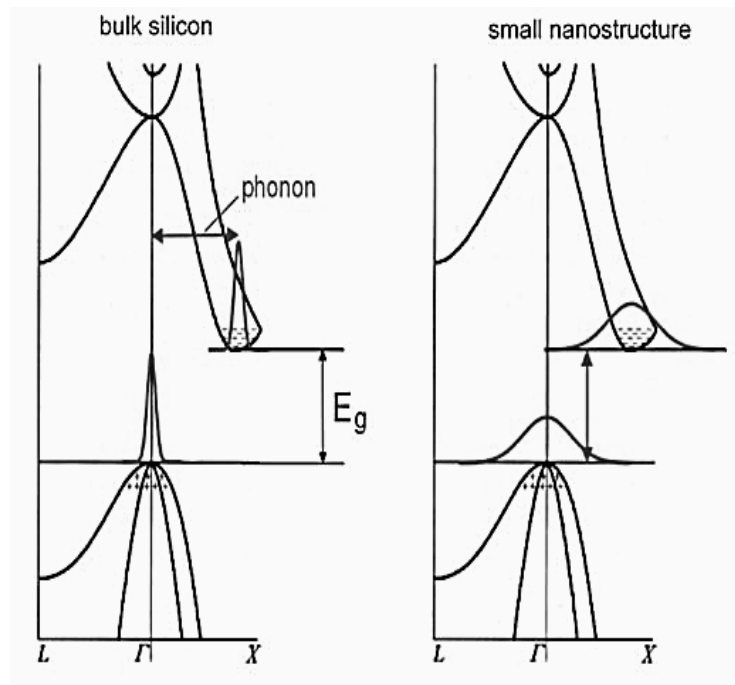


Figure 1.3: Band structure of bulk and nano silicon. (Adapted from Olivier Debieu Dissertation<sup>30</sup>)

The quantum confinement model was first proposed by Canham<sup>31</sup> in 1990 while explaining the visible PL from porous silicon. This principle is explained in the above Fig.1.3. When the structure size becomes very small, comparable to its Bohr radius ( $\sim 5$  nm for silicon), excitons (electron/hole pairs) generated by light gets trapped into a quantum well. The discrete energy levels can be calculated using the Schrödinger equation, where energies are inversely

proportional to the square of the width of the well, i.e. the nanoparticle size: the smaller the nanoparticle, the higher the band gap energy. The first approach was given by calculating the energy levels of a spherical quantum well using the approximation of effective mass<sup>30</sup>,

$$E(d) = E_0 + \frac{\hbar^2 \pi^2}{2d^2} \left( \frac{1}{m_e^*} + \frac{1}{m_h^*} \right) - \frac{1.8e^2}{\epsilon_i d} \quad (1.1)$$

where  $d$  represents the nanoparticle diameter in nm,  $m_e^*$  and  $m_h^*$  represents the electron and hole masses respectively;  $e$  denotes the electron charge,  $\epsilon_i$  is the electric permittivity of Si, and  $E_0$  represents the band gap of bulk Si. The last term in the Eq. (1.1) represents the Coulomb interaction energy between electron and hole. Due to the space confinement, wave vectors have become broadened and the band structure acts like direct, i.e. a phonon is not needed for radiative relaxation. The chances of radiative transitions increase and therefore it is more efficient. The consequences of quantum confinement are as follows: band gap widens and emission intensities rise with increased confinement.

From the Eq. (1.1), it can be seen that the band gap energy of nc-Si is inversely proportional with the particle diameter. This trend has also been found in experiments and thus the theory of quantum confinement is verified. However, luminescence from silicon involves many aspects aside from quantum confinement, including surface effects and competing radiative and non-radiative exciton decay pathways. For example, it has been observed that luminescence is reduced considerably due to the presence of dangling bonds at the nc-Si<sup>32</sup> surface as these dangling bonds does not allow radiative recombination to occur. It is also known that if hydrogen and/or oxygen atoms are present in the nc-Si surface or surroundings, they contribute a lot in passivation of the dangling bonds and eventually in increasing the PL intensity.

There are several other models/theories that have arisen for explaining the PL of Si NCs from several experimental results. The possible alternate model/theories are radiative surface states and interface states, the radiative and non-radiative defects, effect of compression, hydrogenated amorphous silicon, surface hydrides (Si-H<sub>x</sub>) etc<sup>30</sup>. However, the most likely accurate theory is the quantum confinement model by Canham<sup>30</sup>. This model explained the relation of nanoparticle size and its luminescence, broad PL spectra and the dependency of emission energy on the luminescence life-time.

Unlike silicon, which possesses an indirect bandgap (nano silicon acts more like a direct band gap semiconductor); GaN is a direct bandgap semiconductor material and therefore, its light emission mechanism is different from that of silicon. According to Pauli principle, the presence of an occupied state in the conduction band and an unoccupied state in the valance band (known as holes) is required for the PL process<sup>33</sup>. Emission of a photon occurs when these electrons and holes recombine and recombinations could be of two types: radiative and non-radiative.

Radiative recombination occurs when an electron in the conduction band annihilates a hole in the valance band and releases the excess energy in the form of a photon. The possibility of radiative recombination of electrons and holes depends on the band structure of a semiconductor. In order to have radiative recombination, the electron and hole have to be very close so that their wave functions can overlap spatially (shown by the arrows in Figure 1.4)<sup>33</sup>. Figure 1.5 showed the dispersion relation of electrons and holes and it is parabolic in nature similar to a free electron<sup>33</sup>. For direct-bandgap material like GaN, electrons will be thermally equilibrated to the valance band minimum and similarly for holes with the conduction band maximum<sup>33</sup>. In direct band-gap, the emitted photons have negligible momentum ( $k$ ) and

therefore both electrons and holes have a common  $k$  according to momentum conservation. While for silicon, which has indirect band-gap, emission of photon is rare and has to be accompanied by phonon-assisted momentum transfer. Although, silicon nanocrystal (Si NC) acts as a direct bandgap semiconductor due to the overlap of wave functions as shown in Figure 1.3. These Si NCs exploit the effects of quantum confinement due to its small size comparable to wavelengths of electrons.

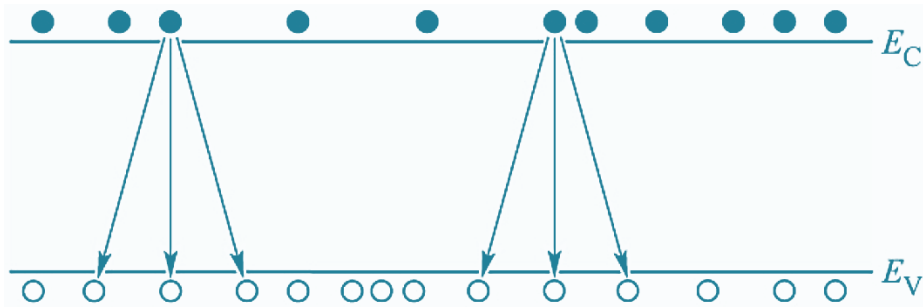


Figure 1.4: Depiction of electrons from the conduction band recombining with the holes from the valance band of a semiconductor.(Adapted from Martin Wölz Dissertation<sup>33</sup> and E. Fred Schubert (Second Edition, 2006)<sup>34</sup> )

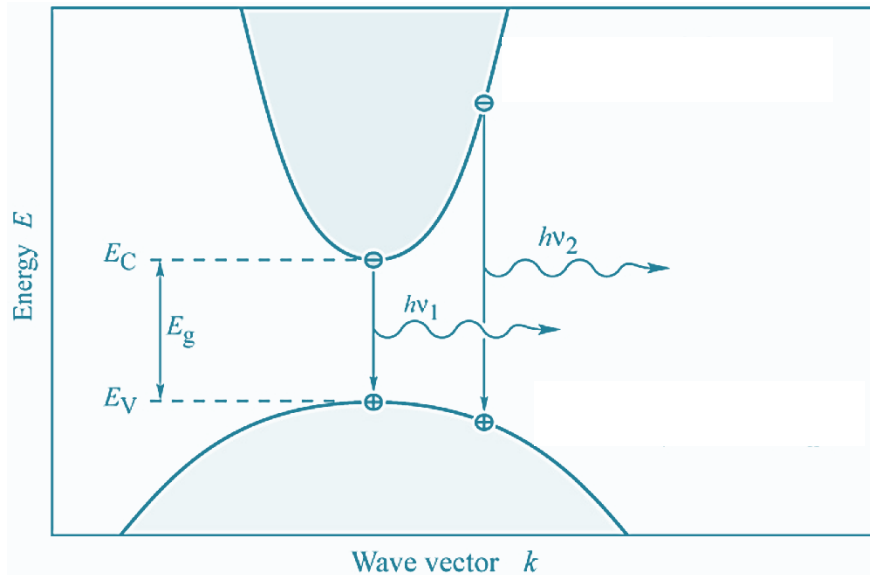


Figure 1.5: Band structure of a direct-bandgap semiconductor (GaN) showing electron-hole recombination in momentum space. (Adapted from Martin Wölz Dissertation<sup>33</sup> and E. Fred Schubert (Second Edition, 2006)<sup>34</sup> )

## 1.5 Outline of Presented Work

This thesis studies the different aspects of semiconductor nanomaterials (specifically, Silicon and Gallium Nitride), starting from its fabrication using a fully gas-phase process, treatment factors relating to enhance PL intensity, applications for stretchable devices (mainly LEDs) etc.

Chapter 2 provides the detailed information about synthesis of silicon nanoparticles using non-thermal plasma and a fully gas-phase process. We will talk about certain advantages of non-thermal plasma and gas-phase synthesis process over other available processes for silicon and gallium nitride (GaN) nanoparticle synthesis. We will also explain the liquid-phase surface functionalization process for SiNCs with 1-decene to improve their quantum yield, which will be used to prepare NCs for device fabrication (LEDs). Finally, we will talk about different kinds of characterization techniques used throughout this thesis along with its brief working principle to give a better understanding of these characterization schemes and its usefulness in characterizing our samples.

In Chapter 3, luminescent stretchable films of SiNCs are discussed. We have demonstrated the first all-gas-phase deposition of luminescent NCs onto elastomeric substrates (polydimethylsiloxane, PDMS). The films show wrinkling in response to pre-stretch of the PDMS substrates, as well as structural changes compared to SiNCs deposited on Si wafers. The SiNCs on relaxed PDMS exhibit blueshifted luminescence compared to SiNCs on Si wafer, with decreased blueshifting observed for the wrinkled SiNC films which had been deposited on prestretched PDMS. Our experiments confirm that the blueshifting effect is due to enhanced oxidation on PDMS, caused by the air-permeability of PDMS and thus oxidation of the SiNC films from all sides as opposed to the top-down-only oxidation that occurs for SiNCs on Si

wafers. This work has been submitted to the journal *ACS Applied Materials and Interfaces* with the title “Aging of Silicon Nanocrystals on Elastomer Substrates: Photoluminescence Effects”.

In Chapter 4, we have successfully performed non-thermal plasma synthesis of GaN nanocrystals (GaN NCs) in a fully gas-phase mode. Trimethyl gallium (TMGa) was used as gallium precursor and ammonia (NH<sub>3</sub>) as nitrogen precursor along with argon as the background gas. By performing a parametric study with different combination of flowrates and RF power, we successfully synthesized crystalline GaN nanoparticles. These nanoparticles were thoroughly characterized by Transmission Electron Microscopy (TEM), X-Ray diffraction (XRD), Raman spectroscopy, X-ray photoelectron spectroscopy (XPS), Fourier Transform Infrared Spectroscopy (FTIR), PL measurement and found out to be hexagonal GaN NCs with stoichiometric ratio of 1.4:1 (Ga:N). We have discussed some additional studies that are in progress to achieve proper stoichiometric (1:1) GaN NCs. To prove the versatility of this process, different sizes of NCs were produced just by changing the reactor geometry and gas flow rates. This process will hopefully expand the range of substrates that can be used for GaN synthesis. We are preparing this work for submission to *Nano Letters* under the title “Gas-Phase Synthesis of GaN Nanocrystals using Non-Thermal Plasma”.

Chapter 5 describes surface nitridation of SiNCs in a single step process using non-thermal plasma. Oxidation can introduce dangling bond defects in SiNCs and also cause a PL shift. In an attempt to prevent the oxidation of Si NCs and to enhance its luminescence properties, we have tried to grow a shell of silicon nitride around SiNCs. Upon successful synthesis, these NCs can be used for different applications like lithium-ion batteries, solar cells, LEDs etc. By means of a series of experiments which involved different reactor configurations, RF power, location of N<sub>2</sub> injection, electrode positioning, N<sub>2</sub> flowrate, we confirmed that

maximum PL and minimum oxidation occurs when these nanocrystal are synthesized using a dual plasma process with N<sub>2</sub> gas being injected in between two plasmas. These NCs were characterized thoroughly using FTIR, XPS, TEM, PL measurement and found out to be oxidized when exposed to atmosphere that led to the decrease of Si NC core size (~ 0.6 nm decrease in NC core diameter over a period of 1 month). In order to prevent the oxidation, a critical thickness of SiN<sub>x</sub> layer is to be achieved. We have discussed some on-going work in order to achieve this critical thickness. This work will be submitted to the journal *ACS Applied Materials and Interfaces* with the title “Surface Nitridation of Silicon nanocrystals in a Single Step process using Non–Thermal Plasma”.

## CHAPTER 2

### Synthesis of Semiconductor Nanocrystals using Non-Thermal Plasma

#### 2.1 Synthesis of Silicon Nanocrystals

Synthesis techniques for SiNCs are diverse and result in a range of nanostructure features like crystallinity, dangling bond density and surface termination. Starting with the liquid-phase reactions like thermal degradation of diphenylsilane<sup>35</sup>, and chemical reactions such as the reaction of silicon based salts with other compounds<sup>36</sup>, which have achieved great success in synthesizing luminescent Si NCs. Several studies have been reported on aerosol techniques for the synthesis of Si NCs, such as laser and thermal deposition/decomposition of silane<sup>37-40</sup>, ion implantation or plasma-enhanced chemical vapor deposition (PECVD) of SiO<sub>x</sub>/Si films with subsequent annealing<sup>41-43</sup> and atmospheric pressure plasma synthesis<sup>44-46</sup>. Although these methods can be useful for making Si NCs, they have certain limitations. In case of atmospheric-pressure synthesis methods, for example, laser pyrolysis, the size distribution of the nanoparticles were typically wide (~ 2–120 nm, lognormal size distribution)<sup>47,48</sup> which needs to be narrowed down after synthesis in order to effectively use it as light-emitters in wavelength-specific applications. Additionally, there is often oxidation of the nanocrystal surface that can affect its optoelectronic properties, hamper further processing and typically require another process to remove the oxide layer.

Another synthesis route is via plasma reactions. A plasma reactor can be designed in such a way that only constitutive elements will come into contact with the emerging nanoparticles, except protective and inert gases. This enables the production of high quality pure nanoparticles which is a very important prerequisite specifically for semiconductor applications. For example, in contrast to the above described laser pyrolysis, SiNCs can be formed in plasmas without any

oxide growth. Besides, using the gas phase synthesis, sizes can be controlled accurately with adjustable particle structure and the surface will be hydride-terminated which allows this process to be flexible in post-synthesis processing routes<sup>49</sup>. Another advantage is that the nanoparticles, which are coming out from the plasma, have a lesser degree of agglomeration compared to other methods as all the nanoparticles are negatively charged. Non-thermal plasmas has a broader operational window for nanoparticle synthesis as it can operate at low pressure as well as atmospheric pressures<sup>46,50–53</sup>. Prevention of oxidation of as-produced silicon nanoparticle surfaces can be done just by storing them in a nitrogen-purged glove box. In this way, it is possible to preserve the Si NC core as well as its surface which has a native hydride coverage that will definitely help in doing wet-chemistry functionalization of these NCs.

Synthesis of Si NCs (diameter < 10 nm) using plasmas have been studied thoroughly since early 1990s owing to its major application in several areas<sup>53</sup>, although most of the studies from early 1990s were based on the detrimental effects of plasma on silicon thin films. The Kortshagen group<sup>50,54</sup> was one of few who have synthesized Si NCs for application purpose and they used a continuous flow non-thermal plasma for that purpose. Nanoparticle heating inside the plasma was modelled by Mangolini et al.<sup>55</sup> and detailed analysis of plasma-induced crystallization mechanism for SiNCs was performed by Kramer et al<sup>56</sup>. Defect free NCs are really important for application purposes and Pereira et al.<sup>57</sup> have studied the defect control for freestanding SiNCs produced from non-thermal plasma. Liquid-phase surface passivation of as-produced Si NCs was performed by Mangolini et al.<sup>58</sup> and photoluminescence quantum yields (PL QY) of ~ 60–70% were achieved. Effect of power on the level of crystallinity for SiNCs was carried out by Anthony et al<sup>59</sup>. The Kortshagen group<sup>60,61</sup> has also studied the gas-phase surface passivation of SiNCs and an all-gas-phase approach for the fabrication of SiNC based Light-

Emitting Diodes (LEDs). Gas-phase hydrosilylation of plasma-synthesized SiNCs were also performed by Agarwal Group<sup>62</sup>. Agarwal et al.<sup>63</sup> have done a measurement study of absolute radical densities in plasma using mass spectrometry. Plasmonic properties of boron and phosphorus doped SiNCs were analyzed by Kramer et al<sup>64</sup> and Zhou et al<sup>65</sup>. For colloidal stability and doping of SiNCs, Wheeler et al<sup>66</sup> has performed a study on hypervalent surface interactions.

This low-pressure non-thermal plasma has been extensively studied not only for SiNCs but also for germanium nanocrystals (Ge NCs)<sup>67</sup>, compounds like indium phosphide<sup>68</sup> and gallium nitride<sup>69</sup>, and also for alloys i.e. silicon-germanium nanoparticles<sup>70</sup>. Holman et al.<sup>67,71</sup> have studied size-controllability, monodispersity and the effect of impaction on film thickness for Ge NCs produced from non-thermal plasma. A numerical study was performed by Le Picard et al.<sup>53</sup> to understand the synthesis of SiNCs in radio frequency (RF) low-pressure plasma and also investigated the mechanism of particle growth.

Atmospheric plasma synthesis is also a very powerful tool for nanocrystal synthesis. Sankaran et al.<sup>46</sup> have synthesized blue luminescent silicon nanoparticles (SiNP) using atmospheric-pressure microdischarges. Microplasma was also used by Nozaki et al<sup>44,72</sup> and Wu et al<sup>73</sup> for the synthesis of tunable luminescent SiNCs and water-soluble SiNCs respectively. Atmospheric plasma has also been used for the synthesis of zinc oxide nanocrystals (ZnO NCs)<sup>74</sup>. Here, we use a low-pressure nonthermal plasma reactor for the synthesis of Si NCs and GaN NCs.

The schematic diagram of the plasma reactor for SiNC synthesis is shown in Fig. 2.1. This model of the reactor was developed by Elijah Thimsen and Lorenzo Mangolini of the

Kortshagen Group at the University of Minnesota in 2005 and has been well-studied<sup>50,59,75,76</sup>. The flow-through reactor consists of a Pyrex tube with an Outer Diameter (O.D.) of 12.7mm in the top portion and 25.4mm in the bottom portion. The tube is 304.8mm long and the expansion area is 177.8mm from the top. Argon and Silane (1% in Argon) are flown through the quartz tube and a pair of ring copper electrodes is wrapped around the tube. The position of the ring electrodes are such that the bottom edge of the ground electrode will be 2cm above from the starting of the expansion region. The thickness of the electrodes is around 1cm and the distance between the inside edges of the electrodes is 1.5cm. The upstream pressure was in the range of 1.85–2.7 Torr with downstream pressure being 160–300 mTorr (with the flowrates of Ar = 5–30 standard cubic centimeters per minute (sccm) and SiH<sub>4</sub> (1% bal. Ar) = 50–80 sccm) and can be kept constant using an orifice plate. The bottom electrode is grounded and the upper one is connected to 13.56 MHz radiofrequency (rf) power supply via an impedance matching network. The matching network has been assembled in our lab, and is depicted in Figure 2.2.

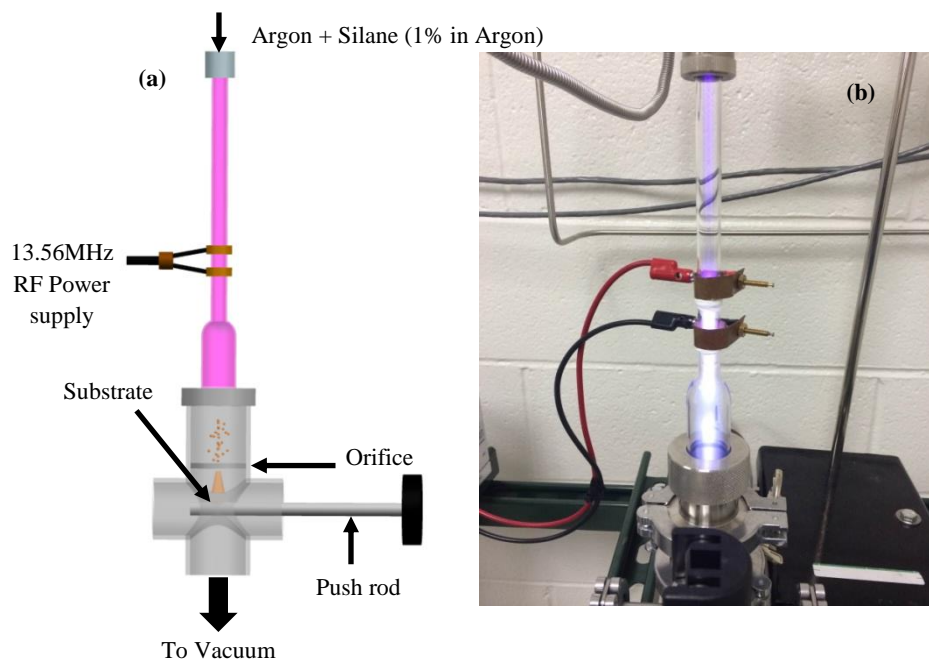


Figure 2.1: The Plasma Reactor (a) Schematic (b) Experimental setup.

The rf power excites plasma in the tube and dissociates the silane which leads to the nucleation and growth of Si nanoparticles. For most of the experiments the Si NCs are collected on substrates via the inertial impaction technique<sup>71</sup>. Except for air-sensitive measurements, these samples were kept in open air environment. For surface functionalization of as-produced Si NCs, nanoparticles were collected on stainless steel mesh via diffusion and kept under nitrogen environment.

There are several parameters which are responsible for the growth and crystallinity of the synthesized SiNCs, such as, supplied power, mass flow rate, pressure and temperature. We have used different combination of flow rates of Argon and Silane. Two different pressure gauges have been used, one at upstream of the slit-shaped orifice (Range: 10 Torr) and the other one at the downstream of that orifice (Range: 1 Torr). At first, we did a power study by keeping all other properties constant to find out the optimized power for the system as it is known that the overall crystallinity of the ensemble of collected nanoparticles depends on power<sup>59</sup>. After studying a power range from 15–60 W, we found that 25W is the optimum power that produces crystalline silicon nanoparticles. Crystallinity has been verified with XRD, TEM, and Raman Spectroscopy.

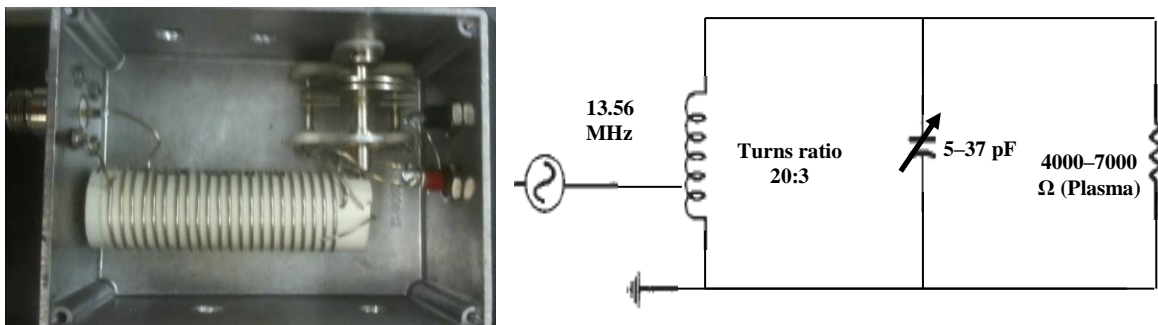


Figure 2.2: Photograph (Top View) and schematic of the matching network.

In order to achieve higher quantum yield from these Si NCs, liquid-phase surface-functionalization was performed using a thermal hydrosilylation reaction<sup>58,77</sup>. For this purpose, we have collected the NCs onto a stainless steel mesh and then immediately transferred to a nitrogen-purged glove box to avoid any oxidation. Inside the glove box, these filters with Si NCs were kept in vials sealed with rubber septum. When we were ready to start the functionalization process, we took out the sealed vials and put it under the N<sub>2</sub> line using a Schlenk line to avoid any oxidation. The functionalization solution is prepared by mixing mesitylene and 1-decene in 5:1 volume/volume ratio. This solution was then degassed and dried by putting some molecular sieves (size 4Å) into it and heating it at 50<sup>0</sup>C under the N<sub>2</sub> environment for 30 mins. Mass of the NCs were ~ 10 mg and to make it 1:1 (mass/volume) ratio for SiNCs: functionalization solution, we transferred 10 ml of functionalized solution into the vial using the Schlenk line. Then, we sonicated the vial containing NCs and solution for 5-10 mins so that it mixes properly. After that, we transferred the solution into a prepared bulb and refluxer tube setup which was being placed in a sandbath heater. Figure 2.3 is showing our functionalization setup including Schlenk line.



Figure 2.3: Schlenk line setup for functionalization of Si NCs.

We heated the sample at 170<sup>0</sup>C (based on 1-decene boiling point temperature) under N<sub>2</sub> flow and it took approximately 2 hours to complete the reaction indicated by formation of a clear solution. During the course of the reaction, cold water was flown through the refluxer tube to recondense the evaporated solvents so that the solution does not dry out. This thermal hydrosilylation process has been used extensively for silicon surfaces<sup>78</sup> and has been described for plasma-produced SiNCs<sup>77</sup>.

## **2.2 Synthesis of Gallium Nitride (GaN) Nanocrystals**

A low-pressure nonthermal plasma reactor has also been used for the synthesis of GaN NCs. The reactor geometry and dimensions are different than the SiNC reactor but the principle is the same. We have used trimethylgallium ((CH<sub>3</sub>)<sub>3</sub>Ga, TMGa) as Gallium (Ga) precursor, ammonia (NH<sub>3</sub>) as nitrogen source, and argon (Ar) as a background gas. Power was supplied from a RF power source via a matching network to the electrodes which excited the plasma causing the precursor to dissociate. These precursor fragments then grouped together and grew to form nanoparticles. We will talk about the detailed synthesis process for GaN NCs in Chapter 4.

## **2.3 Nanoparticle Characterization**

The nanoparticles are really important owing to their applicability in vast areas and they are normally divided into two categories: engineered and nonengineered<sup>79</sup>. Engineered particles are the one which are created or produced according to our needs by following a standard procedure. They could be the final products (like quantum dots) or some intermediate products depending on the application purpose. On the contrary, nonengineered nanoparticles could either be produced by nature or are created without any intent. Depending on the application area, nanoparticles can exist in various forms, for example, aerosols, colloids, nanocomposites, nanopowders etc. In this thesis, we have synthesized Si NCs and GaN NCs using a gas-phase

process in view of application in several areas and these NCs definitely falls under the category of engineered nanoparticles.

Due to their small size, these nanoparticles have different properties as compared to their bulk counterparts and also have surface dependent material properties due to extremely high surface area to volume ratio. There are several types of characterization techniques available and few are listed below (in brackets showing the characterization techniques used for our study).

- Optical (Imaging) Probe Characterization Techniques
- Electron Probe Characterization Techniques ( SEM, TEM)
- Scanning Probe Characterization Techniques (AFM)
- Photon(Spectroscopic) Probe Characterization ( Photoluminescence)
- Ion-Particle Probe Characterization Techniques (Raman Spectroscopy, XRD, EDX )
- Thermodynamic Characterization Techniques

### **2.3.1 Scanning Electron Microscopy (SEM)**

SEM is an electron microscope which creates images of samples by scanning it with a focused beam of electrons. The basic principle is that a beam of electrons strikes the sample surface and after interaction with the sample atoms, it generates signals. These generated signals are typically secondary electrons, back scattered electrons and characteristics X-rays and gives us important information regarding the sample's surface topography, composition, etc. The SEM operates in three different modes: primary (high resolution; secondary electron imaging), secondary (elemental composition analysis by EDX; Characteristic X-Rays) and Tertiary (elemental composition of sample; back-scattered electronic images).

We have used a Carl Zeiss Auriga Dual Column FIB SEM at the Composite Materials & Structures Center (CMSC), MSU. Surface structures, sample porosity, film thickness and sample composition were verified using SEM. One of the major drawbacks of this method is that the sample must be a good conductor at the surface for high image quality. SEM can give some valuable information regarding the purity and degree of aggregation.

### **2.3.2 Transmission Electron Microscopy (TEM)**

TEM is a high magnification imaging technique where a beam of electrons transmits through the sample and gives us important information regarding the sample's crystallographic structure in atomic scale. The basic principle of TEM is that a high energy beam of electrons impinges on a very thin sample—electrons are transmitted through the sample, scattering off of features and providing an atomic-scale image. TEM is the preferred method for the measurement of nanoparticle size, grain size along with overall size distribution, and of crystallinity of nanoparticles.

A JEOL 2200FS ultra-high resolution transmission electron microscope from Center for Advanced Microscopy, MSU was used for our project. Selected Area Electron Diffraction (SAED) is a TEM technique which can be used to obtain the diffraction patterns resulting from the electron beam scattered by the sample lattice. Dr. Xudong Fan helped us in performing TEM analysis for our samples. Special thanks to Alborz for helping us with few TEM analyses.

### **2.3.3 X-ray Diffraction (XRD)**

XRD can be used to obtain several characteristics of the single crystal or polycrystalline materials using the principle of Bragg's Law. In this technique, a parallel beam of monochromatic x-rays hits the sample (sample could either be on a fixed stage or on a rotating stage for averaging purpose) and the gets diffracted from the sample surface at some specific

angle as the atomic lattice works as a three dimensional diffraction grating. The diffraction pattern gives us important information regarding the sample in terms of diffracted beam position (angles) and its corresponding intensities. We can find out the interplanar atomic spacings (d-spacings) from the angles and the intensity coupled with the angles is very useful in identifying the crystalline material or compound. We can also figure out the crystal orientation from the position of those diffracted peaks and crystallite size in the sample can be calculated from the width of the diffracted peaks.

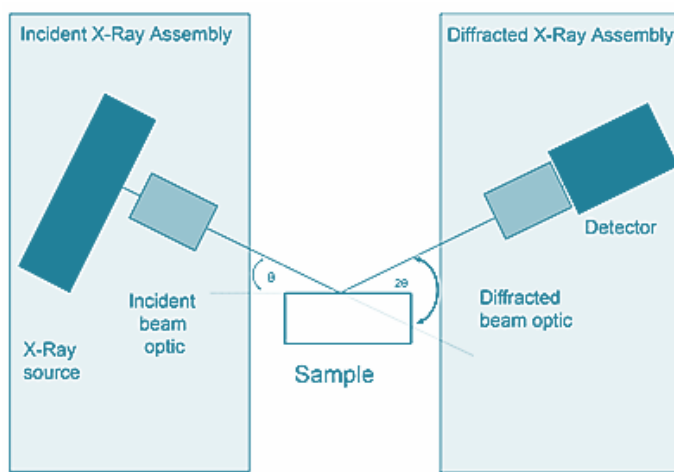


Figure 2.4: Typical X– ray diffraction setup (Adapted from ref. 80).

A Bruker Davinci Diffractometer from the Center of Crystallographic Research, MSU was used for the characterization of our samples. For our samples, which are in film format, a larger volume of sample was required to get proper signals.

#### 2.3.4 X–ray Photoelectron Spectroscopy (XPS)

XPS is a widely known surface characterization technique that can analyze a sample to a depth of 2 – 5 nm. We can get the information about which chemical elements are present near the surface and what is the nature of chemical bonds that exist between these elements. XPS works on the photoemission principle which states that when an x – ray bombards a sample,

some electrons become excited enough to escape the atom<sup>81</sup>. Irradiating a sample with x-rays of adequate energy excites the electrons in specific bound states. Once these photo-ejected electrons are in the vacuum, an electron analyzer will collect them and will measure their kinetic energy. This electron analyzer will create an energy spectrum of intensity (number of photo-ejected electrons vs time) vs binding energy (the energy of the electrons before they left the atom). Elemental analysis can be performed as each prominent energy peak corresponds to a specific element. Therefore, by integrating the area under each peak, we can get an idea about the composition percentage of the sample surface as each peak area is proportional to the total number of atoms present in each element.

A Perkin Elmer Phi 5600 ESCA system from CMSC, MSU was used for XPS analysis with magnesium  $K\alpha$  X-ray source at a take-off angle of  $45^\circ$ . Dr. Per Askeland helped us in performing XPS analysis for our samples.

### **2.3.5 Photoluminescence Spectra and Quantum Yield (PL & QY)**

PL is the light emission from a sample after it absorbs photons (electromagnetic radiation). This process is initiated by the photoexcitation (excitation by photons) and is one of the many forms of luminescence. After the excitation process, several relaxation processes occurs where other photons are re-radiated. Time gap between the absorption and emission process may vary depending on the type of material. PL contains useful information that can assist in sample analysis. The color and intensity of PL give information about nanocrystal size, surface states, and several other information regarding the nanocrystal.

PL can be useful to study crystal defects, like atomic vacancies and substitutions and the nanocrystal size can also be calculated based on the emission peak wavelength. PL Quantum Yield (QY) is the measurement of sample efficiency in terms of light emission. It is calculated

by dividing the number of photons emitted by the sample with the number of photons absorbed by it. PL measurements were performed using an Ocean Optics, Inc. USB spectrometer and optical fiber. The PL was excited using three different LED (peak at 265 nm, 325 nm and 395 nm respectively). An Ocean Optics integrating sphere was used for QY measurements.

### **2.3.6 Fourier Transform Infrared Spectroscopy (FTIR)**

FTIR is a kind of surface measurement technique. Molecular vibrational frequencies for many compounds lie in the IR region of the electromagnetic spectrum and therefore can be measured by this technique. In FTIR, a polychromatic infrared light is passed through a sample and these transmitted light intensities are measured corresponding to each frequency. Due to IR absorption by surface species, a transition occurs from the ground vibrational state to the excited vibrational state inside the molecules. The IR light is collected after interacting with the sample, and the absorbed frequencies indicate which surface bonds are present in the sample.

A Bruker Alpha Fourier Transform Infrared (FTIR) spectrometer has been used for our samples in diffuse reflectance mode.

### **2.3.7 Raman Spectroscopy**

Raman is a spectroscopic technique that can be used to measure mainly vibrational and rotational modes in a sample, but it is also useful for other low-frequency modes. In this type of spectroscopy, the sample is irradiated with photons of known energy (laser light). This laser light then interacts with the sample and the presence of molecular vibrations or phonons in the sample makes it more interesting. Due to these interactions, the energy of the photons from laser light can increase or decrease and based on this energy change, we can get useful information regarding different modes in the sample. This information can be used to identify the species in

the bulk of a sample and is useful for classifying the crystal structure and identity of nanoparticle samples.

We have used a HORIBA Jobin-Yvon LabRAM ARAMIS Raman confocal microscope/spectrometer from CMSC, MSU, to perform spectroscopic analysis and a 532 nm laser was used to excite the sample.

### **2.3.8 Electron Paramagnetic Resonance (EPR)**

EPR is a technique used for the detection of species with unpaired electrons. It is also known as Electron Spin Resonance (ESR). Interestingly, a lot of materials have paramagnetic defects and therefore can be detected by EPR. We have used this technique to figure out whether our synthesized nanoparticles have any defects.

EPR is a magnetic resonance technique and we are trying to detect the unpaired electrons with the help of magnetic field<sup>82</sup>. Due to the applied magnetic field, the orientation of these paramagnetic electrons would be either parallel or antiparallel with the direction of magnetic field. Due to this, two different energy levels will be formed: lower energy level and upper energy level. To excite the electrons from the lower energy level to the upper energy level, a specific microwave frequency is required. This microwave frequency should be matched by the energy gap (energy difference between the lower and upper level) of the external magnetic field in order for transition to occur. This is known as EPR resonance (or absorption).

A Bruker ELEXSYS-II E580 EPR model from Department of Chemistry, MSU was used to perform the spectroscopic measurement. A 5 mm medium wall suprasil EPR sample tube was used to prepare the sample. Prof. John McCracken helped us in performing EPR analysis for our samples.

## CHAPTER 3

### Stretchable Luminescent films of Silicon Nanocrystals

Note: reproduced in part with author permission from R. Mandal and R. Anthony, 2016 (Submitted).

#### 3.1 Introduction

SiNCs and Si-based nanostructures have a special place in the broader nanotechnology field. Silicon plays a major role in the semiconductor industry and offers some great advantages. New properties and functionalities arise for nanoscale Si, which exhibits efficient and tunable luminescence<sup>31,50,58,83</sup>. Additionally, emerging applications involving stretchable and flexible electronics for optoelectronic applications such as *in-situ* health monitoring, display technology, and inexpensive, versatile LEDs and solar cells are not feasible using bulk semiconductors. Therefore, nano-Si could be a great alternative for these applications.

In any NC-based application, incorporating the NCs into the device architectures presents a novel challenge, particularly when deformable substrates for flexible/stretchable devices are required. Many deposition schemes involve solvent processing (spin- or drop-casting) or high temperatures, precluding deposition directly onto elastomeric substrates like PDMS. Gas-phase inertial impaction, however, can sidestep many of these issues by allowing NCs to directly impinge upon substrates from the vapor phase, eliminating solvents and high temperatures<sup>60,71,84</sup>. This inertial impaction opens the door to creating next-generation stretchable and flexible devices using the exciting tunable properties of NCs.

Here, we present results on inertial impaction of plasma-produced Si NCs onto elastomer substrates. The resulting SiNC films formed surface instabilities / wrinkles when the substrates

were relaxed. Our initial measurements also indicated that the PL peak wavelength depended on the stretch state of the elastomer during deposition. Further investigations led us to the hypothesis that the PL shift is in fact due to enhanced oxidation of the SiNCs on PDMS substrates. These results point towards an enhanced understanding of SiNC film formation on stretchable substrates, and can be expanded to other vapor-phase-deposited NCs. In turn, these results will be used to design and engineer novel device applications such as stretchable/bendable LEDs, displays, and others.

### **3.2 Experimental Details**

We have used a nonthermal low pressure plasma reactor for the synthesis of Si NCs, as discussed previously<sup>50</sup>. The flow-through reactor consists of a pyrex tube with an Outer Diameter (O.D.) of 1.27cm in the top portion and 2.54cm in the bottom portion. The tube is 30.5cm long and the expansion area is 17.8cm from the top. Argon (Ar) and silane (SiH<sub>4</sub>, 1% in Ar) were flown through the Pyrex tube, and 13.56 MHz radiofrequency (rf) power was supplied via dual ring electrodes encircling the upper portion of the tube. The gas flowrates for Ar and SiH<sub>4</sub>/Ar were 5-30 sccm and 50-80 sccm respectively. The pressure in the reactor was kept at 1.85-2.6 Torr using a slit-shaped nozzle orifice, and was 160-300 mTorr downstream of the orifice. The described conditions led to synthesis of crystalline Si NCs of diameter 4-5nm, as confirmed using TEM, x-ray diffraction (XRD), and Raman spectroscopy. The slit-shaped orifice at the reactor base accelerated the Si NCs and they inertially impacted onto the substrates underneath<sup>60,71,84</sup>. For most of the experiments, Si NCs were deposited onto polydimethylsiloxane (PDMS) films and bulk silicon wafers. The deposition was performed by rastering the substrates beneath the orifice at a standoff distance of ~3mm. Following synthesis, the samples were stored in air.

PDMS was prepared in the lab using Sylgard 184 (Dow Corning Corp.). The prepolymer base (PDMS monomer) and the cross linking agent were vigorously mixed in a 10:1 weight ratio, then degassed in a vacuum desiccator for 20-25 minutes until all the air bubbles were removed from the mixture. Pre-measured amounts of the mixture were cast into plastic petri dishes, leading to film thicknesses of  $\sim 0.5$  mm. The PDMS was then heat-cured using a hot plate at  $60^{\circ}\text{C}$  for 2-3 hrs. The PDMS was cooled at room temperature and cut into small substrates of dimensions  $28\text{mm} \times 12\text{mm}$ . SEM image of this PDMS film shows (Figure 3.1) random micro ridges at the film surface. For PDMS films, which are not conductive, we had to coat it with tungsten (W) for better SEM imaging.

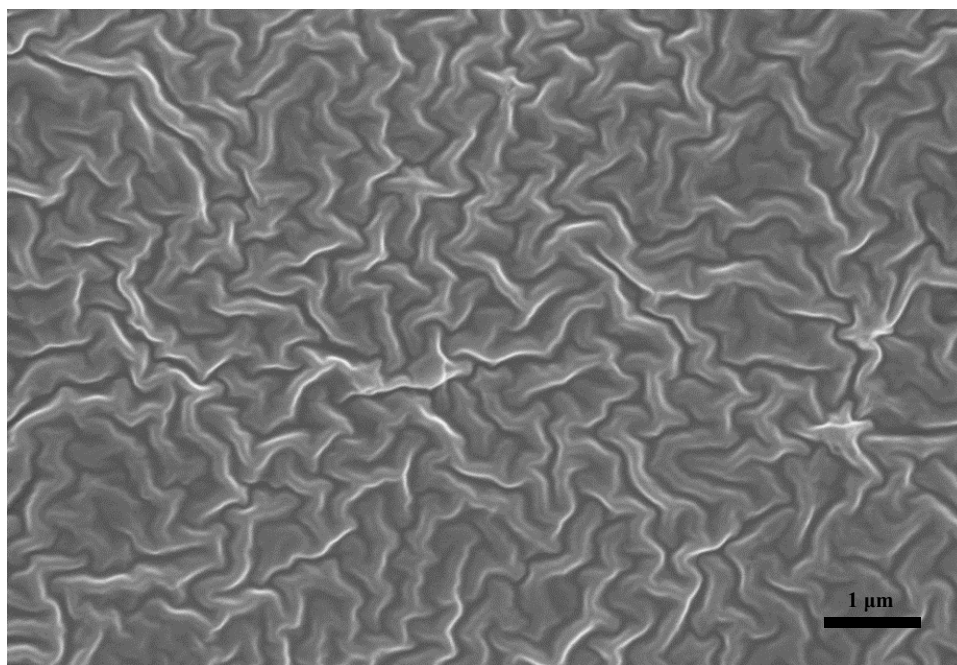


Figure 3.1: SEM image of a typical PDMS surface.

With the aim of making stretchable film of Si NCs, a stretching stage has been designed and manufactured based on our reactor geometry (see Figure 3.2). This stretching stage can easily be coupled with the push rod. One end of this stage is fixed and the other end can move on a

threaded screw and is controlled by a knob attached with the screw. Based on the dimension of our PDMS films, this stage can stretch the film to more than 100% of its actual length.

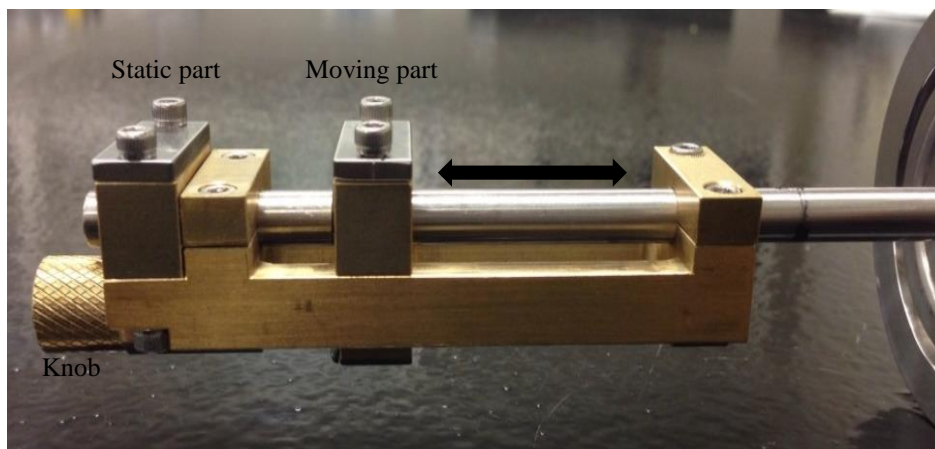


Figure 3.2: Stretching stage coupled with the push rod.

PL measurements were performed using an Ocean Optics, Inc. USB spectrometer and optical fiber. The PL was excited using a UV/blue LED (peak at 395nm). The measurements were performed in air. FTIR study has been performed using a Bruker Alpha-FTIR instrument with a diffuse-reflectance (DRIFTS) module to understand the surface properties of the Si NCs. Scanning Electron Microscopy (SEM) has been performed using a Carl Zeiss Auriga Dual Column FIB SEM at The Composite Materials and Structures Center (CMSC) and for TEM, we have used JEOL 2200FS ultra-high resolution transmission electron microscope at the MSU Center For Advanced Microscopy. A Kaiser Optical Systems Holoprobe Raman Spectrograph setup from W. M. Keck Microfabrication Facility, MSU has been used to perform Raman analysis of Si NCs. XRD of our Si NCs was performed in the Center for Crystallographic Research, MSU using a Bruker Davinci Diffractometer.

### 3.3 Results and Discussions

This research is the first investigation to our knowledge of inertial impaction of nanomaterials onto elastomeric substrates, and our first experiment was to deposit a thin layer of Si NCs onto a relaxed PDMS substrate as well as a silicon wafer substrate to compare the appearance and PL of the resulting films. In addition, the house-built stretching stage allowed us to prestretch the PDMS before deposition, and then allow it to relax. Henceforth, we refer to samples produced on prestretched PDMS according to their “stretching ratio”, meaning the ratio of the length of the PDMS during the stretching/deposition to its length when relaxed. We produced SiNCs on silicon wafer, relaxed PDMS, and PDMS at stretching ratios of 10%, 20%, and 40%.

Before going into the experiment of stretchable film, we have performed the nanoparticle characterization using a variety of instruments. To verify the crystallinity of Si nanoparticles (Si NPs), XRD measurement has been performed. XRD patterns clearly shows peaks from the [111], [220] and [311] crystallographic planes at  $28.46^\circ$ ,  $47.51^\circ$  and  $55.91^\circ$  respectively as shown in Fig. 3.3.

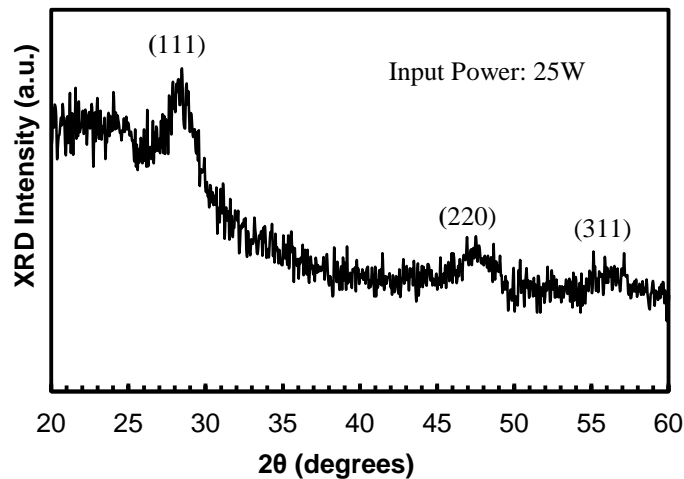


Figure 3.3: X-ray diffraction patterns from Si nanoparticles.

Raman vibrational spectroscopy was also performed to validate the XRD results and the emergence of a peak at  $514.81\text{ cm}^{-1}$  (see Fig. 3.4), corresponding to nanocrystalline Si, strengthens our conviction that we have crystalline nanoparticles. Our results from XRD and Raman spectroscopy were found to be in good agreement with the published literature<sup>85-87</sup>. TEM analysis has also been performed to characterize the nanoparticle size and its microstructure (see Fig. 3.5).

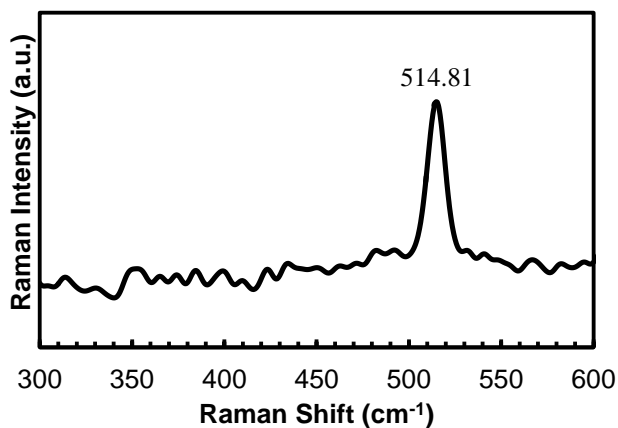


Figure 3.4: Raman vibrational spectroscopy from Si nanoparticles.

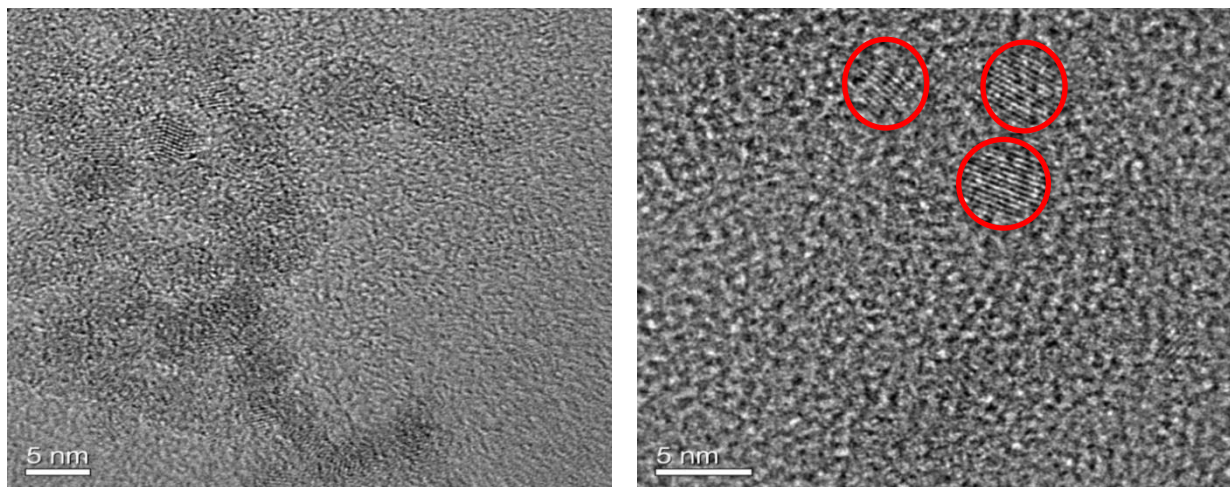


Figure 3.5: High resolution TEM images showing Si NCs.

TEM analysis validated the crystallinity of Si nanoparticles. Microscopy was performed by Dr. Fan at the Center for Advanced Microscopy, using a JEOL 2200 FS ultra-high resolution

microscope. We used graphene-coated copper grids and deposited Si NCs using drop-casting from ethanol. The size of these NCs is  $\sim 5\text{nm}$  which is important for light emission purposes. In these images, the lattice fringes from crystalline silicon are clearly visible-indicating the fact that the crystallinity of these nanoparticles is high.

In order to get an idea of the surface bonding of the nanoparticles, we have studied the FTIR spectra (see Fig. 3.6). Sample for this study is prepared by using 50 sccm of  $\text{SiH}_4$ , 5 sccm of Ar and 25W of electrical input power.

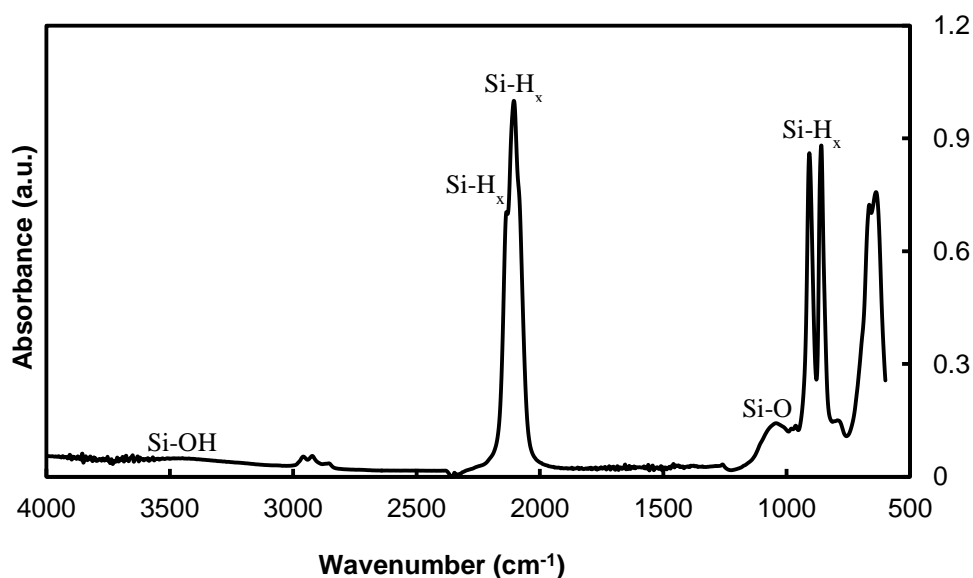


Figure 3.6: FTIR spectra from Si NCs.

FTIR analysis was performed right after the deposition of nanoparticles. A Bruker Alpha FTIR spectrometer was used for this purpose in diffuse reflectance mode. The absorption bands can be assorted into three groups. The bands located at wavenumber  $k= 3420\text{ cm}^{-1}$  can be attributed to Si-OH vibrations in surface bound hydroxyl groups. The absorption bands at wave numbers,  $k = 2105\text{ cm}^{-1}$ ,  $k = 2139\text{ cm}^{-1}$  represents Si-H stretching vibration and  $k= 908\text{ cm}^{-1}$ ,  $k = 860\text{ cm}^{-1}$  represents Si-H bending/wagging vibrations at the Si surface. This showed that the particles are primarily covered with hydrogen and confirmed the presence of chemically bound

H atoms on the surface of the SiNCs<sup>88</sup>. The peak at wavenumber  $k = 1052 \text{ cm}^{-1}$  is very small and it represents a partial surface oxidation of the silicon nanoparticles. The fact behind this partial oxidation is the time taken to transfer the sample from the reactor to the FTIR, when it was exposed to air.

The Si NCs were produced without hydrogen injection into the plasma, causing them to have a nontrivial surface defect density and thus PL QY of only several percent immediately after deposition<sup>61</sup>. Thus, to measure their PL, we have waited 1-2 days after their deposition on substrates to allow ambient-air oxidation to begin to cap the defects and increase the samples' PL intensities. The results of these PL measurements were surprising: Despite using exactly the same recipe for synthesis, the PL from SiNCs on PDMS was significantly blueshifted in comparison to the PL from SiNCs on silicon wafer (up to 80nm) (Fig. 3.7 (a)). The PL peak should, in principle, depend on the Si NCs themselves and not their substrate, and so we found this result to be puzzling. Even more intriguing, we found that the PL peak for the Si NCs on prestretched PDMS actually shifted back towards the peak position for Si NCs on silicon wafer (see Fig. 3.7(b)).

As the Si NC recipe was the same, we expected the PL peak to remain constant regardless of substrate – and so we began to consider possibilities to cause the PL to shift. Our first hypothesis regarded possible changes to the film microstructure. The Bohr exciton radius for silicon is near  $5 \text{ nm}^{89,90}$ , which is very close to the size of these Si NCs. We realized that the PL peak of the Si NCs would possibly be dictated by the Si NCs' proximity to one another, as the effective grain size (and thus spatial confinement of the exciton) will depend on the packing of the NCs in the films. More densely packed NCs would thus have a redshifted PL peak compared to loosely packed NCs.

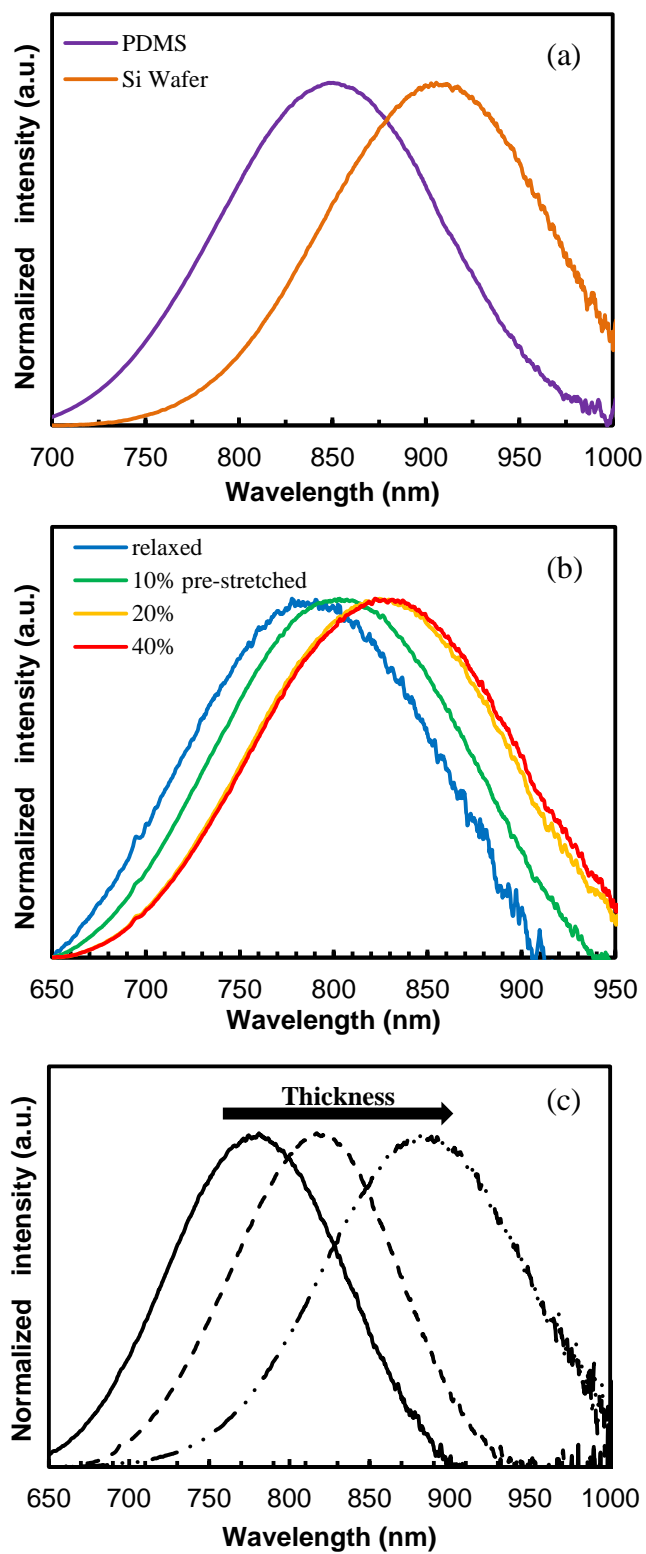


Figure 3.7: Photoluminescence spectra (a) different substrate (b) different stretching ratio of PDMS (c) different thickness of PDMS films

To be consistent with this hypothesis, the NCs on PDMS would have to be more loosely packed than the NCs on silicon wafer. However, both top-down and cross-sectional SEM images (Fig. 3.8) confirmed instead that the Si NC layers on PDMS were more densely packed compared to layers on silicon wafer.

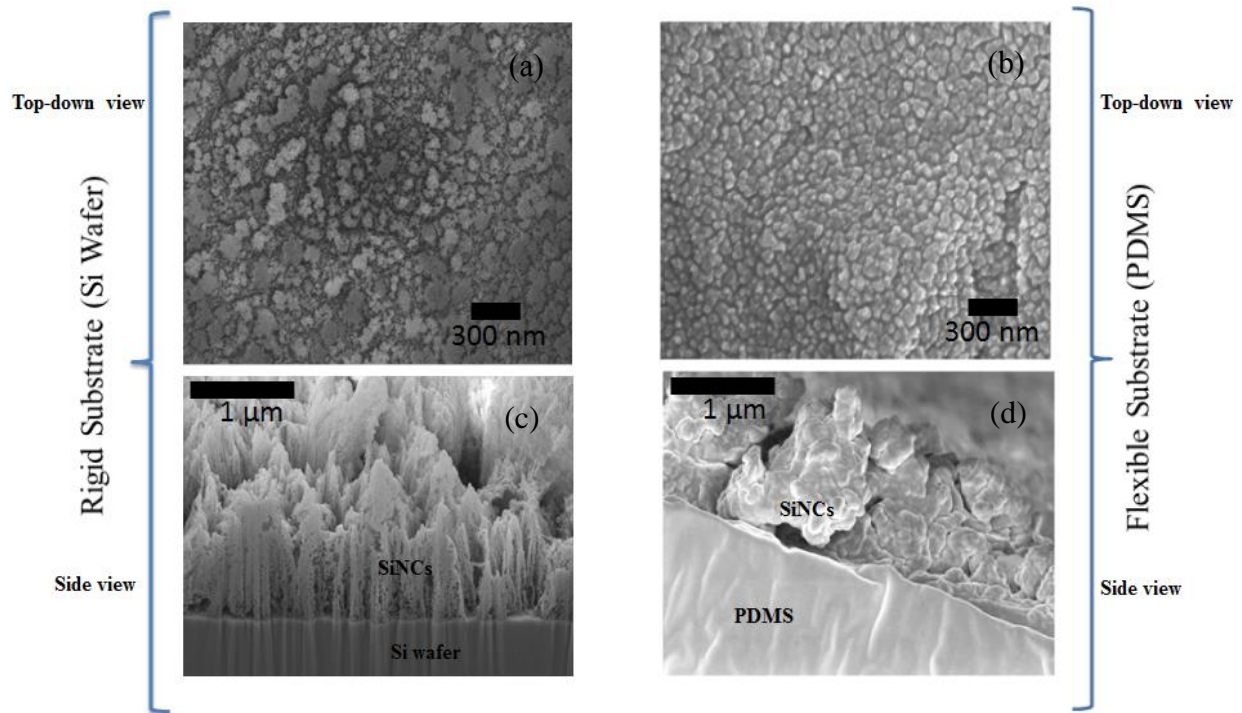


Figure 3.8: SEM images of Si NC films: (a) & (c) on Si wafer, (b) & (d) on PDMS.

To perform SEM, SiNC films on both Si Wafer and PDMS were coated with 3nm of Tungsten (W) to have better contrast. For 10 min deposition time, thickness of the film was  $\sim 1 \mu\text{m}$ . The SiNC film deposited on PDMS has significantly different morphology as compared to the film deposited on Si wafer. Films on PDMS are denser, and the nanoparticles form more articulated grains. In contrast, the films on Si wafers are fluffier. The reason behind this morphological difference might be attributed to the difference in elastic properties of the PDMS as compared to Si wafer. Also, the top-down SEM analysis has been performed for PDMS films with different

stretching ratio and the results are shown in Figure 3.9. It is clearly visible that, for non-stretched film, there is no large-scale cracking (there was no strain) in the film and the nanoparticles formed articulated grains.

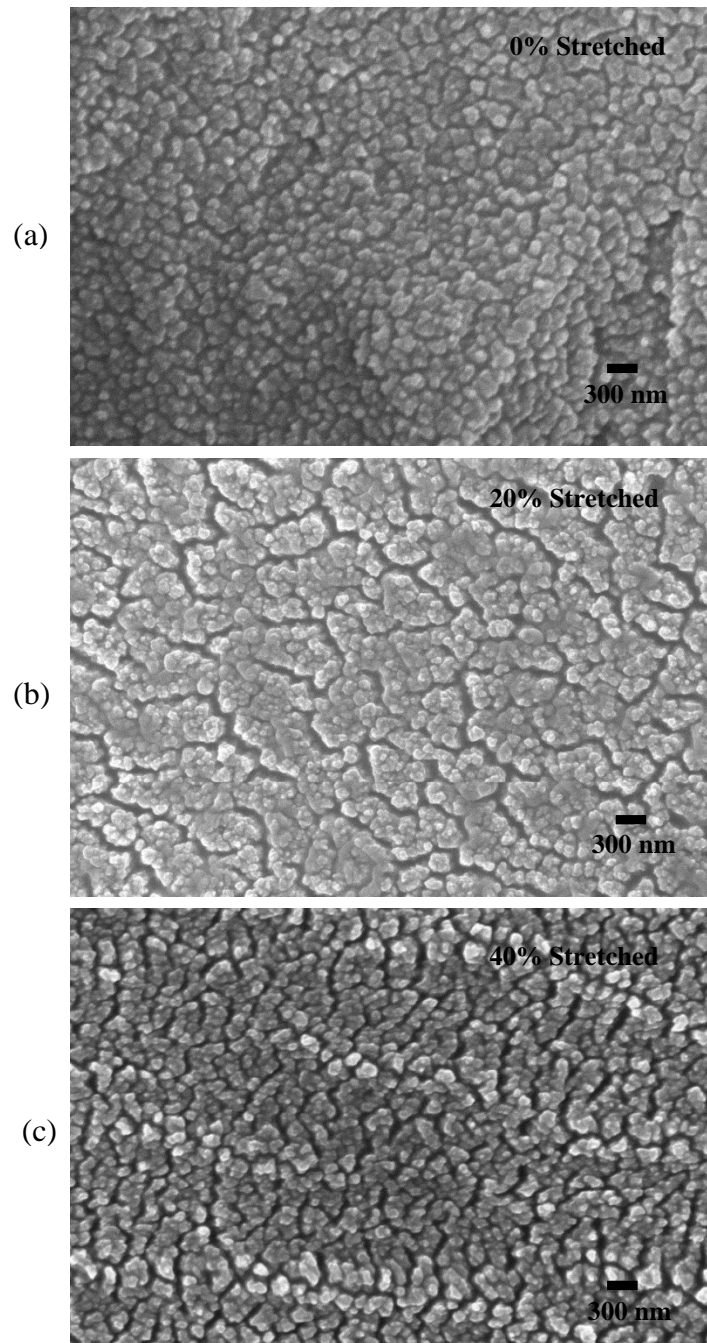


Figure 3.9: SEM images (Top-down view) of Si NC films on PDMS with different stretching ratio.

But, as we increase the stretching ratio, cracks started to develop and become bigger with increasing stretching ratio. Another important point to be noted is that “wavy” structures started to form with stretching.

As a next step, we deposited films of varying thickness on PDMS. Our initial measurements had been made on fairly thick layers of  $\sim 1\mu\text{m}$ , which required 100 rastering cycles (deposition time 10 mins). We deposited Si NCs on relaxed PDMS with 10 cycles, 50 cycles, and 100 cycles (corresponding to  $\sim 100\text{nm}$ ,  $500\text{nm}$ , and  $1\mu\text{m}$ ). We then measured the PL from these layers, revealing that the thin films have PL that is blueshifted even more dramatically than the thick films (see Fig. 3.7(c)). The thickness dependence of the peak PL wavelength seeded the idea that oxidation of the films may be responsible for the changes in peak PL wavelength. Oxidation of Si NCs causes a  $\text{SiO}_x$  layer to grow at the NC surface, corresponding to a core size shrinkage and blueshifting PL<sup>91,92</sup>. An increased rate of oxidation of Si NCs on PDMS compared to on silicon wafer would explain the difference in peak PL wavelength, and would also explain the thickness dependence (thinner films oxidize more rapidly).

We then remade our samples on relaxed and prestretched PDMS as well as on Si wafer, and stored them in a nitrogen-purged glove bag, keeping a set of films in air as well. We measured their PL immediately after synthesis and for several days after synthesis to observe whether the oxygen-free environment affected the PL peaks. The results are shown in Figure 3.10. For samples stored in the glove bag, the PL peaks overlap on the first day and on subsequent days. For samples stored in air, the peaks began to shift from one another (blueshifting for the samples on PDMS) within a day of synthesis. This confirmed the hypothesis that oxidation is enhanced on PDMS. The air-permeability of PDMS has been demonstrated by

previous groups<sup>93,94</sup>, and thus the Si NC films on PDMS were oxidizing not only from the top but also through the bottom of the films. The PL measurements are ensemble measurements, collecting light from the entirety of the film thickness – thus, additional oxidation at the back of the films would lead to blueshifting compared to the films on silicon wafer, which were only oxidizing from the top.

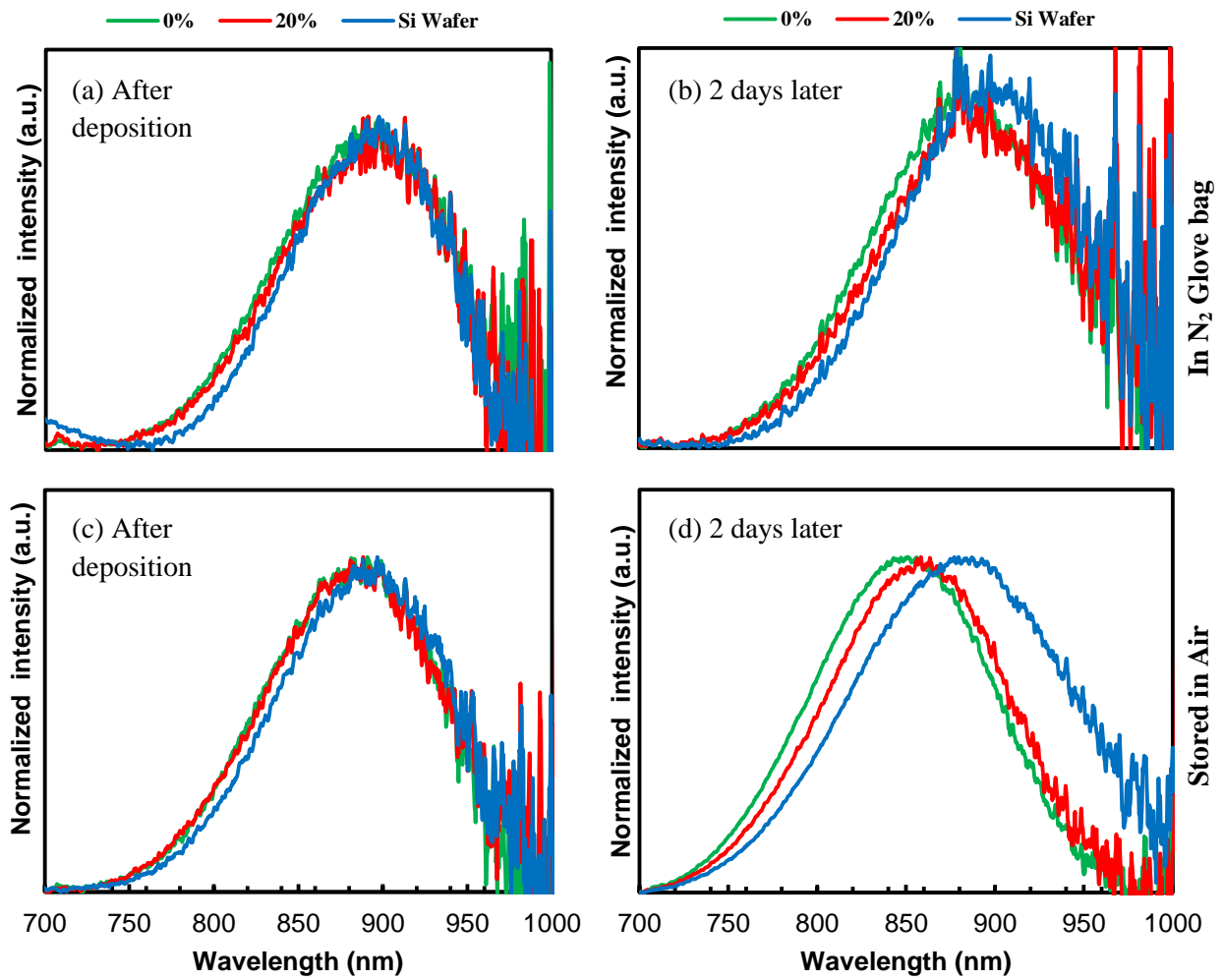


Figure 3.10: Photoluminescence spectra from oxidation dependence experiment.

These PL data have been validated with the FTIR data. FTIR analysis has been performed for samples kept in nitrogen-purged glove-bag as well as in open air conditions. For both cases,

copper has been used as a substrate material and data has been recorded right after deposition as well as after 2 days. The results are shown in Figure 3.11. There is minimal surface oxidation present (Si-O-Si vibration  $\sim 1050\text{ cm}^{-1}$ ) for both the samples right after the deposition and this is likely due to performing the measurements in air.

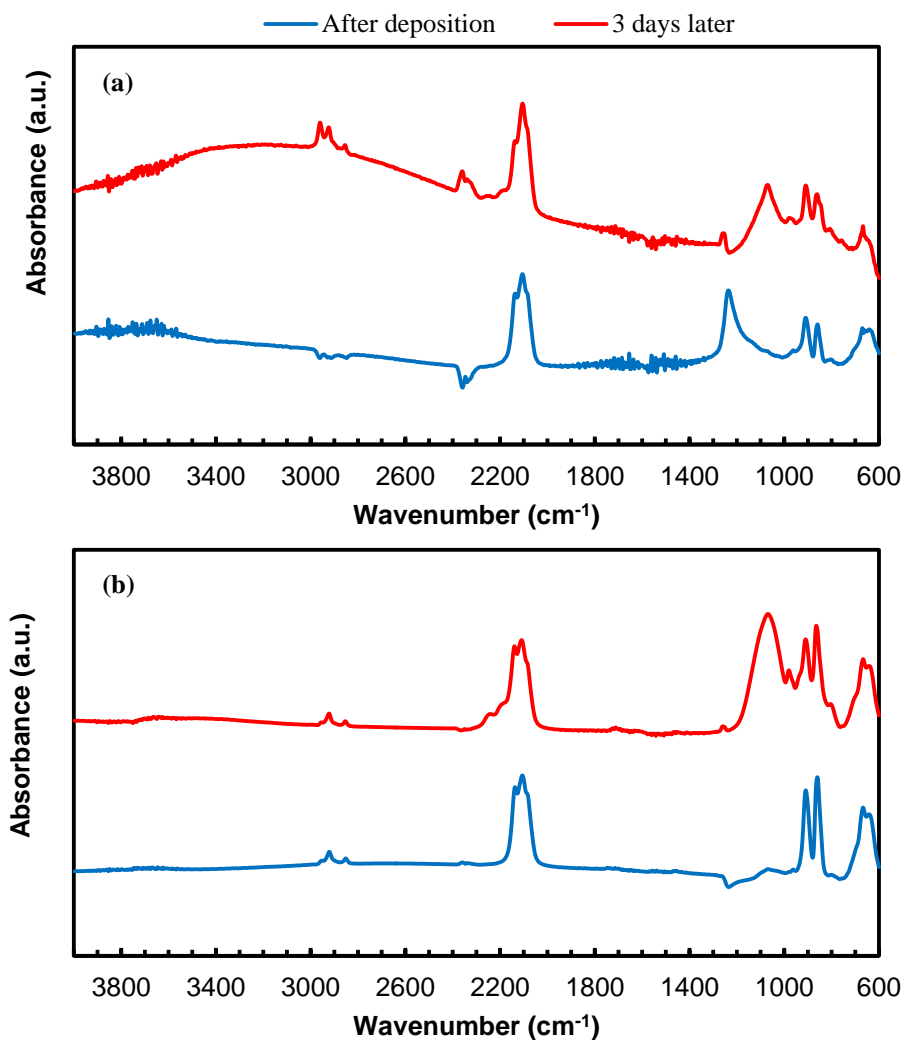


Figure 3.11: Comparison of FTIR spectra analysis (a) sample from glove bag (b) sample from open air. Oxidation peak (Si-O-Si) is located at  $\sim 1050\text{ cm}^{-1}$ .

After the measurement, all the samples were stored in their respective environment. The next measurement was performed after two days. For the samples stored in open air, the NC surface has been oxidized heavily (a dominant peak is visible for Si-O-Si vibration at  $\sim 1050\text{ cm}^{-1}$ ).

Whereas, for samples stored inside glove bag, no such dominant peak is visible for Si-O-Si vibration.

The dependence on stretching ratio can be explained by examining the surface of a Si NC film on pre-stretched PDMS before and after relaxing the substrate. To do this, we deposited Si NCs on a PDMS substrate pre-stretched to 40% of its initial length, and left the substrate and Si NC film in place on the stretching stage while imaging in the scanning electron microscope (SEM). The SEM image shows a fairly flat layer of NCs. Then, we removed the stage and relaxed the film of Si NCs, then re-imaged the film. After relaxing the substrate, the Si NC film developed wrinkles across its surface (see Fig. 3.12(a)).

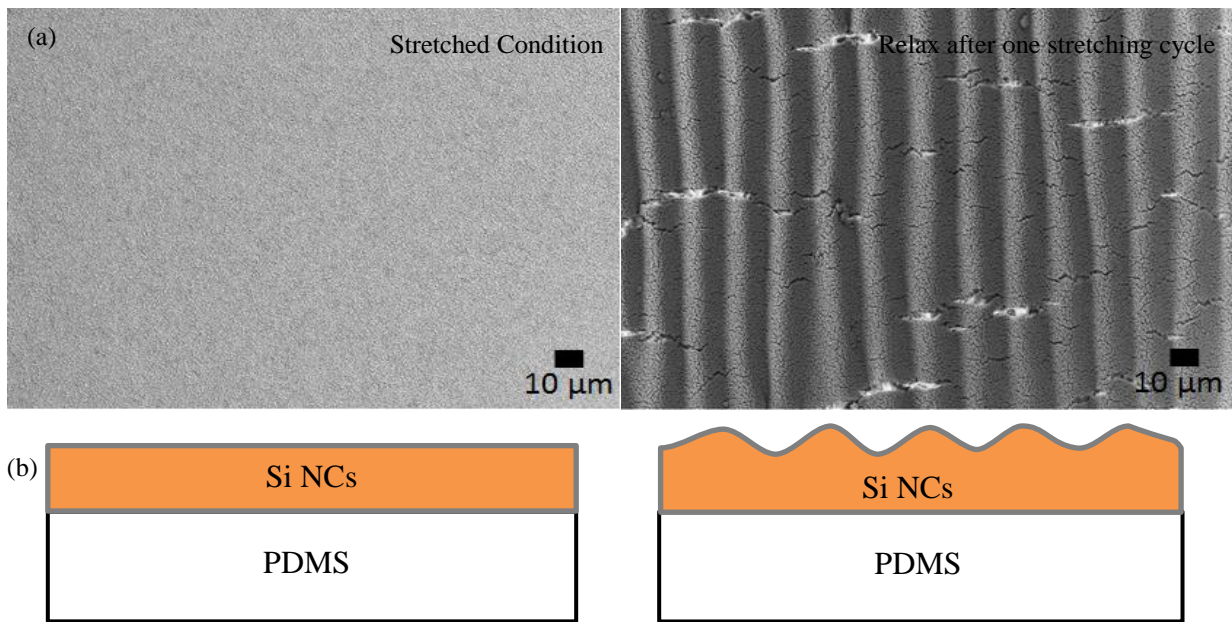


Figure 3.12: (a) SEM images of a Si NC film on PDMS in different conditions, (b) a cartoon showing wrinkling formation in PDMS films.

This wrinkling causes the Si NC film to be thicker in some places compared to the same thickness Si NC film on relaxed PDMS or on silicon wafer. The increased thickness would result in reduced fraction of Si NCs that are oxidized, compared to the entirety of the film. This

explains why increasing stretching ratio causes reduced blueshifting of the PL peak. Figure 3.13 shows a cartoon of this process.

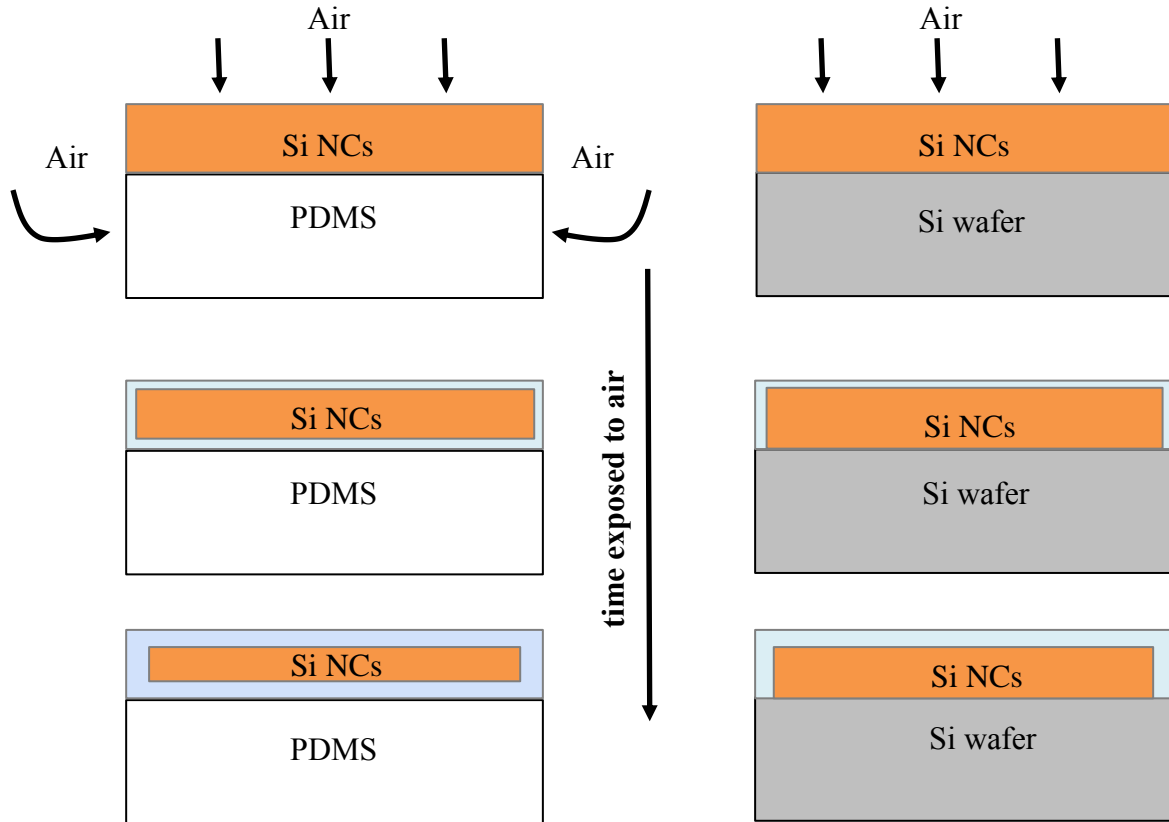


Figure 3.13: Oxidation dependence experiment with cartoon.

It is clearly seen that the PL peak shifts to lower energies (red-shifting) with increasing stretching ratio. Between unstretched PDMS and PDMS stretched 40% beyond its original length, the difference in PL peak position is 60 nm. PL has also been recorded for the same set of samples when they were in stretched condition and the same trend has been found. Emission intensity also increases with increasing stretching ratio. For the same sample, intensity is higher in stretched condition compared to relaxed condition. The reason behind this kind of behavior of the Si NC film on PDMS could be due to buckling effect, but the major reason is the enhanced

oxidation as discussed before. These findings have been thoroughly investigated with different combination of flow rates of  $\text{SiH}_4$  and Ar, and the results found were consistent. A summary of this project is shown in Figure 3.14.

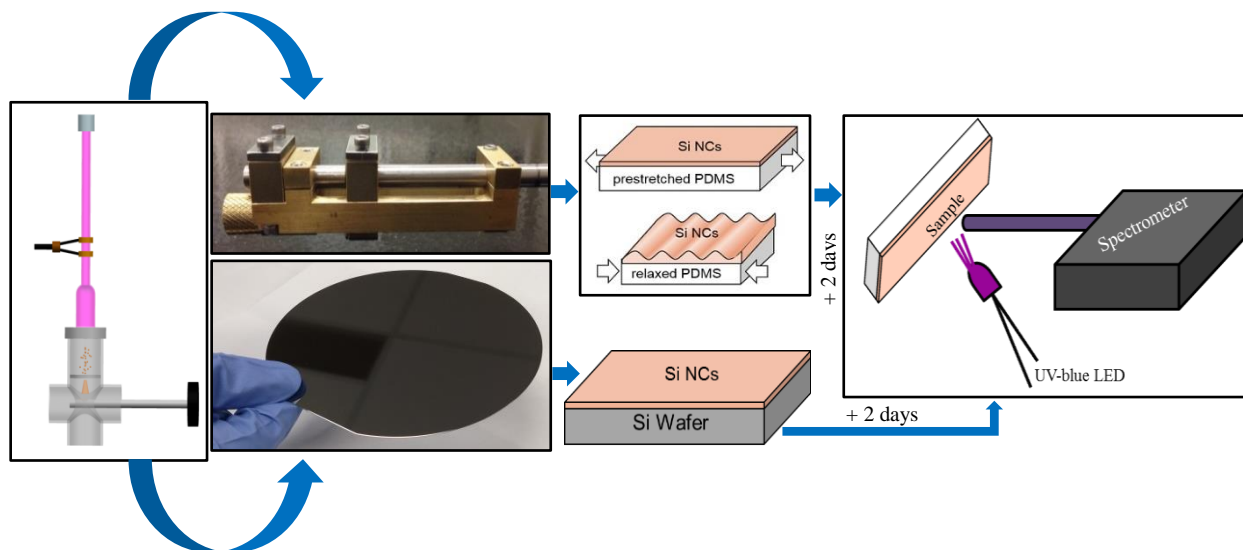


Figure 3.14: Flowchart showing different steps of this experiment.

### 3.4 Conclusions

In conclusion, we have demonstrated the first all-gas-phase deposition of luminescent NCs onto elastomeric substrates. The films show wrinkling in response to pre-stretch of the PDMS substrates, as well as structural changes compared to Si NCs deposited on Si wafers. We hypothesize that these changes are a result of the elastic response of the substrate, and plan future studies to describe and model these observations. The Si NCs on relaxed PDMS exhibited blueshifted luminescence compared to Si NCs on Si wafer, with decreased blueshifting observed for the wrinkled Si NC films which had been deposited on prestretched PDMS. Our experiments confirm that the blueshifting effect is due to enhanced oxidation on PDMS, caused by the air-permeability of PDMS and thus oxidation of the Si NC films from all sides as opposed to the top-down-only oxidation that occurs for Si NCs on Si wafers. These results will aid ongoing and

future development of stretchable and flexible luminescent NC layers for next-generation displays, LEDs, and other devices.

## CHAPTER 4

### Gas-Phase Synthesis of Gallium Nitride (GaN) Nanocrystals using Non-Thermal Plasma Reactor

#### 2.4 Introduction

Bulk GaN is a standard light-emitting material, very efficient for Light Emitting Diodes (LEDs) and has been in use for many years. This material is very attractive due to its high-brightness emission and thermal stability. GaN is a direct band gap semiconductor and is widely used in the ultraviolet/blue light emission technologies due to its band gap energy of 3.4 eV. The major advantage of GaN over other popular semiconductors like cadmium selenide (CdSe) is its relative non-toxicity. Although, GaN is mostly used in blue/ultraviolet high-brightness solid-state lighting devices<sup>95-97</sup>, nanoscale form of GaN offers tunable emissions<sup>98</sup> and doping of GaN and alloying with other semiconductor materials (for example, Indium Gallium Nitride, InGaN) will enable these devices to be applicable in the visible spectrum as well<sup>99-102</sup>. Besides, emerging applications involving stretchable and flexible electronics for optoelectronic applications are not feasible using bulk semiconductors.

NCs are normally inexpensive to produce and easy to deposit via a number of solvent-based techniques such as spin casting and drop casting; therefore, the idea of using a GaN NC based LED for white light emission is an attractive solution to improve the ubiquity and versatility of solid-state lighting (SSL). But, working with these colloidal NCs requires solution-phase processes and there are a few problems associated with it. A large fraction of NCs could

go waste as this process uses a number of steps with different solvents. Besides, these solvents could be environmentally toxic and can create limitations in the device structure due to incompatibility with other solvents or materials. Therefore, there is a need to develop a technique for incorporating NCs into GaN-based LEDs without involving these solution processes.

The scarcity of defect-free GaN crystal lattice poses the major roadblock in achieving high-efficiency devices. This mostly happens due to the lattice mismatching between the substrate material and GaN as there are very few substrate material available that has same lattice structure and thermal compatibility with GaN and in most cases, these substrate materials are very expensive. It is also well known fact that the substrate material and its orientation mostly affect the crystal structure of epitaxially grown GaN. From the viewpoints of lattice mismatch and crystal symmetry, sapphire is the most suitable substrate for GaN growth. The problem is that epitaxial growth of high-quality GaN requires costly substrates (*e.g.* sapphire), high temperatures, and long processing times. These processing challenges prohibit some of the most innovative applications of electronic devices, including stretchable/flexible displays and wearable sensors/electronics. Synthesizing freestanding NCs of GaN, on the other hand, could enable these novel device morphologies, as the NCs could be incorporated into devices without the requirements imposed by epitaxial GaN growth.

There are several recent studies which show effort into synthesis of GaN NCs<sup>69,95–97,99,103–107</sup>. Prior works on GaN nanocrystal synthesis have involved a range of methods, such as: thermal reactions of ammonia (NH<sub>3</sub>) with gallium compounds<sup>96</sup>, reactive laser ablation<sup>108</sup>, metal-organic chemical vapor deposition<sup>109</sup>, solution phase methods using gallium organometallic compounds<sup>110</sup>, mechanical grinding of powders<sup>102,111</sup>, microwave resonant cavity<sup>112</sup>, arc plasma<sup>103</sup>, molecular beam epitaxy<sup>99</sup>, spray pyrolysis<sup>106</sup> and some other techniques as well. Many

of these above mentioned processes are time and energy consuming and either require pre-chosen substrate for GaN NCs deposition or require liquid-phase processing techniques. GaN NC synthesis using a flow-through plasma could be an exciting option as it has all the ingredients for stoichiometric synthesis and it is a low-temperature process unlike other existing processes which requires high temperature<sup>112</sup>. This flow-through plasma process has already been used extensively not only for the synthesis of group IV NCs like silicon and germanium, but also for some compound materials like indium phosphide (InP), Si-Ge alloys and Zinc Oxide (ZnO)<sup>50,67,68,70,113</sup>. Motivated by these advantages, we have used this non-thermal plasma processing technique for the synthesis of GaN NCs, which is a fully gas-phase-only deposition scheme.

## 2.5 Experimental Details

We used a nonthermal plasma reactor for the synthesis of GaN NCs directly from gaseous precursors and deposited onto glass substrates without any additional steps. The plasma reactor has some advantages over other available methods, namely size monodispersity, easy tuning of NC properties such as size and surface, and the ability to deposit the NCs directly from the gas phase without removal from the reactor. The plasma route is also inexpensive and GaN NCs can be processed rapidly. Some studies have already been performed with microwave plasmas<sup>69,112</sup>, but microwave plasmas require higher power and frequencies. Therefore, radiofrequency (RF) plasmas are an attractive alternative. An RF nonthermal plasma reactor is comprised of a borosilicate glass tube with three ring electrodes encircling the tube externally as shown in Figure 4.1.

Vapor-phase precursors and carrier gases were flown through the glass tube at relatively low pressure (typically 5-15 Torr). Power was supplied from a RF power source through a

matching network to the electrodes. Our Ga source was TMGa, our nitrogen source was  $\text{NH}_3$ , and Ar was the background gas. TMGa was flown to the reactor without a carrier gas but *via* a pressure based mass flow controller (MFC) which operates based on the vapor pressure of TMGa at room temperature. The total TMGa vapor flowrate was varied from 1-2 sccm,  $\text{NH}_3$  at a flowrate from 50-90 sccm and the Ar flowrate was varied from 50-100 sccm. The total gas flowrate was varied from 100-200 sccm and the pressure in the reactor was kept between 5-15 Torr using a slit-shaped orifice. Pressure can be easily tuned by changing the orifice width. Supplied power was varied from 60-150W.

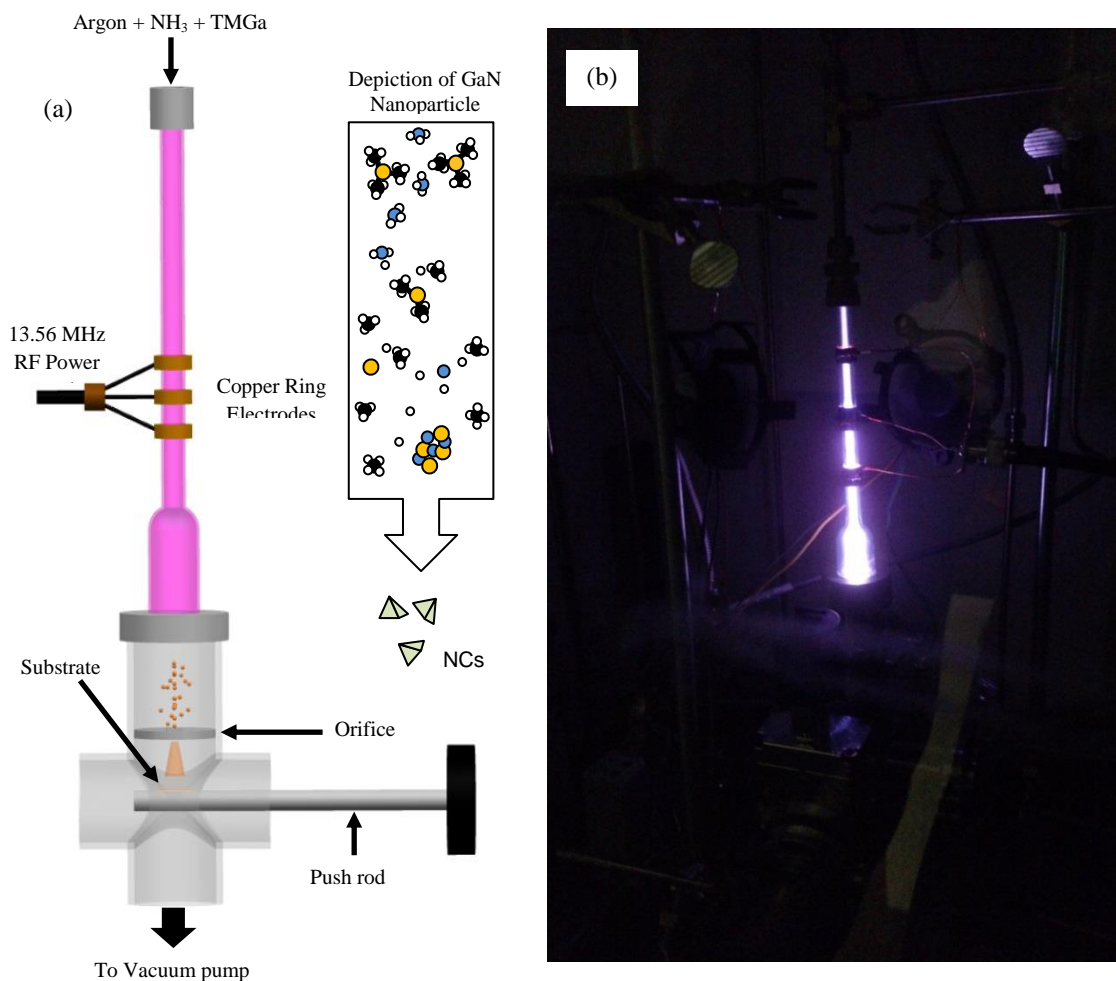


Figure 4.1: The Plasma Reactor (a) Schematic (b) Photo of Experimental setup.

For most part of the experiments, GaN nanoparticles were deposited via inertial impaction technique onto glass substrate. A slit-shaped orifice at the reactor base accelerated the nanoparticles and they inertially impacted onto the substrates underneath<sup>60,71,84</sup>. The deposition was performed by rastering the substrates beneath the orifice at a standoff distance of  $\sim 3$ mm. Following synthesis, the samples were stored in air.

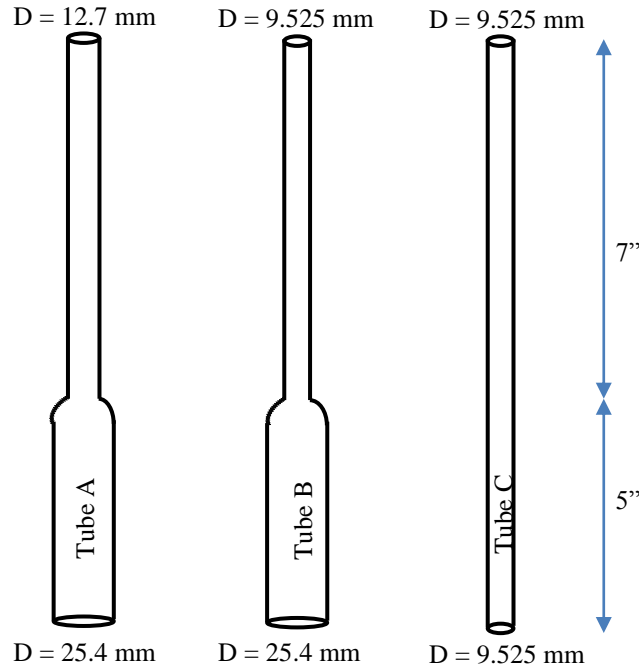


Figure 4.2: Glass tubes with different dimensions used for the plasma reactor.

In principle, the plasma imparts the particles with a negative charge and thereby discouraging the agglomeration of nanoparticles. Only the free electrons are heated by the supplied power. The electron-ion recombination happens at the nanoparticle surface that results in the heating of the particles and eventually aiding particle crystallization<sup>50</sup>.

We started this research with two objectives: (1) to synthesize GaN NCs using a fully gas phase process, and (2) size tunability of GaN NCs for luminescence applications. For size tunability, we have used three different glass tube dimensions (see Fig. 4.2) with different flow

combinations to get different residence time and therefore different NCs size. Increased residence time gives longer time for the nanoparticles to grow and thus increase its size.

## **2.6 Results and Discussions**

Several characterization techniques have been used to find out the nanoparticle properties, its crystallinity and size distribution.

### **2.6.1 Transmission Electron Microscopy (TEM) Analysis**

TEM studies have been performed to characterize the nanoparticle size and its microstructure. Microscopy was performed by Dr. Fan at the Center for Advanced Microscopy, using a JEOL 2200 FS ultra-high resolution microscope. We used graphene-coated copper grids and deposited GaN NCs using drop-casting from ethanol. We started off with lower power (around 60W) and with tube B. The main reason to start with the small tube was to have increased power density with same supplied power as compared to bigger tubes.

The flow conditions were same for both cases and were Ar = 60 sccm, NH<sub>3</sub> = 65 sccm and TMGa = 1 sccm respectively. Fig. 4.3(a) and (b) indicates amorphous material for 110W supplied power, as does the SAED pattern (bright rings in the SAED pattern indicates a crystalline sample). In contrast, for 130W supplied power, both the bright-field imaging (Fig. 4.3(c)) and the selected-area electron diffraction (Fig. 4.3 (d)) indicate crystalline material. This is the same phenomenon we observed for SiNCs: with increased power, crystallinity of nanoparticles improves. The described conditions led to synthesis of crystalline GaN NCs of diameter ~ 3-4 nm, as confirmed from bright-field TEM images.

GaN is known to exist in at least two crystalline polymorphs: the equilibrium wurtzite structure (hexagonal) and the metastable zinc blende structure (cubic). A third polymorph, rock

salt, is only formed under high pressure. Wurtzite phase of GaN crystal is thermodynamically stable at ambient conditions, while the zinc blende form of GaN crystal structure is metastable and is only achieved in extreme conditions.

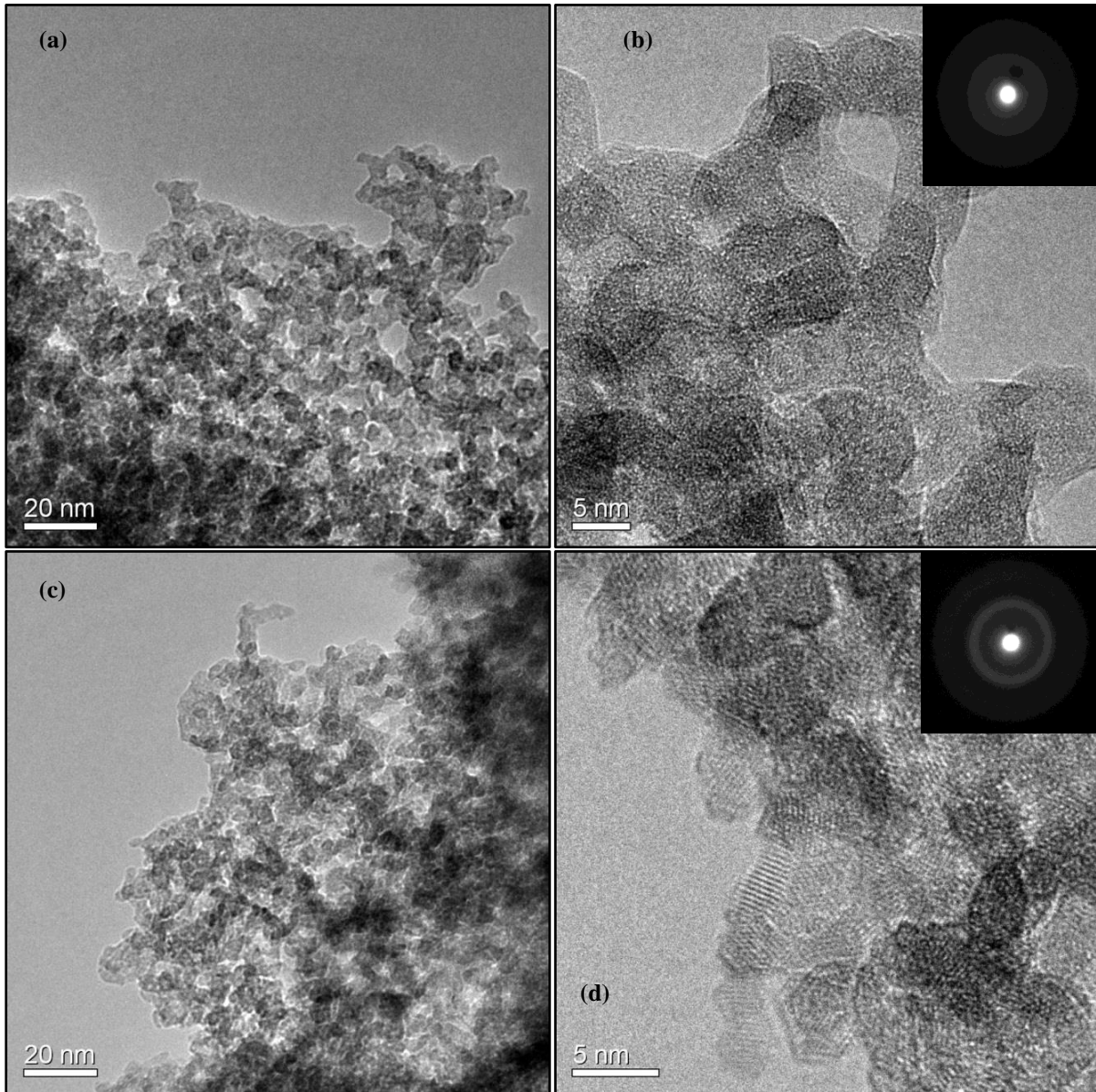


Figure 4.3: TEM images of a cluster of GaN nanoparticles at different supplied powers. (a) and (b) show low level of crystallinity at 110W. (c) and (d) show high level of crystallinity at 130W. The inset in (b) and (d) shows the SAED pattern.

To confirm the crystal structure of the GaN NCs, we have analyzed these high resolution bright field TEM images using ImageJ software<sup>114,115</sup>. To measure the spacing of the atomic planes from GaN single crystals, we used profile plots as well as Fast Fourier Transform (FFT) and the results are shown in Figure 4.4.

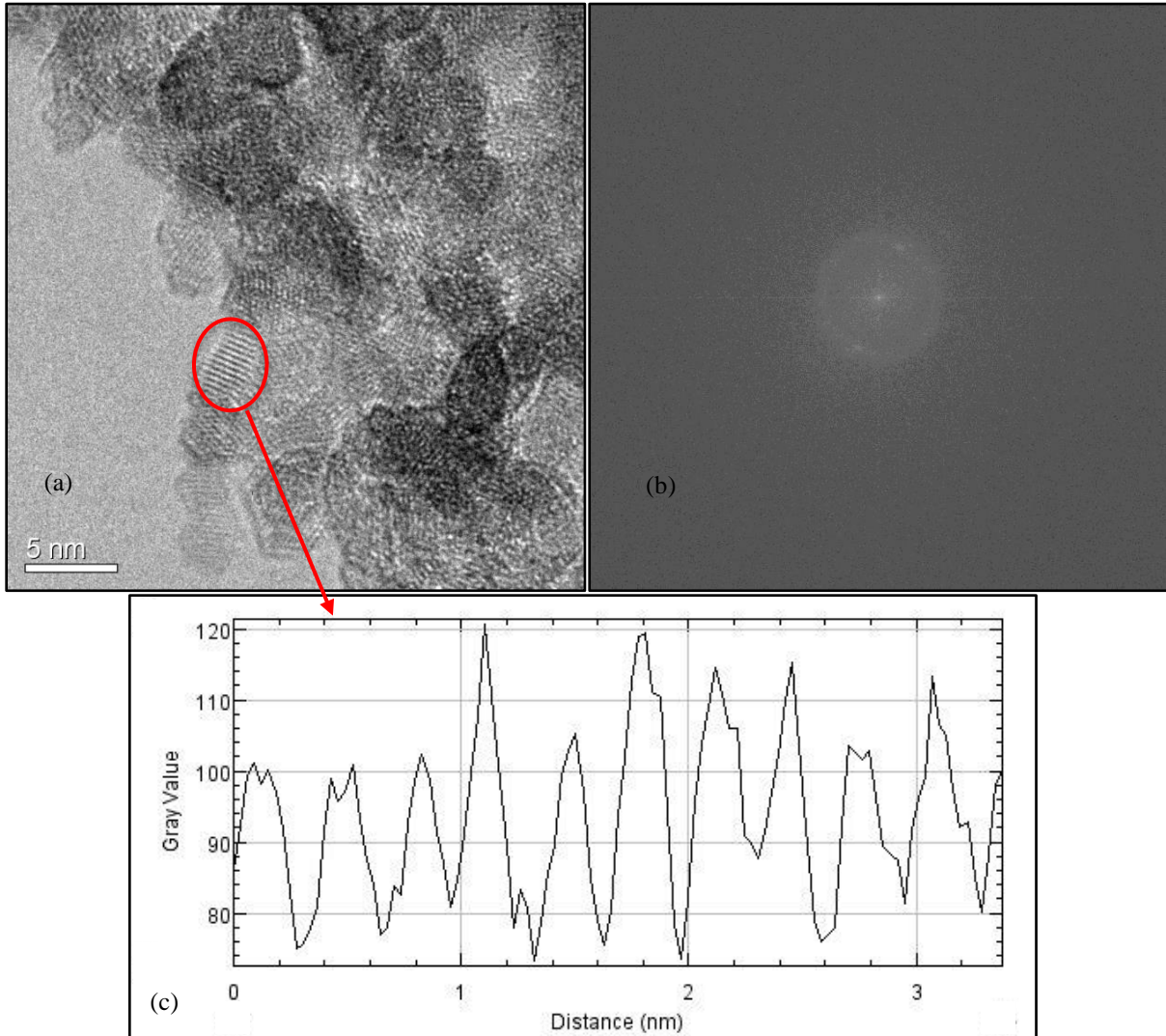


Figure 4.4: (b) FFT and (c) Profile plot of a Single crystal GaN from TEM image (a).

From the profile plot (Fig. 4.4(c)), we calculated the lattice spacing as the total number of cycles divided by the total distance. To get more accurate data, averaging has been performed for

around 20-30 single GaN NCs and the average value of lattice spacing has been found to be  $\sim 3.16 \text{ \AA}$  ( $\pm 0.04 \text{ \AA}$ ), which is very close to the hexagonal lattice constant ( $3.189 \text{ \AA}$ ). FFT measurements were performed to verify the profile plot results and were found out to be in good agreement with it. Our data indicates that we have synthesized hexagonal (wurtzite) GaN NCs.

Table 4.1 Physical properties of different crystal structure of GaN

Physical Properties (300K)	Hexagonal GaN	Cubic GaN	Reference
Energy band gap (eV)	3.39	3.2	Levinshtein, <i>et al.</i> 2001 <sup>116</sup>
Density (g/cm <sup>3</sup> )	6.15	6.15	Levinshtein, <i>et al.</i> 2001 <sup>116</sup>
Melting point ( <sup>0</sup> C)	2500	2500	Porowski, 1997 <sup>117</sup>
Lattice constant ( $\text{\AA}$ )	a=3.189, c=5.186	a=4.52	Levinshtein, <i>et al.</i> 2001 <sup>116</sup>
Thermal conductivity (W/cm·K)	2.1	2.1	Florescu, <i>et al.</i> 2000 <sup>118</sup>
Heat capacity (J/mol·K)	35.3	35.3	Krukowski, <i>et al.</i> , 1999 <sup>119</sup>
Bulk modulus (GPa)	210	210	Kucheyev, <i>et al.</i> 2000 <sup>120</sup>

## 2.6.2 X-ray Diffraction (XRD) Analysis

To strengthen our conviction that we have crystalline GaN nanoparticles and to double check with the TEM results, we performed XRD measurements. The results are shown in Fig. 4.5. As seen from the pattern, the GaN NCs display broad peaks centered at  $2\theta$  values of  $35^{\circ}$  and

60° respectively. These broad diffraction bands could point towards the metastable cubic phase of GaN NCs<sup>121-123</sup>. But, we already have verified that we have hexagonal (wurtzite) structure GaN NCs from ImageJ analysis of the TEM images. Moreover, it is also mentioned in literature that the broad diffraction peaks could also be due to their very small size (~2-4 nm)<sup>97</sup> as the XRD peaks are broadened due to small crystallite size. For wurtzite GaN, diffraction peaks should be at  $2\theta = 32.4^\circ, 34.6^\circ, 36.9^\circ, 48.3^\circ, 57.9^\circ, 63.6^\circ$  and  $69.2^\circ$ . Some of these peaks are shown in Figure 4.5 with bar.

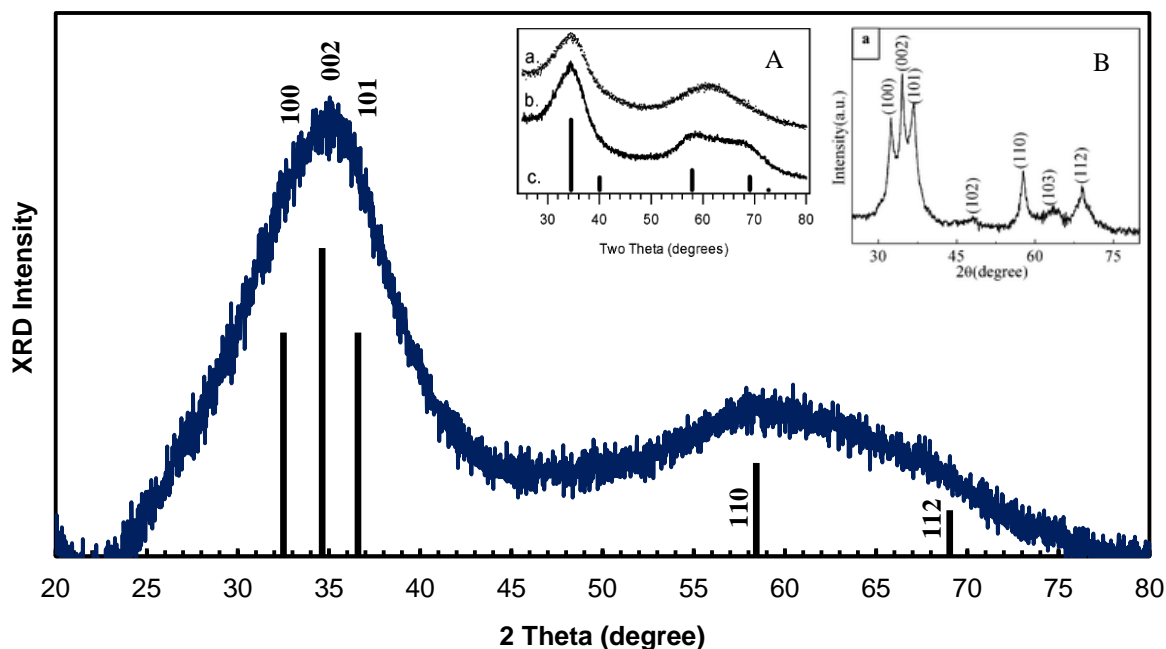


Figure 4.5: XRD pattern from GaN NCs (with inset (A) from ref. 121,123 showing XRD pattern for zinc blende GaN NCs with similar range of nanoparticle size and inset (B) from ref. 124 showing XRD pattern of hexagonal GaN NCs with bigger size).

### 2.6.3 Raman Vibrational Spectroscopy

To verify the crystallinity (as observed from TEM and XRD analysis) and to validate the hexagonal crystal structure (wurtzite) of GaN, Raman vibrational spectroscopy has been performed. We have used a HORIBA Jobin-Yvon LabRAM ARAMIS Raman confocal

microscope/spectrometer from CMSC, MSU to perform spectroscopic analysis. A 532 nm laser was used to excite the sample.

The spectra were taken at ambient temperature through a microscope, and the substrate used for these samples were glass microscope slides. Figure 4.6 shows the Raman spectrum of the as-produced sample in the range of 200-800  $\text{cm}^{-1}$ . One dominant broad peak with Raman shift of 568  $\text{cm}^{-1}$  appears in the high frequency range. In the low frequency range, two broad peaks at 306  $\text{cm}^{-1}$  and 446  $\text{cm}^{-1}$  and a small peak at 366  $\text{cm}^{-1}$  are visible.

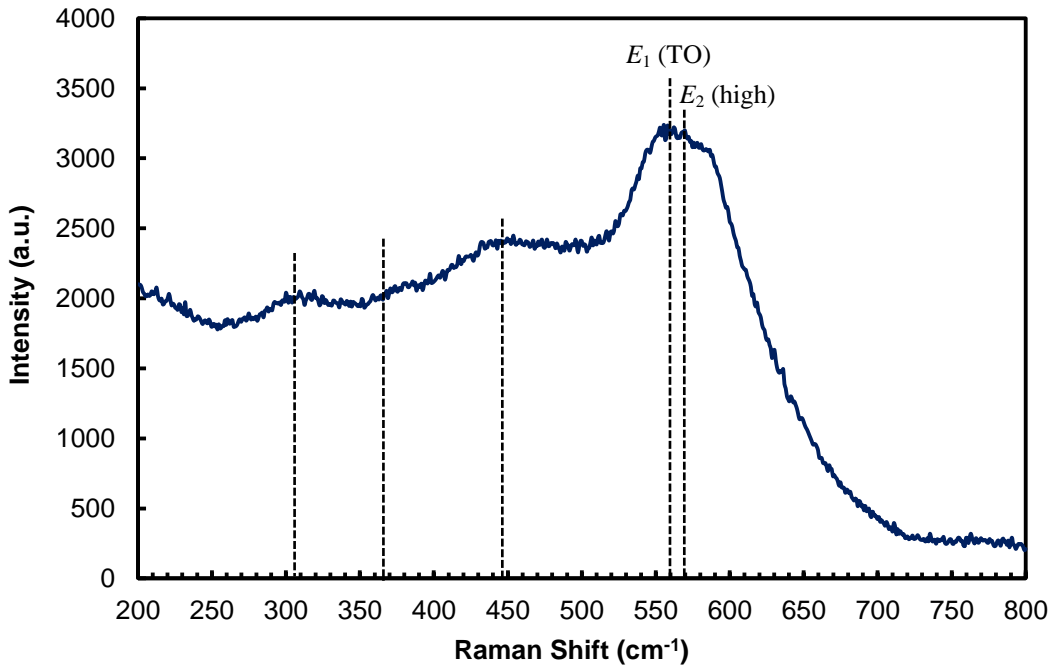


Figure 4.6: Raman vibrational spectra of as-synthesized nanocrystalline GaN

By comparing our results with the experimental data and phonon frequencies of GaN crystal available in literature<sup>103,125,126</sup>, the strongest peak centered at 568  $\text{cm}^{-1}$  can be assigned to the  $E_2$  (high) mode as observed for bulk GaN. There seems to be another peak at 560  $\text{cm}^{-1}$ , which can be assigned to the optical modes of  $E_1$  (Transverse Optical, TO). The peaks found at 306  $\text{cm}^{-1}$ , 366  $\text{cm}^{-1}$  and 446  $\text{cm}^{-1}$  could be from the borosilicate glass used as a substrate<sup>127,128</sup>. Also, there

could be some extra peaks which are unexpected to occur in an ideal bulk crystal. New Raman peaks appearing in a nonideal GaN crystal are most likely from “disorder-activated” Raman scattering (DARS). The appearance of the DARS spectra could either be due to damaged GaN films or due to high density of defects or amorphous films<sup>129–131</sup>. Presence of any defects or impurities in our samples can be detected by the XPS and PL spectra analysis and will be discussed later.

This spectroscopic analysis validated the findings from TEM and XRD analysis that we synthesized nanocrystalline GaN. It also states that the crystal structure of our GaN NCs is not metastable cubic phase (zinc blende) as the TO phonon frequencies for cubic GaN<sup>132,133</sup> is in the range of 552-555 cm<sup>-1</sup>.

#### **2.6.4 X-Ray Photoelectron Spectroscopy (XPS) Analysis**

The stoichiometry of the as-prepared GaN NCs was checked by XPS. XPS spectra showed the presence of Ga, N, C and O in the as-produced sample. Source of carbon signal is most likely surface contamination, the carbon tape holder, and hydrocarbon contamination from instrument, reactor (pump oil) and from air. The oxygen contamination is likely attributed to little air exposure (transferring sample from the reactor to the glove bag). XPS spectra of Ga-2p<sub>3/2</sub> and N-1s are shown in Fig. 4.7 (a) and (b) respectively. Ga-2p<sub>3/2</sub> signal was detected at 1117.2 eV confirming the presence of GaN<sup>134</sup> as Gallium oxide (Ga<sub>2</sub>O<sub>3</sub>) is normally found at higher binding energies as mentioned in literature<sup>134,135</sup> (see inset of Fig. 4.7 (a), Ga-2p<sub>3/2</sub> : 1119.5 eV). So, we do not believe that the NCs are oxidized. Furthermore, N-1s spectra has one major and one minor contributions: major signal is centered at 397.4 eV (v1 in Fig. 4.7(b)) which is in agreement with nitride bonding formation<sup>134</sup>, the minor signal at 399.5 eV (v2 in Fig.

4.7(b)) relates to the nitrogen binding with a  $sp^3$  carbon<sup>123</sup>. Carbon presence was confirmed by C-1s spectrum centered at 284.8 eV (see Fig. 4.8) and might be from the C-H groups present at the sample surface. This can be verified by FTIR analysis (see Fig. 4.9).

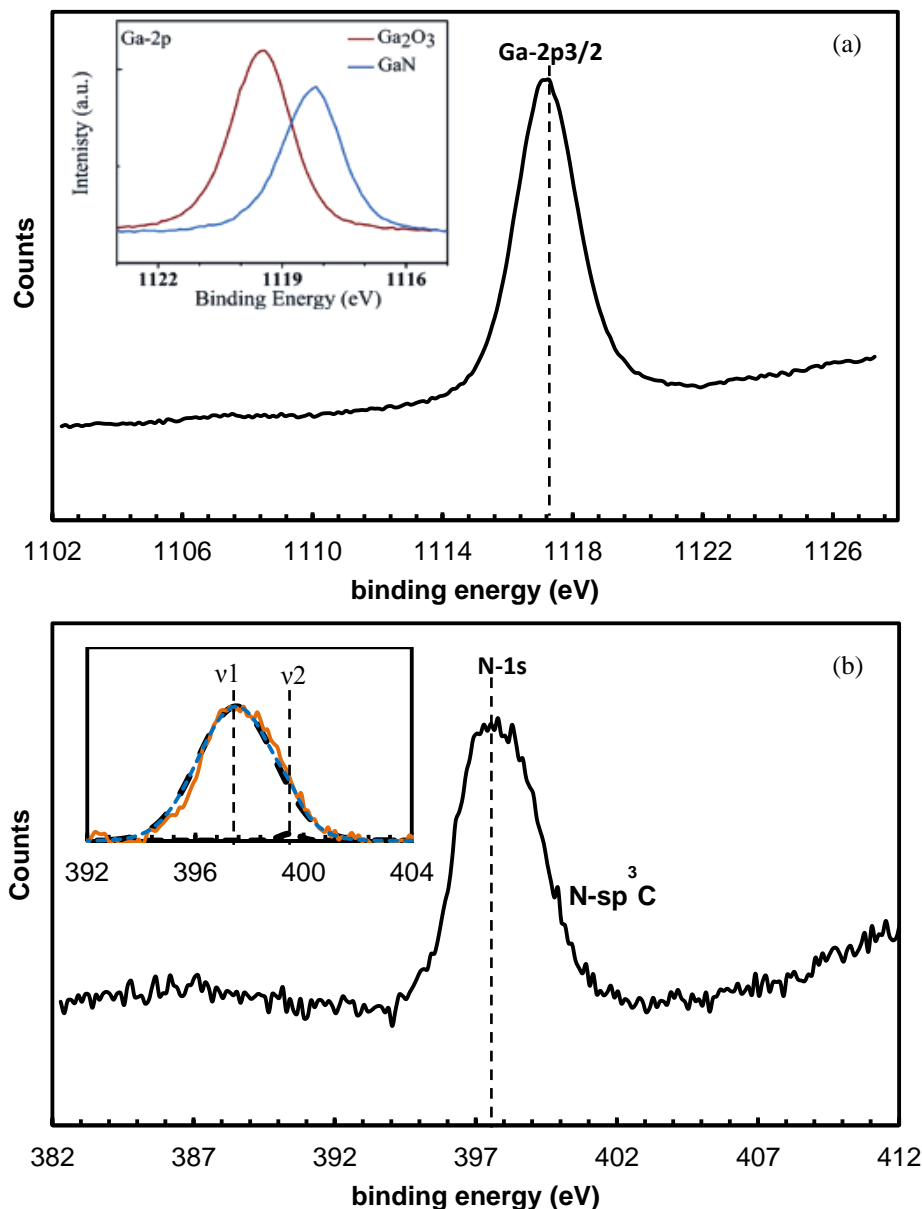


Figure 4.7: X-ray photoelectron spectroscopy signals of (a) Ga-2p<sub>3/2</sub> (with inset from ref. 134 showing difference in Ga-2p peak position for GaN and Ga<sub>2</sub>O<sub>3</sub> in terms of binding energy) and (b) N-1s from the as produced GaN nanocrystals (with inset showing deconvolution of N-1s spectra using two Gaussian lineshapes, N-1s spectra is shown in orange and overall fit is shown in blue).

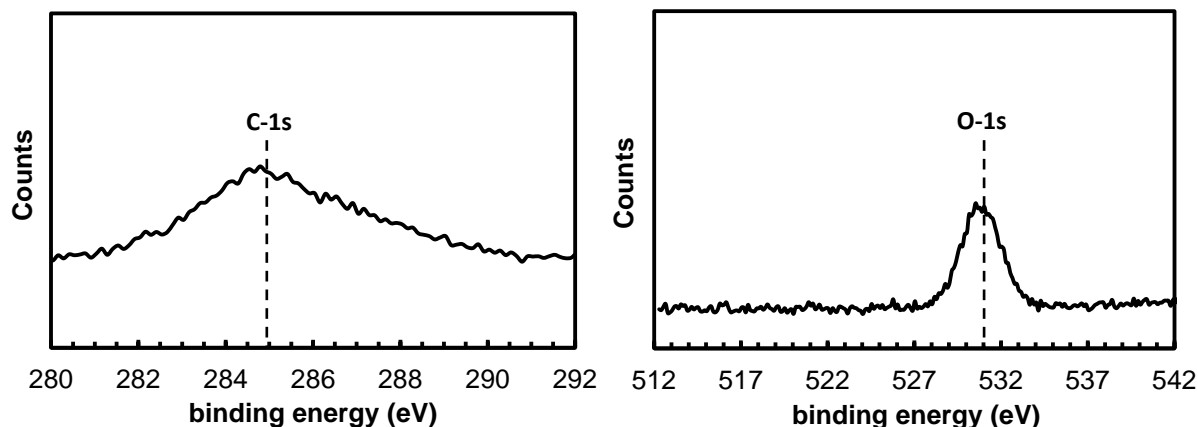
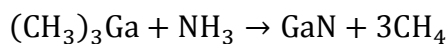


Figure 4.8: X-ray photoelectron spectroscopy signals of Carbon (C-1s) and oxygen (O-1s)

The presence of C-H groups could either be attributed to the incomplete reaction of precursor ((CH<sub>3</sub>)<sub>3</sub>Ga) or hydrocarbon contamination in the reactor or XPS instrument. The ideal reaction of GaN formation using TMGa and NH<sub>3</sub> is as follows:



The O-1s signal at 531 eV represents the contribution from C-O bonding. The XPS analysis evidently shows that we have synthesized GaN NCs successfully. We can also say that our sample was metallic gallium-free<sup>123</sup> as no signals were found below the binding energy of 1116 eV for Ga-2p.

Compositional analysis has also been performed with XPS. It shows Ga and N with 25.35 and 17.56 at % i.e. Ga:N ratio of 1.4:1.0. As discussed earlier, the presence of carbon (50.34%, due to interference from Ga Auger) is likely due to some contamination and oxygen content (6.75%) is due to little exposure to air while transferring the sample from the reactor to glove bag. Our ultimate goal is to achieve 1:1 ratio for Ga and N and therefore some future studies need to be performed to improve the measured stoichiometry.

Table 4.2 Composition analysis of GaN nanocrystals

Atomic Concentration Table				
C1s	N1s	O1s	Ga2p3	Comments
50.34	17.56	6.75	25.35	Atomic Concentration
± 5	± 2	± 1	± 1	Error

### 2.6.5 Fourier Transform Infrared Spectroscopy (FTIR) Analysis

In order to get an idea of the surface bonding of the nanoparticles, we performed FTIR (see Fig. 4.9). We obtained the FTIR spectra right after the deposition of nanoparticles, although they were exposed to air during measurement. The quick measurement and near-immediate spectra acquisition mean that any O-related peaks are from the sample and not from air exposure. A Bruker Alpha FTIR spectrometer has been used for this purpose in diffuse reflectance mode.

The measured absorption bands can be assorted into several groups. The strongest absorption is observed at  $600\text{ cm}^{-1}$  and is hypothesized to be the lattice vibration of crystalline GaN<sup>121,136</sup>. We also observe vibrational modes related to N-H ( $\nu$ ,  $\omega$ ,  $\tau$  and  $\delta$ ) from surface nitrogen bound to hydrogen. Small C-H<sub>x</sub> peaks ( $\sim 2900\text{ cm}^{-1}$ ) are present agreeing with the XPS analysis that showed slight C contamination.

Absorption band at  $1680\text{ cm}^{-1}$  represents bending vibrations which can be assigned to N-H<sub>2</sub> scissoring whereas absorption band at  $1000\text{ cm}^{-1}$  represents stretching vibrations for N-H<sub>2</sub>. C-H bending vibrations can be seen at  $1360\text{ cm}^{-1}$  which can be assigned to C-H<sub>x</sub> ( $x = 2,3$ ) deformation modes. We are unsure about the sharp absorption peak at  $2100\text{ cm}^{-1}$ , but it is presumably a byproduct from the precursors and could be assigned to C-O stretching vibrations. After the FTIR measurement, we have heated the sample at  $200^{\circ}\text{C}$  under nitrogen environment for 2 hours and measured the FTIR spectra again (see Fig. 4.10). As the sharp absorption peak at

2100  $\text{cm}^{-1}$  is almost gone after heating; we could infer that the peak was not part of actual sample. The absorption bands show the dominant presence of N–H group at the nanoparticle surface.

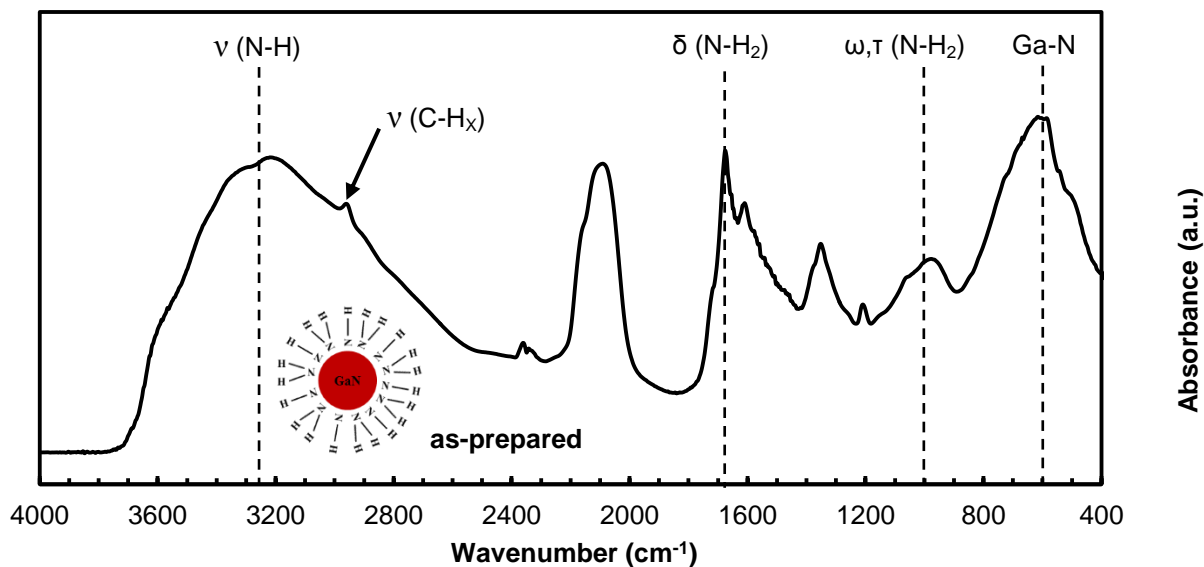


Figure 4.9: FTIR spectra from as-prepared GaN NCs (the inset image shows a possible configuration of GaN NCs)

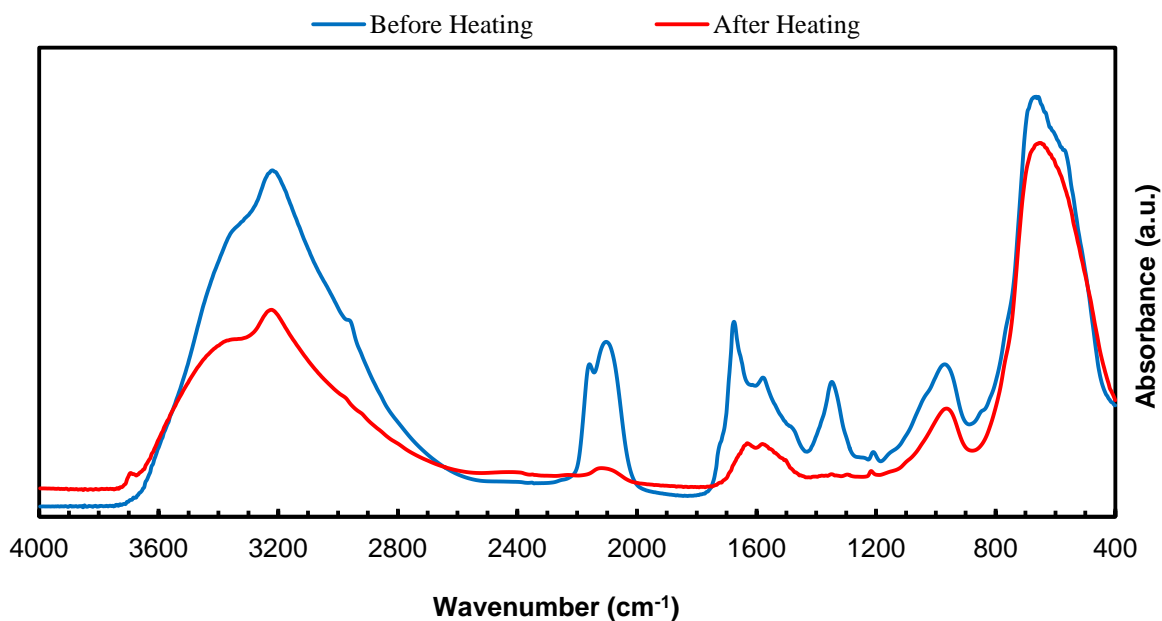


Figure 4.10: FTIR spectra from as-prepared GaN NCs (before and after heating).

## 2.6.6 Photoluminescence Spectra and Quantum Yield ( PL & QY)

We have performed PL measurements using an Ocean Optics, Inc. USB spectrometer and optical fiber. The PL was excited using a UV LED (peak at 325nm). The measurements were performed in air.

We did not observe any PL immediately after synthesis and waited few days after deposition. Based on the band gap of GaN (3.4 eV), the emission spectra should have been at ~ 365nm. However, for our sample, we couldn't find any emission spectra even after several days of deposition. This could be due to the presence of several defects or impurities in the sample surface as defects in GaN are very common. Also, it could be due to the fact that the intensity of the excitation source was not strong enough or the wavelength of excitation source was not suitable to excite the sample to get any PL. Another possible reason could be due to the presence of N-H as we know that N-H could quench the PL.

Defect emission from GaN is very common as it is very difficult to make stoichiometric GaN and could be attributed to surface states, impurities, and nitrogen vacancies<sup>137-140</sup>. For nitrogen deficient GaN (like our sample as confirmed by XPS results), researchers have observed broad peak at visible spectrum due to some trap states<sup>107,121</sup>. The Bohr radius of GaN is approximately 3nm<sup>141</sup> and as our TEM analysis showed, we have synthesized GaN NCs in the range of 2-4 nm; we expected to see quantum confinement from these NCs with PL being shifted to higher energies (i.e., lower wavelength). Also, the emission wavelength of amorphous GaN was reported to be longer than 400nm, both experimentally<sup>142</sup> and theoretically<sup>143</sup>. But, we have already showed that we synthesized crystalline GaN nanoparticles.

This is still under investigation and we are planning to use a laser with relatively higher intensity compared to LEDs and also with variable wavelength from 250 nm – 340 nm.

The absorption spectra (see Fig. 4.11) demonstrate that our as-prepared GaN NCs absorb light below 400nm, but beyond that there is very little absorption. This is in good agreement for a material (GaN) which has a band gap in the UV range.

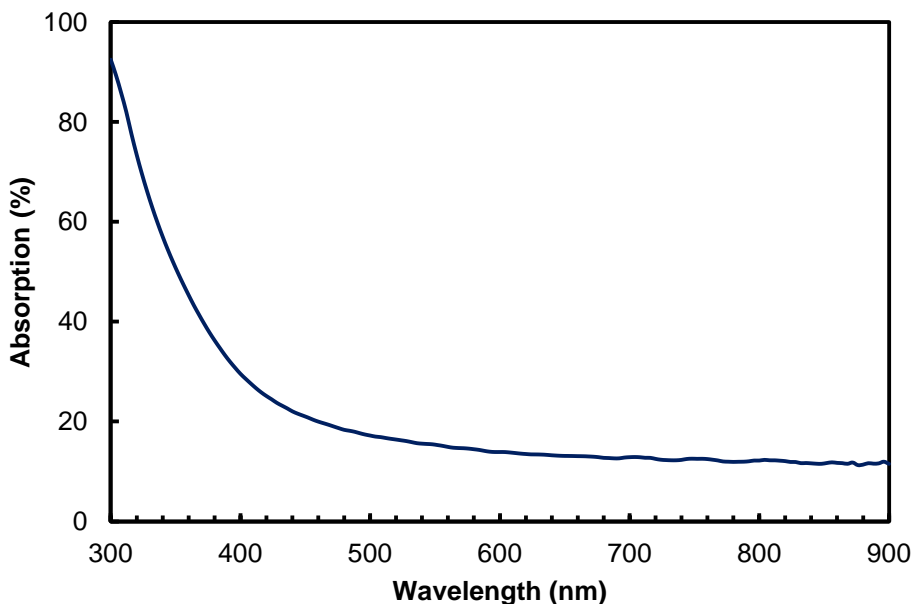


Figure 4.11: Absorption spectra from GaN NCs

### 2.6.7 Size-Tuning of GaN NCs using Plasma Reactor

GaN is one of the most popular semiconductor materials due to its band gap properties and has application in diverse areas. For white light emission technologies, GaN along with some color converting materials (phosphor) have been used widely<sup>144,145</sup>. But, group III–Nitride NCs itself has the prospect of high quality phosphors. Thus, there is a huge interest growing in controlling the PL peak of the GaN NCs during or after synthesis. This can be done either by doping/alloying<sup>145–147</sup> with other materials or tuning its size<sup>138</sup>. The objective of this work is to tune the GaN nanocrystal size and to investigate the effect of size tuning in PL spectra. In this way, we will be able to prove the versatility of our process.

To vary their size, GaN NCs were synthesized using different reactor geometries and different flowrates. The objective was to create different residence times for NCs inside the reactor. Residence time inside the plasma reactor can be calculated using the following equation.

$$t_{\text{res}} = \frac{\pi r^2 \times L \times P}{Q} \quad (4.1)$$

Here,  $r$  is the tube radius,  $L$  represents plasma length,  $P$  is the ratio of reactor pressure ( $P_r$ ) to atmospheric pressure ( $P_{\text{atm}}$ ) and  $Q$  is the total gas flowrate. Particle residence time is inversely proportional to the total gas flow rates. However, increasing the pressure increases the particle residence time. The glass tube diameter used in our reactor has similar effect on residence time as the pressure. For this part, two cases have been studied and the functional parameters are listed below.

Table 4.3 Residence Time Calculation

<b>Cases</b>	<b>Pressure (Torr)</b>	<b>Tube Radius (inch)</b>	<b>Plasma Length (inch)</b>	<b>Flowrate (sccm)</b>	<b>Residence Time(sec)</b>
Case 1	10	0.375	7	126	0.004235
Case 2	15	0.5	7	182	0.010504

The total flowrate for the first case was 126 sccm (Ar = 60 sccm, NH<sub>3</sub> = 65 sccm and TMGa = 1 sccm) with 114W (130W) RF power. Whereas for the second case, the total flowrate was 182 sccm (Ar = 85 sccm, NH<sub>3</sub> = 95 sccm and TMGa = 2 sccm) with 125W (150W) RF power.

The microstructural properties of GaN NCs were analyzed using TEM and XRD. For the first case, microstructural and optical properties have already been discussed which lead us to GaN NCs of size  $\sim 3\text{-}4$  nm in diameter. For the second case, as the residence time is almost double compared to the first case, we expected NCs with bigger size. TEM results are shown in Figure 4.12.

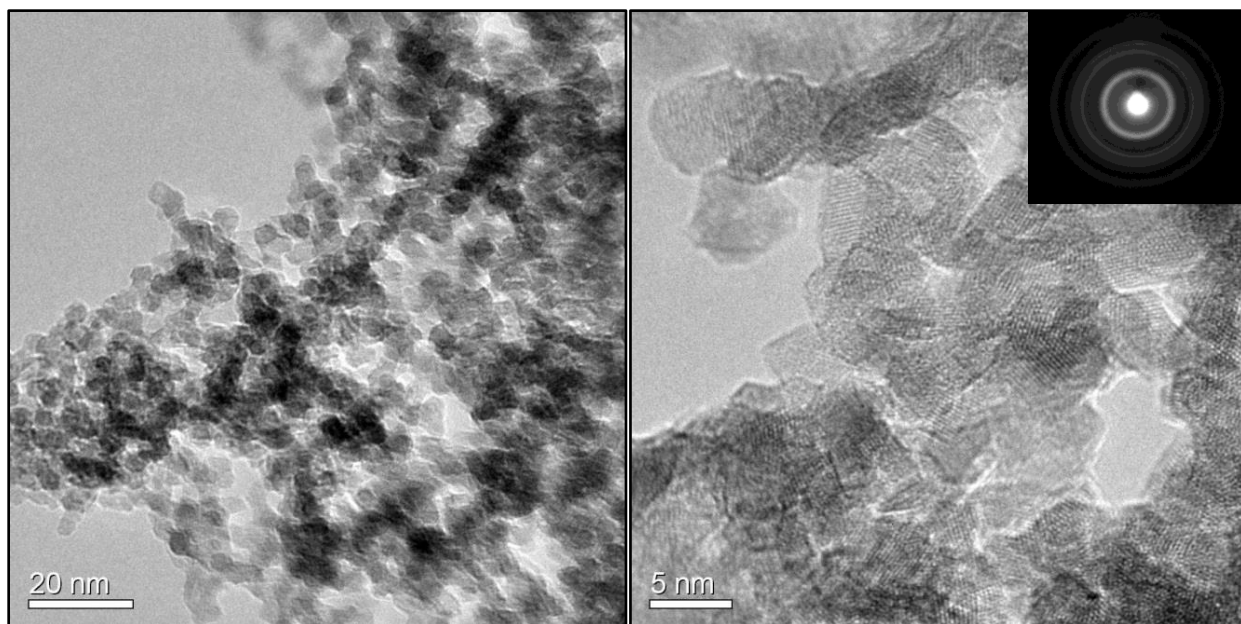


Figure 4.12: TEM images of a cluster of GaN nanoparticles with Ar = 85 sccm, NH<sub>3</sub> = 95 sccm, TMGa = 2 sccm and 125W (150W) RF power (for Case 2). The inset is showing the selected-area electron diffraction (SAED) pattern.

Both the bright-field imaging and the selected-area electron diffraction indicate crystalline material as the lattice fringes from GaN NCs are clearly visible. A statistical study has been performed from these TEM images using Image J software<sup>114,115</sup>. We have measured the individual nanocrystal size for maximum possible number of NCs from these TEM images and plotted a distribution (see Fig. 4.13).

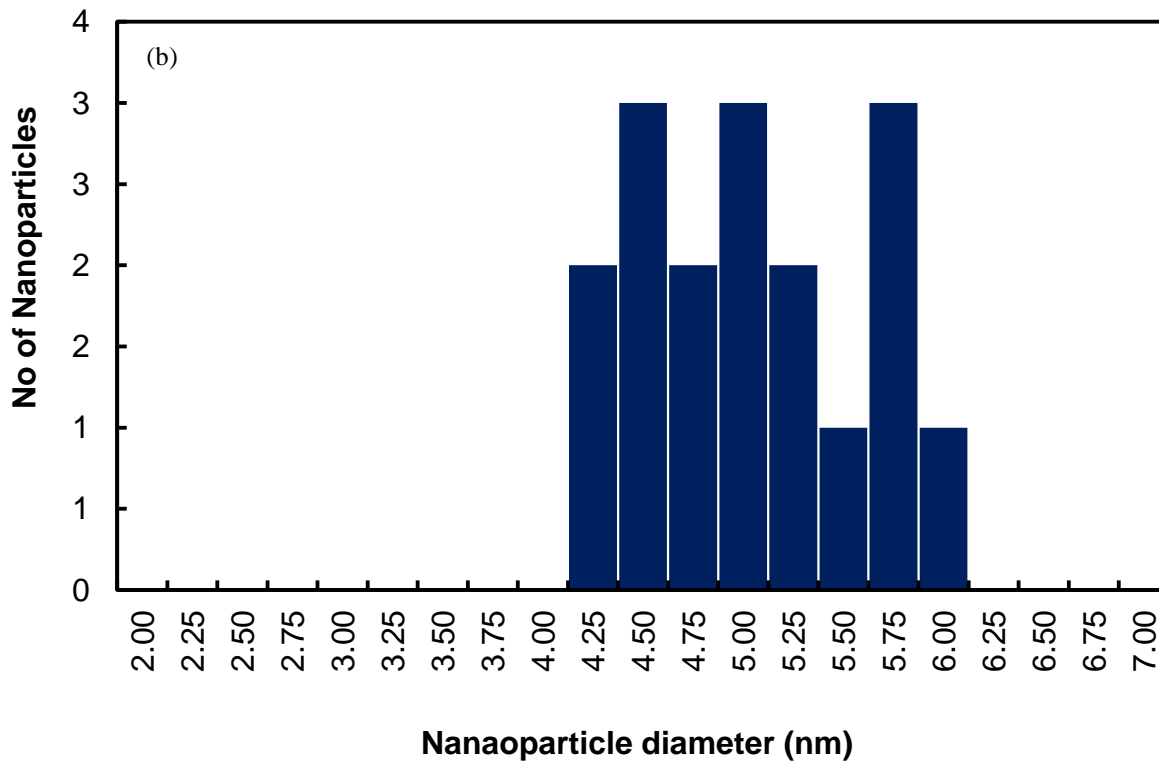
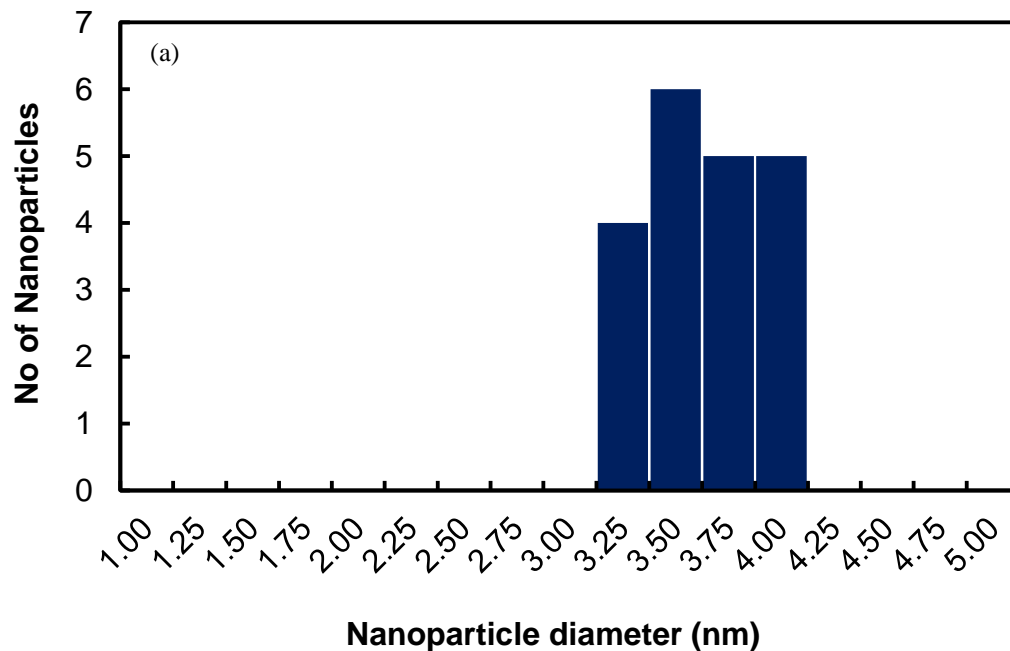


Figure 4.13: Nanoparticle size distribution for (a) Case 1: Ar = 60 sccm, NH<sub>3</sub> = 65 sccm, TMGa = 1 sccm and 114W (130W) RF power; (b) Case 2: Ar = 85 sccm, NH<sub>3</sub> = 95 sccm, TMGa = 2 sccm and 125W (150W) RF power.

Table 4.4 Nanoparticle size distribution for different cases

Case 1			Case 2		
Nanoparticle Index	Nanoparticle diameter (nm)	Error	Nanoparticle Index	Nanoparticle diameter (nm)	Error
1	3.6	±0.2	1	4.7	±0.2
2	3.0	±0.2	2	4.4	±0.2
3	3.1	±0.2	3	5.7	±0.2
4	3.7	±0.2	4	5.2	±0.2
5	3.8	±0.2	5	4.1	±0.2
6	3.4	±0.2	6	4.8	±0.2
7	3.6	±0.2	7	4.3	±0.2
8	3.8	±0.2	8	4.9	±0.2
9	3.4	±0.2	9	5.0	±0.2
10	3.2	±0.2	10	5.6	±0.2
11	3.7	±0.2	11	5.0	±0.2
12	3.5	±0.2	12	4.5	±0.2
13	3.4	±0.2	13	4.6	±0.2
14	3.2	±0.2	14	4.2	±0.2
15	3.3	±0.2	15	5.6	±0.2
16	4.0	±0.2	16	5.4	±0.2
17	3.7	±0.2	17	5.8	±0.2
18	3.8	±0.2			
19	3.9	±0.2			
20	3.3	±0.2			
<b>Mean</b>	<b>3.5</b>		<b>Mean</b>	<b>4.9</b>	
<b>SD</b>	<b>0.28</b>		<b>SD</b>	<b>0.55</b>	
<b>Min</b>	<b>3.0</b>		<b>Min</b>	<b>4.0</b>	
<b>Max</b>	<b>4.0</b>		<b>Max</b>	<b>5.8</b>	

From this distribution, we have compared the crystal size for both the cases. For the first case, the nanoparticle size distribution range is from 3-4 nm (Average size = 3.513 nm), whereas for the second case, the nanoparticle size distribution has a broader range from 4-6 nm (Average size = 4.932 nm) (see Table 4.4). This shows we can tune the nanoparticle size easily by changing certain parameters.

We attempted to verify the GaN nanoparticle size using XRD. The plots are shown in Figure 4.14. The substrate used for these samples was glass and the background has been subtracted from these signals. As it can be seen from the Fig. 4.14(a), we got two broad peaks centered at the  $2\theta$  value of  $35^\circ$  and  $60^\circ$  respectively for smaller nanoparticles ( $\sim 3-4$  nm). But, for bigger size GaN NCs ( $\sim 4-6$  nm), four broad peaks were observed at the  $2\theta$  value of  $35^\circ$ ,  $58^\circ$ ,  $63.5^\circ$ , and  $69^\circ$ . The lattice spacing ( $d$ ) as measured in TEM along with the diffraction pattern indicated that we synthesized wurtzite GaN NCs. It is very clear from these plots that as the nanocrystal size increases, a higher number of peaks become visible and the peaks become narrower which are what we expected based on reduced Scherrer broadening. These broad peaks yielded from XRD measurements are characteristic of nanosized crystalline GaN domains as discussed earlier. Some of the peaks are shown in Fig. 4.14 with bar.

Size-tuning of these GaN NCs is a very interesting phenomenon for optical applications. We can tune the emission wavelength by tuning the NC size. We tried to measure the PL from these bigger size GaN NCs but were unable to detect any signal from our setup. Future work will include synthesis of GaN NCs with even larger size. Although, we were able to show that by changing certain experimental parameters and reactor configurations, we can easily control/tune the GaN nanoparticle size.

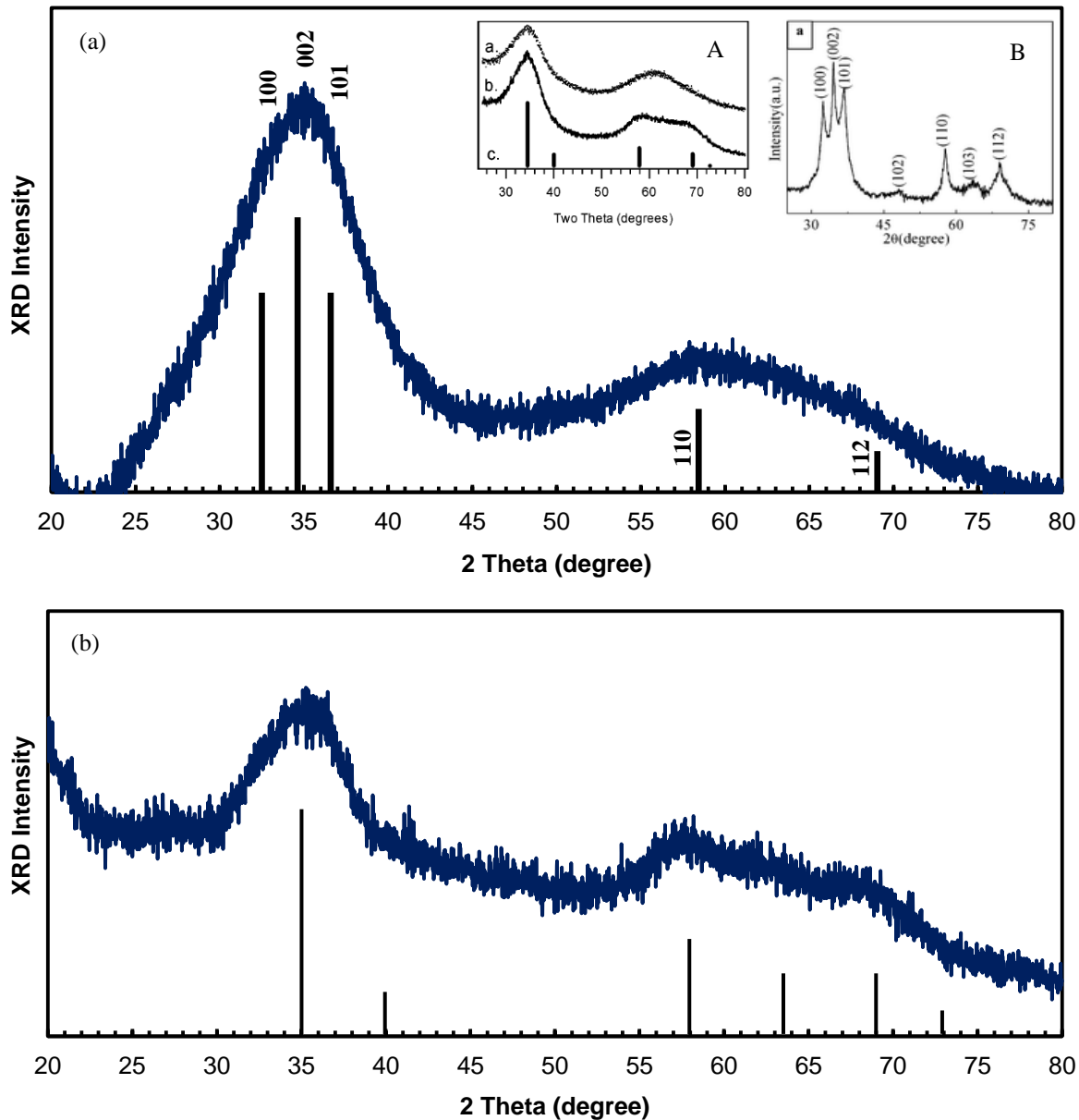


Figure 4.14: XRD pattern from GaN NCs for (a) Case 1 and (b) Case 2 (with inset (A) from ref. 121,123 showing XRD pattern for zinc blende GaN NCs with similar range of nanoparticle size and inset (B) from ref. 124 showing XRD pattern of hexagonal GaN NCs with bigger size).

## 2.7 Dual Plasma Synthesis

A dual plasma system has been designed (primary and secondary RF plasma) specifically to garner some advantages, such as, high reactive species density (due to the supply of more energy), heterogeneous nucleation, more control over the crystallinity of nanoparticles and its

surface properties. This concept has already been used for the gas-phase surface functionalization of Si NCs<sup>148</sup> in two step RF plasma process to attach hydrocarbons. Here, we have used this design for GaN NCs synthesis with the aim to improve its surface properties. The schematic of our dual plasma reactor is shown in Figure 4.15.

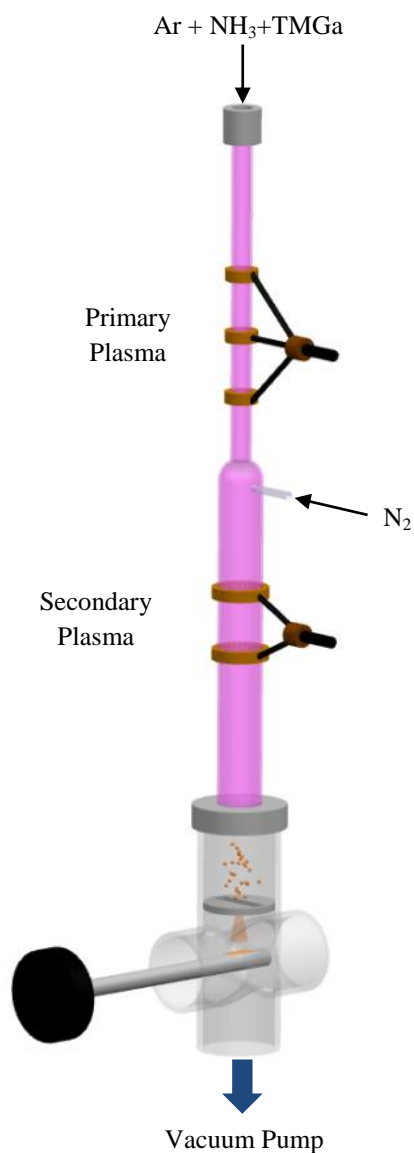


Figure 4.15: Schematic of the dual plasma reactor for the synthesis of GaN NCs.

The role of primary plasma (top) is to dissociate all the precursor gases and is responsible for initial growth of GaN nanoparticles. This growth of nanoparticles would continue to the

secondary plasma (bottom) and would help us in getting better surface coverage due to complete reaction of the gases. Nitrogen ( $N_2$ ) was flown through the side arm in between the two plasmas to get better nitride formation and surface coverage. This flow-through plasma reactor consists of a quartz tube with an outer diameter (O.D.) of 12.7 mm in the top portion and 25.4 mm in the bottom portion. The tube is 381 mm long and the expansion area is 177.8 mm from the top. Ar,  $NH_3$  and TMGa were flown through the quartz tube (entered through the contraction part with O.D. 12.7 mm, primary plasma) around which five ring copper electrodes were situated.

Three ring electrodes were used for the primary plasma, whereas, the secondary plasma had two ring electrodes. All the electrodes had same thickness of 10 mm. For primary plasma, the distance between the inside edges of the electrodes was 3.8 cm with the electrodes positioned in such a way that the upper edge of the top ground electrode would be 76 mm from the top of the quartz tube. The side arm has an O.D. of 6.35 cm and is located 2.5 cm below the junction point of contraction and expansion region. Another pair of electrodes was used for the secondary plasma and the gap between the inside edges of the electrodes was 2.5 cm with the top electrode being located 3.8 cm below the sidearm.

Two plasmas can be distinguished based on the emission color, where Ar/ $NH_3$ /TMGa plasma looks purple,  $N_2$  plasma is pink. GaN NCs were nucleated, grew in primary plasma and were transported to the downstream region (secondary plasma) by gas flow. The purpose of using secondary plasma was to provide enough energy for the dissociation of nitrogen atoms (N radicals) so that they can react and form bonds with the remaining precursors (if any) and also continue the nanoparticle growth process. This way GaN NCs were expected to form with better stoichiometric ratio, especially since nitrogen vacancy is a common defect in GaN.

The flowrates for the primary plasma was fixed with 60 sccm, 65 sccm and 1 sccm for Ar, NH<sub>3</sub> and TMGa respectively. N<sub>2</sub> flowrate was varied from 0 – 100 sccm. Therefore, pressure also varied from 7.5 – 15 Torr. The RF power used for the primary plasma was 150W (same as the single plasma synthesis) with secondary plasma power varied from 10W – 40W. The generated GaN NCs were collected on different substrates using impaction technique and kept in open air.

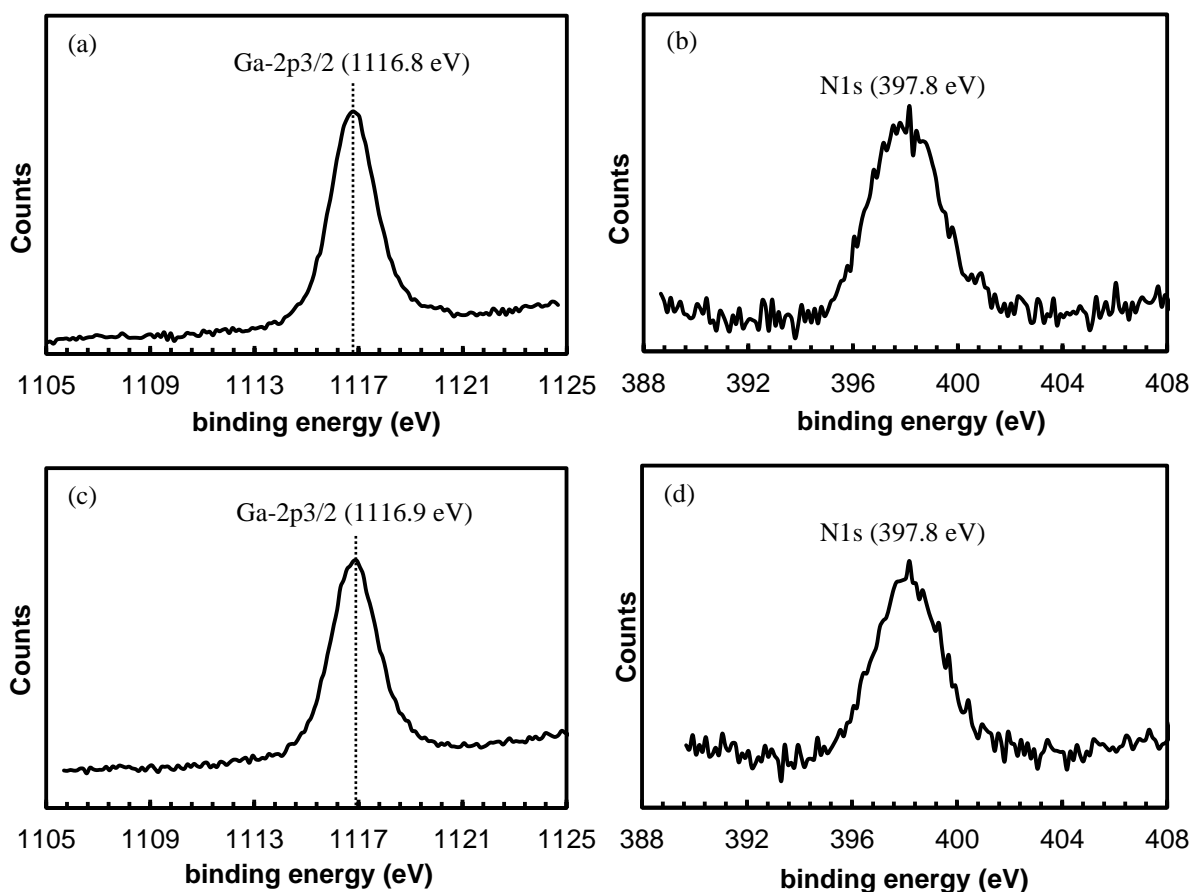


Figure 4.16: XPS signals of Ga-2p<sub>3/2</sub> and N1s from as produced GaN NCs synthesized using straight tube dual (a) & (b) without N<sub>2</sub> through the side arm, (c) & (d) with 50 sccm N<sub>2</sub> through the side arm.

These NCs were characterized using XPS and TEM. Figure 4.16 shows the XPS spectra of GaN NCs, specifically Ga-2p<sub>3/2</sub> and N-1s signals from two different samples. Ga-2p<sub>3/2</sub> peak at 1116.8

eV and 1116.9 eV for samples synthesized without N<sub>2</sub> and with 50 sccm N<sub>2</sub> respectively indicated the formation of GaN<sup>134</sup>. Also, both the samples had N-1s signals centered at 397.8 eV, which represents nitride bonding formation<sup>134</sup>. Although, we had signals from C and O apart from Ga and N, we do not believe the NCs were oxidized as Ga-2p<sub>3/2</sub> peak for Ga<sub>2</sub>O<sub>3</sub> occurs at higher binding energies as compared to GaN (~ 1119.5 eV)<sup>134,135</sup>.

The presence of oxygen could be attributed to the little exposure of sample to air while transferring and the source of carbon is likely due to hydrocarbon contamination from air and instrument. Furthermore, the absence of significant contribution at binding energy lower than 1116 eV gave indication of metallic gallium-free material synthesis<sup>123</sup>. Composition analysis has also been performed using XPS data for both the samples.

For the sample synthesized without N<sub>2</sub>, Ga:N was found out to be approximately 1:1. Whereas, the sample synthesized with 50 sccm N<sub>2</sub>, Ga:N was found to be 1: 1.4, which is in agreement with added N<sub>2</sub> flowrate. As discussed earlier in this chapter, with single plasma synthesis, Ga:N was 1.4:1 and the goal was to improve the ratio with dual plasma synthesis. By comparing all the data, we can definitely say that dual plasma has helped in getting stoichiometric GaN NCs.

TEM analysis has been performed to characterize the size and microstructure of these NCs and is shown in Figure 4.17. We have tried to show the effect of secondary plasma power by comparing two different powers. As it can be seen from the Figure 4.17, higher secondary power helps in getting better crystallinity. With 40W secondary power, crystal lattice planes are more prominent and bright rings in the SAED pattern also indicates better crystallinity as compared to the 20W secondary power. As the nanoparticle would have more time to grow

during dual plasma synthesis (due to extended plasma length), we expected the size of the NCs to be bigger than the single plasma synthesis. By quantifying the TEM images, the average size of the NCs was found out to be  $\sim 5.3$  nm, which is bigger than the NCs synthesized with single plasma under the same conditions ( $\sim 3.5$  nm).

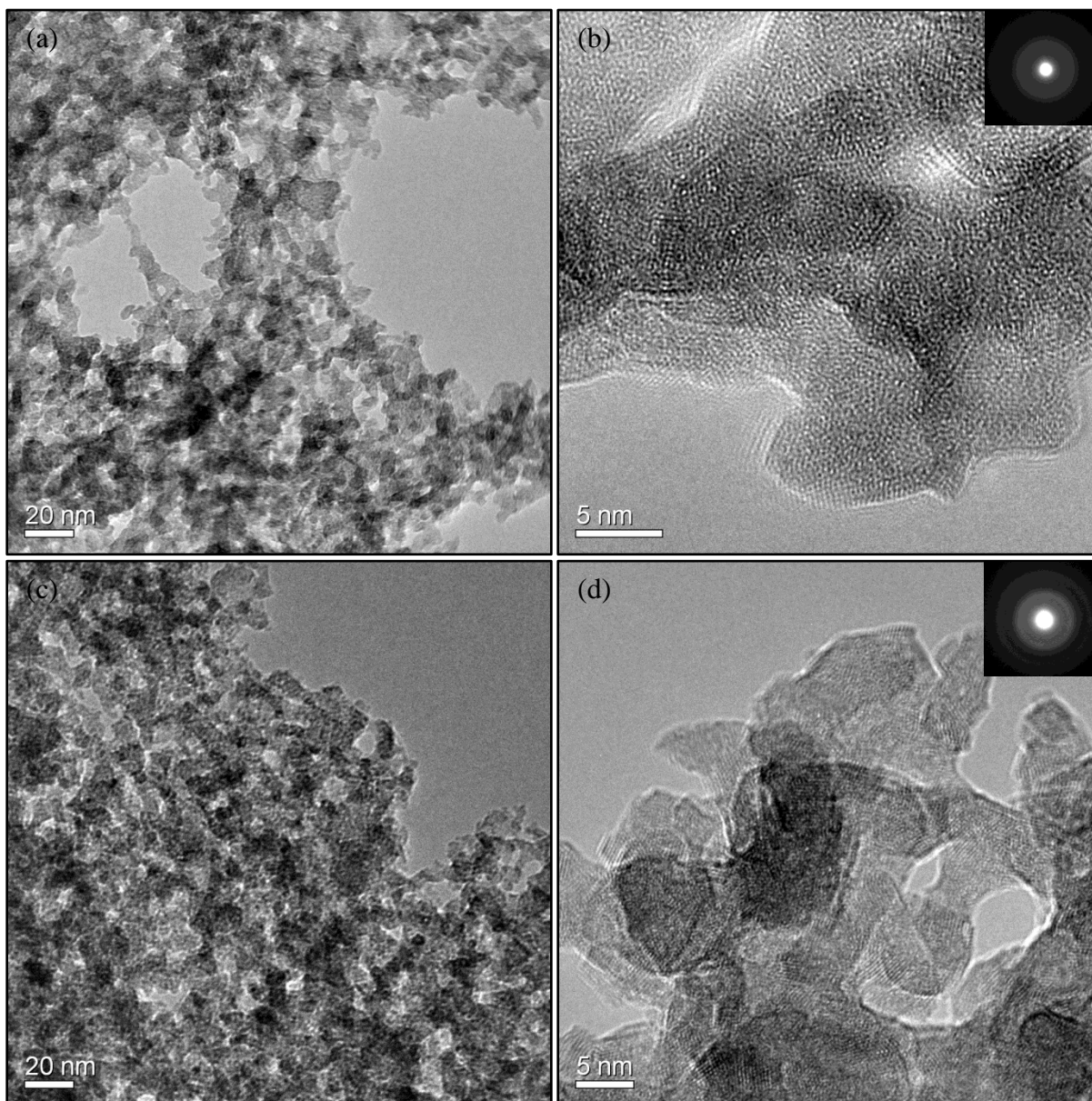


Figure 4.17: TEM images of GaN NCs synthesized from dual plasma reactor with varying secondary plasma power: (a) & (b) 20W and (c) & (d) 40W. The inset in (b) and (d) shows the corresponding SAED pattern.

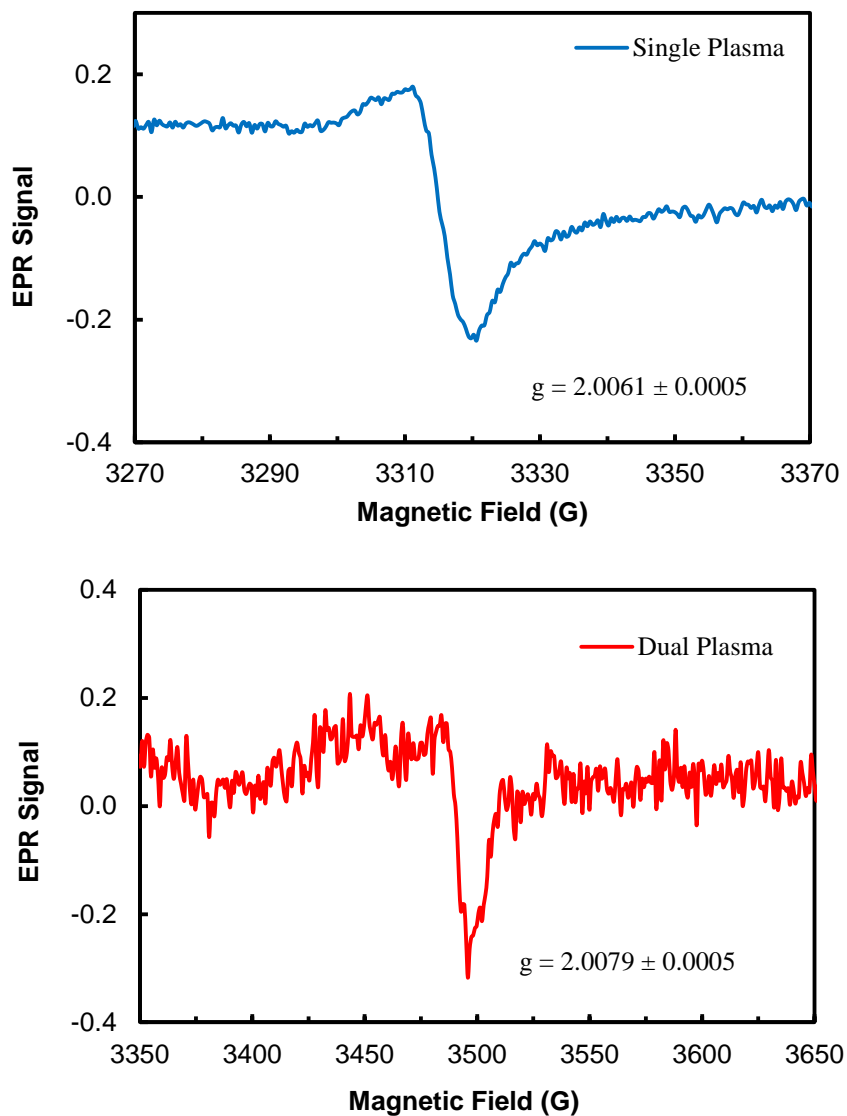


Figure 4.18: EPR spectra from GaN NCs synthesized using Single Plasma and Dual Plasma

EPR measurement was performed to identify and quantify any defects present in the as-produced GaN NCs. We have used a Bruker ELEXSYS-II E580 spectrometer to perform the EPR measurement and the results are shown in Figure 4.18 and Figure 4.19. In Figure 4.18, we have compared the EPR spectra from GaN NCs synthesized using single plasma and dual plasma. Both the samples were prepared using 60 sccm Ar, 65 sccm  $\text{NH}_3$ , 1 sccm TMGa and 150W power (secondary plasma power was 40W for dual plasma setup). After deposition,

samples were kept in glove box until the EPR measurement and the measurement was performed under room conditions. Corresponding  $g$ -values are also displayed in Figure 4.18 ( $g$ -value represents a specific type of dangling bonds in EPR study).

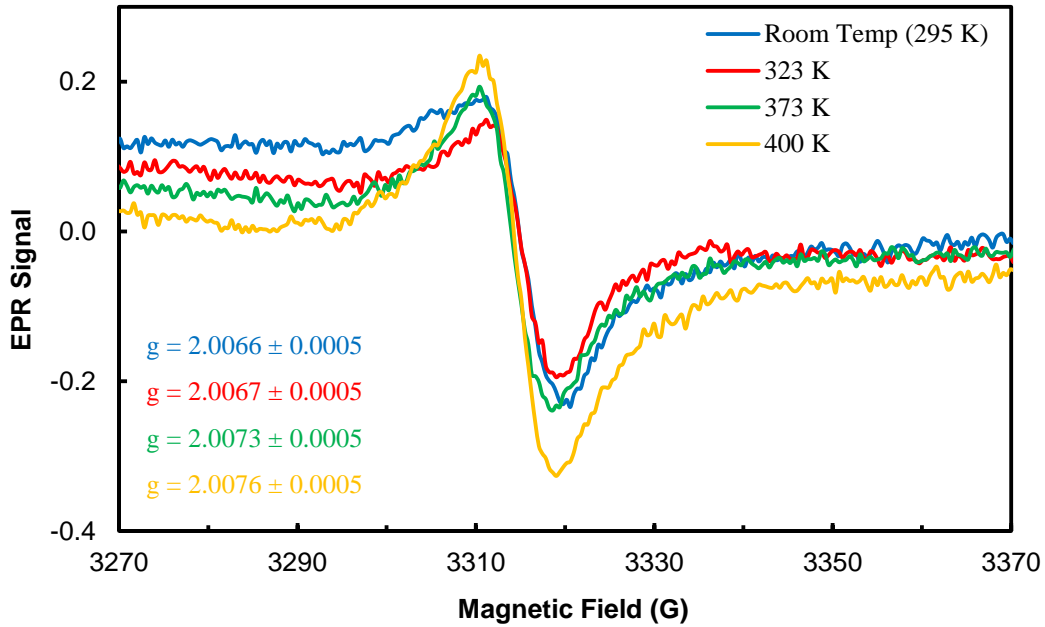


Figure 4.19: EPR spectra of Single Plasma synthesized GaN NCs at different temperatures

GaN usually contains several defects due to its high cohesive energy and these defects can influence its electronic and optical properties<sup>149</sup>. The problem is that most of these defects in GaN are unknown until now except few like Ga interstitial<sup>150,151</sup>, Ga monovacancy<sup>152</sup>, nitrogen split interstitial<sup>149</sup> etc. Based on the  $g$ -value of single plasma synthesized GaN NCs, defects could be attributed to  $V_{Ga}V_N$  divacancy ( $g \sim 2.0059$ )<sup>149</sup>. Isolated  $V_{Ga}$  ( $g \sim 2.0051$ ) and  $V_{Ga}O_N$  pairs ( $g \sim 2.0049$ ) also has  $g$ -values close to  $V_{Ga}V_N$  divacancy<sup>149</sup>.

But for the dual plasma synthesized GaN NCs, which has  $g = 2.0079$ , we could not assign the type of defects and it is still under investigation. But, we can presumably say that the defects have decreased with dual plasma synthesis as the EPR amplitude (signal) has decreased.

Additionally, there is a change of line shape for dual plasma sample and the EPR spectrum is not symmetric.

We have also studied the effect of heating on GaN NCs using the EPR spectra. NCs were synthesized using single plasma and the sample was heated from room temp to 400K under room conditions. EPR spectra were recorded at four different temperatures and are presented in Figure 4.19. We observed that with heating, the line shape of EPR spectra has changed and became more symmetric. We also found out that the  $g$ -values have increased with increasing temperature. This is very interesting phenomena and might indicate to the defects with metastable configurations<sup>153,154</sup>.

## **2.8 Conclusions**

In this chapter, we have demonstrated the all-gas-phase synthesis of GaN NCs. This process allowed us to deposit the GaN NCs directly from gas-phase onto the substrates giving us more freedom in choosing substrates. These nanoparticles were thoroughly characterized using TEM, X-Ray diffraction, Raman spectroscopy, XPS, FTIR, PL measurement and found out to be hexagonal GaN NCs with stoichiometric ratio of 1.4:1 (Ga:N). We have discussed the role of dual plasma synthesis in achieving proper stoichiometric (1:1) GaN NCs. To prove the versatility of this gas-phase process, different sizes of NCs were produced just by changing the reactor geometry and gas flow rates. This gas-phase process will definitely provide us with more options for substrates which can be used for GaN nanocrystal growth.

## CHAPTER 5

### Surface Nitridation of Silicon Nanoparticles using a Non-Thermal Plasma

#### 5.1 Introduction

Nano silicon acts as a direct bandgap material in contradiction to bulk silicon and can emit light. Due to its light emission capabilities and non-toxicity nature, silicon nanostructures has become a very hot topic from past decades as it has huge potential for application in optoelectronic technologies<sup>155–157</sup>. Several studies have been performed in the past decade on Si QD based light-emitting diodes (LEDs)<sup>20,21,60,158–161</sup> as the production cost is very low compared to other semiconductor material and it has complementary metal-oxide-semiconductor (CMOS) compatibility. Properties of Si QDs embedded in different matrix material like silicon oxide matrix<sup>162,163</sup> as well as silicon nitride matrix<sup>159,164–169</sup>, has also been studied extensively. Based on the recent theoretical and experimental studies, it is found out that Si QDs embedded in *silicon nitride* matrix has better optical characteristics than in silicon oxide matrix in terms of quantum size effect and emission efficiency<sup>159,164,165</sup>. Thus, *silicon nitride* matrix could be a great matrix material for application in silicon based LEDs.

Also, silicon nitride has lower tunneling barrier compared to silicon oxide<sup>170–172</sup> and therefore it will allow the transfer of electrons and holes to the Si QDs easily. It is also found out that the Si QDs embedded in nitride matrix emits in lower wavelengths as compared to in oxide matrix and the band gap can be tuned from 1.5 to 3.0 eV<sup>166,169</sup>. Silicon Carbide (SiC) has also been used in few studies<sup>173,174</sup> as a matrix material for Si QDs but it has similar characteristics of

an oxide matrix<sup>173,175</sup> in terms of energy levels. These insulating matrix materials make quantum structures more stable, but as it contain radiative defects or interface states, it may contribute to PL in terms of peak shift. Such states do not have any size dependency and therefore it is possible to distinguish the radiative mechanisms<sup>176–180</sup>. Additionally, hydrogenated Si<sub>3</sub>N<sub>4</sub> embedded QD structures are often amorphous<sup>164,165,181,182</sup>, whereas Si QDs in SiO<sub>2</sub> are usually crystalline. A wide range of luminescence has been observed in Si<sub>3</sub>N<sub>x</sub> by various researchers<sup>183,184</sup> which opens up the possibility of using silicon in fabricating full-color devices. Besides optoelectronics, these Si QDs embedded in a dielectric matrix also has huge potential for application in photovoltaics/solar cells<sup>25,175,185</sup>.

Some recent studies have also been performed on surface nitridation<sup>186</sup> or encapsulation<sup>187</sup> of silicon nanoparticles (Si NPs) using a plasma process. Encapsulated Si NPs with silicon nitride is a very promising anode material for lithium-ion batteries (LIBs) as silicon is abundant, inexpensive, has higher theoretical capacity and better stability in typical electrolytes as compared to the conventional anode material i.e. graphite<sup>188–192</sup>. Although Si has some drawbacks, nano silicon came out to be the alternative of bulk Si for using as an anode material for LIBs<sup>191,193–195</sup>. Although, carbon and SiO<sub>2</sub>-coated Si nanostructures are great anode material for LIBs, production of these nanostructures are mostly complex and multi-step process<sup>195–198</sup>. Silicon nitride (SiN<sub>x</sub>) is stable in atmospheric conditions and very useful as a surface barrier layer. So, it would be really useful to develop a simplified process to make surface-nitrided Si nanostructures for various applications. The main purpose of this work is about in-flight nitridation of Si NCs in a fully gas-phase flow-through plasma reactor and thereby to enhance its optical properties.

## 5.2 Experimental Details

Nitridation of bulk and nano Si surfaces have been done previously using  $N_2$  plasma and found out to be self-limiting at reasonable temperatures ( $300^{\circ}C$ – $800^{\circ}C$ )<sup>199–202</sup>. Temperature-dependent saturated thickness is also reported for nitridation of bulk Si surfaces with the thickest films being 3nm, at  $900^{\circ}C$ <sup>203</sup>. It is also demonstrated that  $SiN_x$  morphology is temperature dependent and amorphous  $SiN_x$  was detected for surface temperatures lower than  $500^{\circ}C$  with better distribution of nitride layer at higher temperatures<sup>202</sup>. Thus, plasma synthesis could be a great option for surface nitridation of Si nanoparticles while keeping the Si NC core intact. Here we are combining a plasma-based nitridation with an earlier-stage synthesis plasma in a flow-through process.

Here, production of Si nanoparticles and their surface nitridation were performed using a flow-through plasma reactor in a fully gas phase mode. The schematic diagrams of the plasma reactors are shown in Figure 5.1. As discussed earlier, same flow-through reactor is used here with few modifications. The tube is 304.8 mm long and the expansion region starts at 177.8 mm from the top for case 1 (see Fig. 5.1(a)), whereas for case 2 (see Fig. 5.1(b)), the expansion region starts at 127 mm from the top. Ar and  $SiH_4$  (1% in Ar) are flown through the quartz tube and a pair of ring copper electrode is wrapped around that tube. Nitrogen gas is flown through the sidearm which is situated 1cm below the junction point of the reaction zone and the expansion region. The position of these electrodes is different for different cases. For case 1 (see Fig. 5.1(a)), the ring electrodes are above the side arm and positioned in such a way that the bottom edge of the ground electrode will be 2 cm above the junction point of the reaction zone and the expansion region. The gap between the electrodes was kept at 2.54 cm. However, for case 2 (see Fig. 5.1(b)), the powered electrode was placed at the end of the reaction zone and the

grounded electrode was below the side arm with variable distance from the side arm. The thickness (width) of all the electrodes was around 1cm.

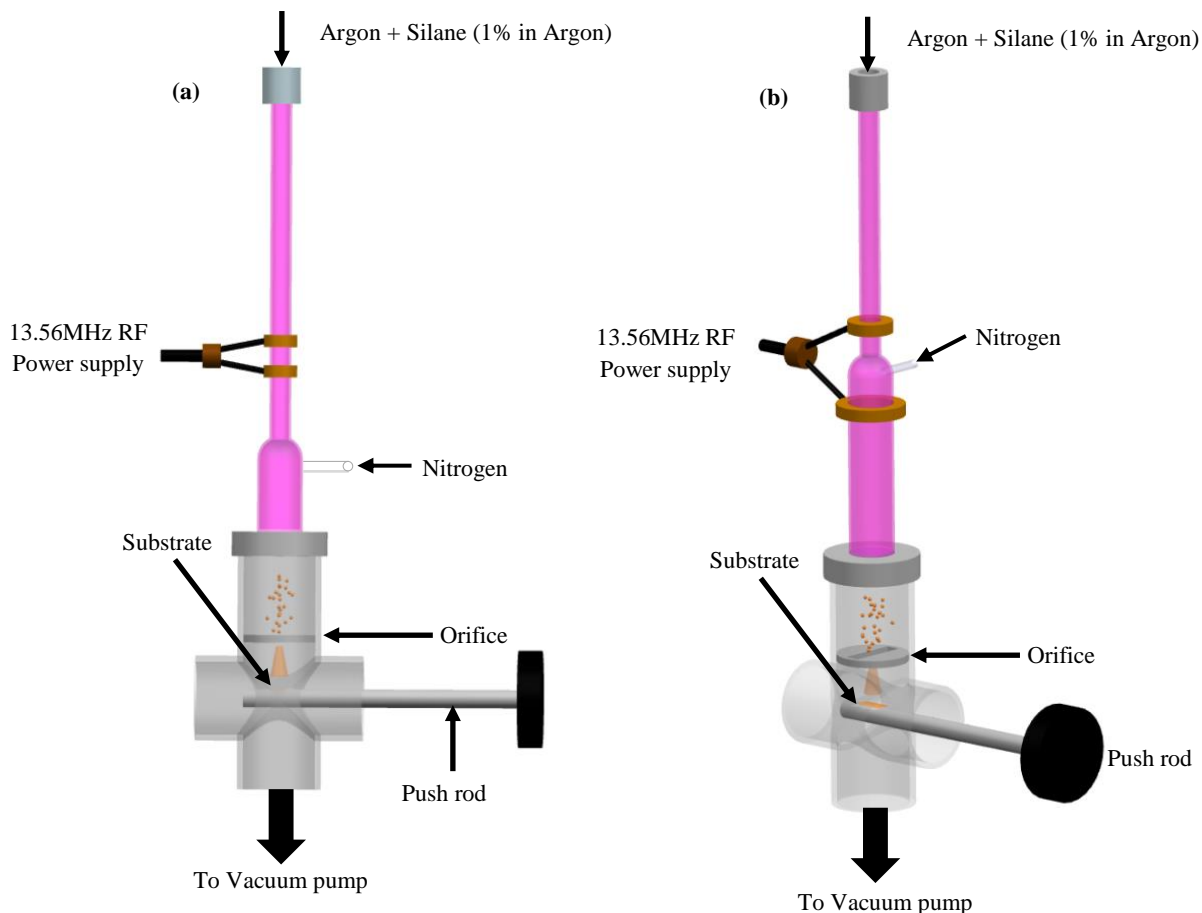


Figure 5.1: Schematics of the Plasma Reactor with (a) case 1 and (b) case 2.

The pressure was kept constant at 2.75 Torr (with the flowrates, Ar = 30 sccm, SiH<sub>4</sub> (1% bal. Ar) = 80 sccm) using an orifice plate. For surface nitridation of Si nanoparticles, we have flown N<sub>2</sub> through the side arm into the afterglow part of the plasma. Nitrogen and Argon flow rates was varied from 30 – 120 sccm and 30 – 60 sccm whereas silane flow rate was kept same. Pressure in the reactor also changed due to different combination of flowrates and was in the range of 2.7-3.4 Torr. The supplied power was 25W as discussed in the second chapter. These samples were mostly collected on glass via inertial impaction technique and were kept in open air environment.

### 5.3 Results and Discussions

The focus of this research is surface nitridation of Si nanoparticles in a single-step process. Si NCs synthesized using the same plasma reactor with the continuous flow of SiH<sub>4</sub> and Ar as described in the first chapter, without any nitrogen injection, are known to be crystalline and are H-terminated<sup>61</sup>. Our research hypothesis is that as we have added N<sub>2</sub> in the afterglow part of the plasma, the nanoparticle surface are expected to be covered with nitride layer.

In order to get an idea of the surface bonding of the nanoparticles, we have studied the FTIR (see Fig. 5.2). We performed right after the deposition of nanoparticles. A Bruker Alpha FTIR spectrometer was used for this purpose in diffuse reflectance mode. These Si nanoparticles were synthesized using 80 sccm of SiH<sub>4</sub>, 50 sccm of Ar and 25W of input power. The reactor design was same as shown in Figure 5.1(b) except the expansion region was shorter (127 mm) with total length remained same. We have compared three different cases of nitridation with different reactor configuration.

The FTIR spectra from Si NCs synthesized with and without H<sub>2</sub> flowing through the side arm look similar in terms of Si-H<sub>x</sub> (x = 1, 2, 3) peaks. For the no hydrogen injection case, the presence of H<sub>2</sub> could be attributed to SiH<sub>4</sub> precursor. For Si NCs, the absorption peak found around ~ 2100 cm<sup>-1</sup> is the combination of three different silicon hydride peaks: SiH (~ 2086 cm<sup>-1</sup>), SiH<sub>2</sub> (~ 2112 cm<sup>-1</sup>), and SiH<sub>3</sub> (~ 2136 cm<sup>-1</sup>)<sup>204</sup>. But, flowing hydrogen through the side arm would increase the concentration of SiH<sub>3</sub> species and lower the amount of SiH group's presence at the sample surface as can be seen from the plot<sup>61</sup>. The absorption bands at ~ 908 cm<sup>-1</sup> and ~ 865 cm<sup>-1</sup> represents Si-H<sub>x</sub> bending/wagging vibrations at the Si surface. The shoulder at ~ 1052 cm<sup>-1</sup> is due to very small partial surface oxidation of Si NCs as the samples were exposed to air while transferring from the reactor to the FTIR instrument.

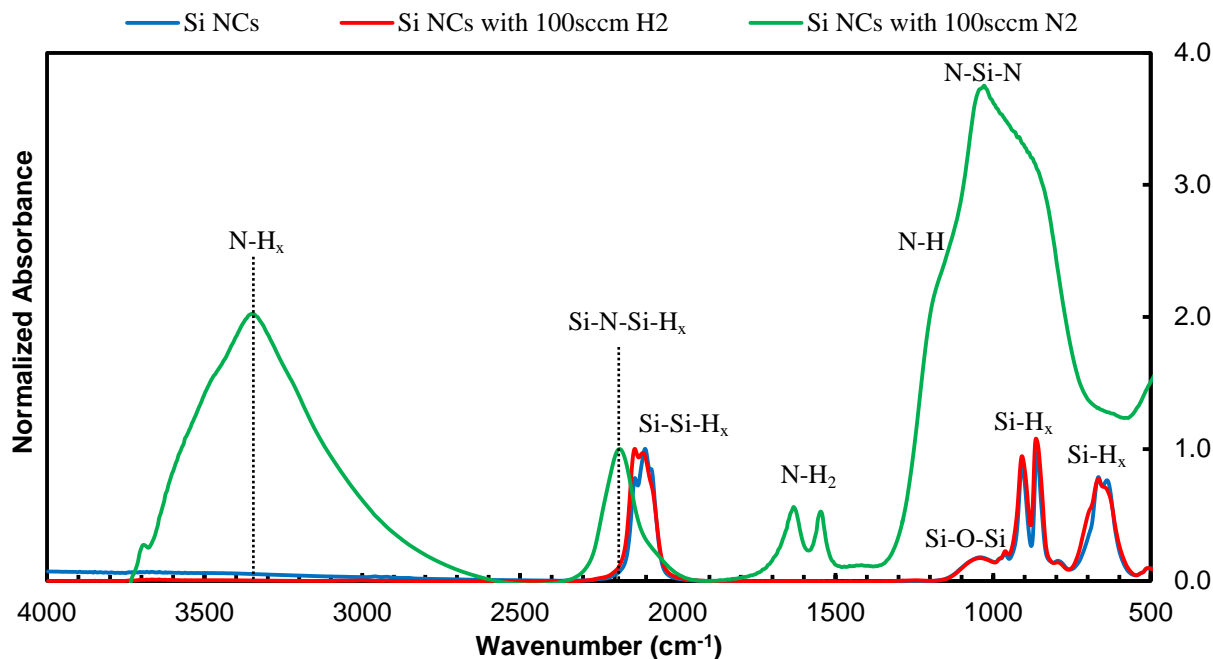


Figure 5.2: Comparison of FTIR spectra from Si nanoparticles (a) without any gas injection through the side arm, (b) 100 sccm H<sub>2</sub> through the side arm and (c) 100sccm N<sub>2</sub> through the side arm.

For Si NCs with N<sub>2</sub> injection, intense absorption band was observed in the range 700-1200 cm<sup>-1</sup> and is attributed to the transverse optical mode of Si-N-Si antisymmetric stretching vibration<sup>187,205–209</sup>. This peak position can change depending on the N<sub>2</sub> content of the film. There is a shoulder associated with the Si-N-Si broad peak centered at ~ 1150 cm<sup>-1</sup> and could be the combined effect of N-H bending vibration and the Si-N-Si longitudinal optical asymmetric stretch<sup>187,210–212</sup>. The presence of absorbance peak in the range 2000 – 2300 cm<sup>-1</sup> indicated the presence of H<sub>2</sub> at the sample surface as this peak could be assigned to Si-N-Si-H<sub>x</sub> (x = 1,2) stretching vibrations. But, there is a shift of ~ 86 cm<sup>-1</sup> for this peak towards higher wavenumbers as compared to SiH<sub>x</sub> peak from Si NCs without any gas injection and this happened as H atoms were replaced by N atoms in the surface Si back-bonds<sup>187</sup>. Hydrogen was also found to be bound with N atoms in Si NC surface and absorption bands at ~ 1550 cm<sup>-1</sup>, ~ 1635 cm<sup>-1</sup> represents NH<sub>2</sub> (secondary and primary) bending vibrations<sup>213</sup> whereas absorbance band at ~ 3356 cm<sup>-1</sup>

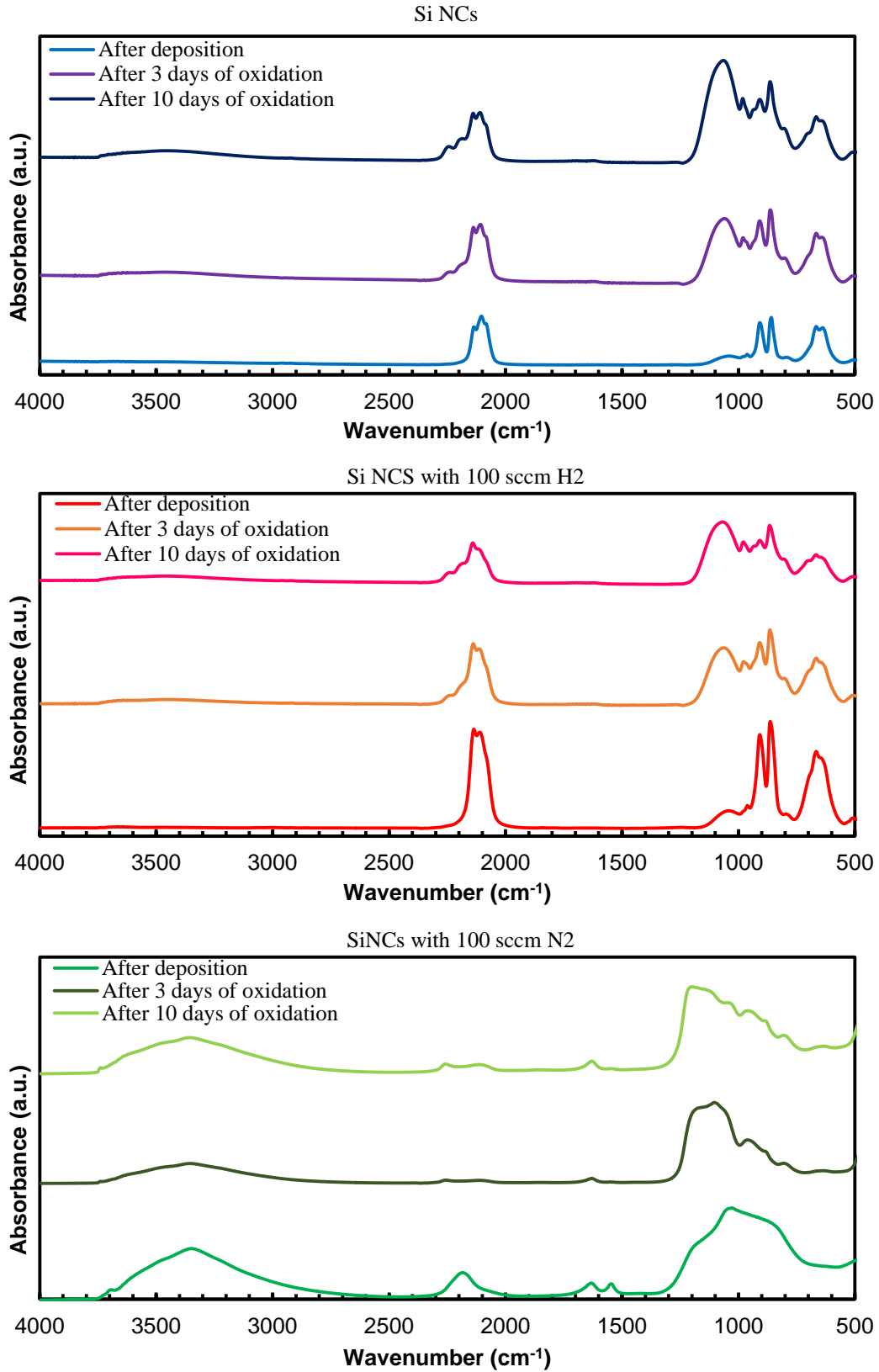


Figure 5.3: Evolution of FTIR spectra for three different cases.

represents  $\text{NH}_x$  ( $x = 1,2$ ) stretching vibrations<sup>213,214</sup>. The evolution of the samples discussed above is shown in Figure 5.3 using FTIR spectra. We have compared FTIR spectra from all the samples three times: just after deposition, after 3 days and after 10 days. The shoulder at  $\sim 1052 \text{ cm}^{-1}$  was due to partial surface oxidation of Si NCs and over the time it has increased indicating all the samples were oxidized.

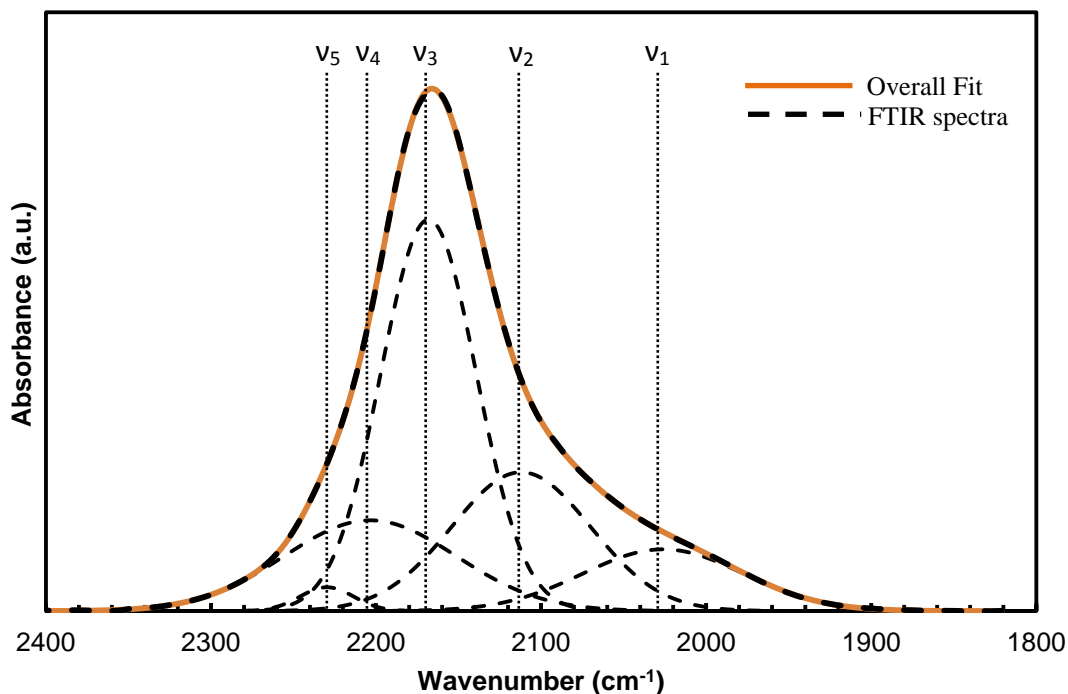


Figure 5.4: Deconvolution of the FTIR spectra for Si-N-Si-H<sub>x</sub> stretching vibrations region using five Gaussian lineshapes for Si NCs synthesized using 120 sccm N<sub>2</sub> flown through the side arm for the plasma reactor shown in Figure 4.1 (b).

To get a more detailed idea about the quality of nitride coating around Si NCs, we have carefully analyzed the Si-N-Si-H<sub>x</sub> ( $x = 1,2,3$ ) and Si-N-Si absorbance bands. Considering the information available in the literature<sup>187</sup>, we have deconvoluted the Si-N-Si-H<sub>x</sub> peak using five Gaussian lineshapes and is shown in Figure 5.4. The absorbance peak at  $\sim 2115 \text{ cm}^{-1}$  ( $v_2$ ) could be assigned to the binding configurations of  $(\text{Si}_2)\text{SiH}_2$  and  $(\text{Si}_2\text{N})\text{SiH}$ <sup>187,215,216</sup>. Whereas, the biggest absorption band centered at  $\sim 2170 \text{ cm}^{-1}$  ( $v_3$ ) can be attributed to the Si-H stretching vibration in

a  $\text{Si}_3\text{N}_4$  matrix whose actual configuration is  $\text{N}_3\text{Si:H}$ <sup>187,213</sup>. The absorbance bands at  $\sim 2030\text{ cm}^{-1}$  ( $\nu_1$ ) and at  $\sim 2205\text{ cm}^{-1}$  ( $\nu_4$ ) are unidentified. The smallest absorbance band at  $\sim 2230\text{ cm}^{-1}$  ( $\nu_5$ ) might be from SiH in the  $\text{N}_3\text{SiH}$  binding configuration<sup>187</sup>. Based on the Si-N bonding configurations, there exists four different types of Si-H bonding sites<sup>208</sup>. Si-H absorption band could shift from  $2090$  to  $2170\text{ cm}^{-1}$  when an N atom replaces an H atom. As we are not able to resolve these closely separated peaks due to  $(\text{N}_3)\text{Si-H}$ ,  $\text{SiN}_2\text{Si-H}$ , and  $\text{Si}_2\text{NSi-H}$ , we lumped all the absorption representing  $\text{N}_3\text{Si-H}$  vibration at  $2170\text{ cm}^{-1}$ .

The Si-N-Si antisymmetric stretching band from FTIR spectra (see Fig. 5.2) for  $\text{SiN}_x$  coated Si NCs synthesized with  $100\text{ sccm N}_2$  injected through the side arm into the  $\text{SiH}_4/\text{Ar}$  plasma is shown in Figure 5.5. This stretching band is broad in nature with center at  $\sim 1030\text{ cm}^{-1}$  and the position of this band can change based on the ratio of N and H content for a particular  $\text{SiN}_x$  film<sup>187,205-207,209</sup>. It is a known fact that for N-rich films, this absorbance band should appear beyond  $970\text{ cm}^{-1}$  towards higher wavenumber<sup>187,205</sup>. For our sample, the absorbance band appeared with center at  $\sim 1030\text{ cm}^{-1}$ , which is an indicative of synthesis of N-rich films. A similar trend was reported by S enemaud et al.<sup>217</sup>, who observed a shoulder in the Si-N-Si stretching band centered at  $\sim 1020\text{ cm}^{-1}$  for  $\text{SiN}_x$  films ( $1.27 < x < 1.61$ ) due to Si-N-Si stretching vibration in  $\text{N}_3\text{SiH}$ .

Additionally, a shoulder was also found in lower wavenumbers ( $\sim 830\text{ cm}^{-1}$ ) which is also an indicative of a more stoichiometric nitride film and can be assigned to the Si-N-Si antisymmetric stretching vibration<sup>209</sup>. A small shoulder of the absorbance band at  $\sim 1190\text{ cm}^{-1}$  could be attributed to N-H bending vibrations.

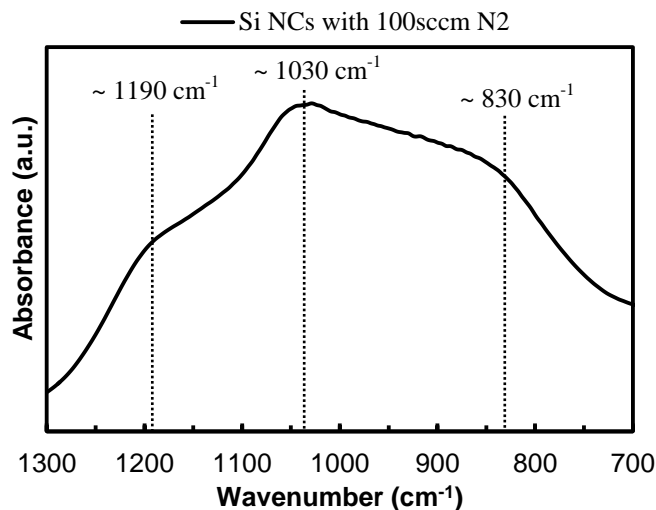


Figure 5.5: FTIR spectra showing Si–N–Si stretching band for SiN<sub>x</sub> coated Si NCs.

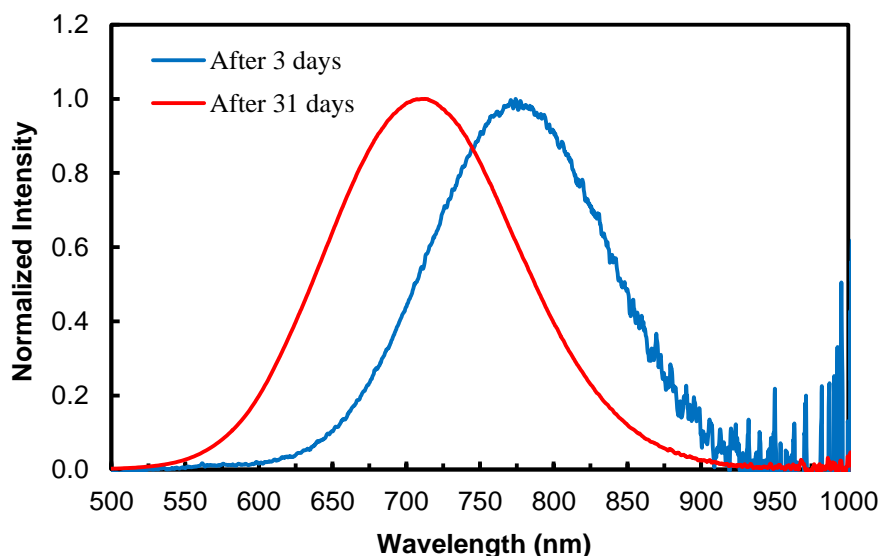


Figure 5.6: PL spectra from SiN<sub>x</sub> coated Si NCs synthesized with 100 sccm of N<sub>2</sub> through the sidearm into the SiH<sub>4</sub>/Ar plasma.

It is well-known that the deciding factors of PL from quantum confined (bohr radius  $\sim 5$  nm) Si NCs are nanocrystal size and its surface composition<sup>19,32,41,187,218,219</sup>. No PL was observed from these SiN<sub>x</sub> coated Si NCs immediately after the deposition within the sensitivity of our setup, and we had aged the samples in air approximately 3 days. So, the samples could have had nontrivial surface defect density and storing them in ambient-air environment helped them in capping their

defects and enhanced the sample's PL intensity. We have compared the PL spectra of SiN<sub>x</sub> coated Si NCs synthesized with 100sccm N<sub>2</sub> for two instances: 3 days after deposition and 31 days after deposition. The sample was exposed to open air after deposition and the evolution of its PL spectra is shown in Figure 5.6. The PL peak was at ~ 776 nm after 3 days and was blue-shifted a bit compared to Si NCs synthesized with 50 sccm of N<sub>2</sub> ( PL peak centered at ~ 780 nm but not shown here).

We have used the model developed by Ledoux et al.<sup>19</sup> for the calculation of nanocrystal core size and was found out to be ~ 4.4 nm (PL peak ~ 776 nm). We have studied two different flow rates of N<sub>2</sub> : 50 sccm and 100 sccm, but the PL spectra from both the cases were almost similar indicating self-limiting characteristics of our nitridation process<sup>187</sup>. Simulations performed by Kramer et al.<sup>56</sup> gave us an idea about the temperature fluctuations in Si NCs and from that study we know that the temperature of 5 nm Si NCs should be in the range of ~ 375<sup>0</sup>C – 575<sup>0</sup>C at 40W input rf power, the least power required for nanoparticle crystallization. Now, our PL results, which we measured 3 days after deposition, indicated the Si NC core size of ~ 4.4 nm in diameter. Considering the fact that the overall NC core size shrinks due to oxidation even though the NC becomes bigger as a whole<sup>187</sup>, we assume 4.4 nm was the minimum size of our Si NCs when it interacted with the N species inside the plasma. Based on this consideration, we are predicting the NC surface temperature to be close to 500<sup>0</sup>C, which is good enough to get structured nitride layer<sup>202</sup>. But, the nitride layer might not be thick enough and therefore susceptible to oxidation as can be seen from the PL spectra.

The stability of our nitride coating with respect to atmospheric conditions was studied using PL spectra. With increasing number of days of exposure, (i.e. with increasing surface oxidation), emission from NCs blue-shifts (see Fig. 5.6) which is in good agreement with

theoretical analysis. Another plot showing the oxidation rate comparison of five different samples, are shown in Figure 5.7.

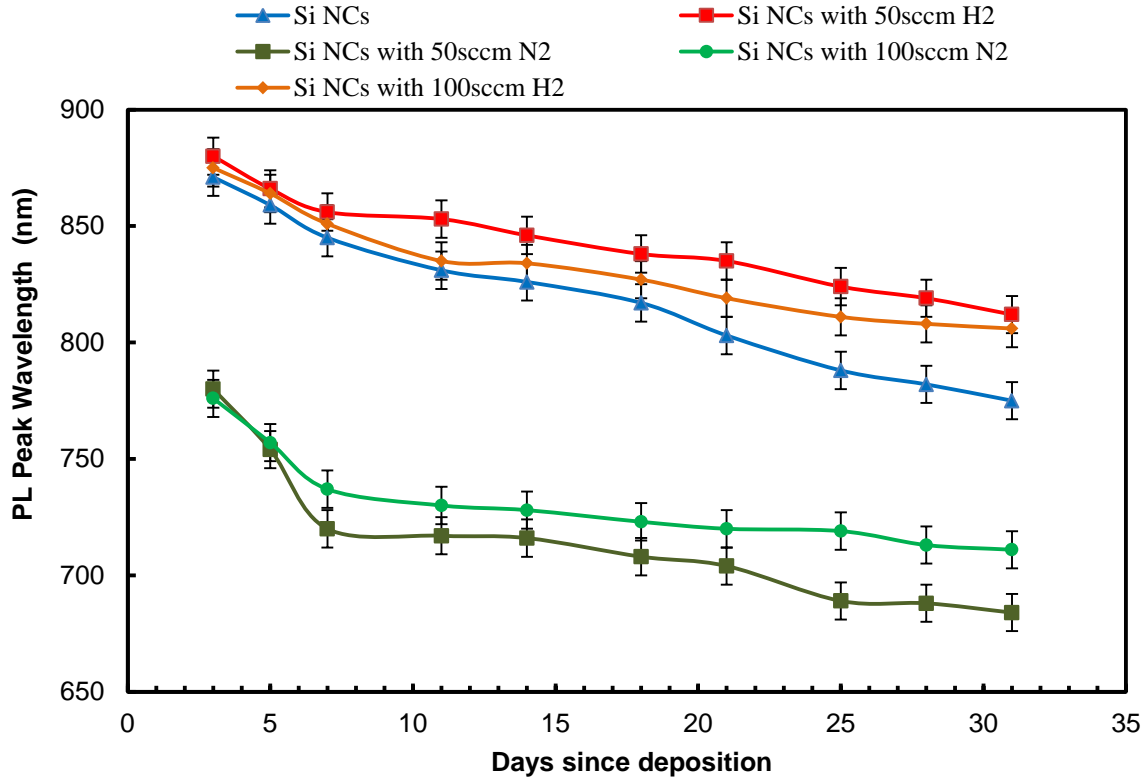


Figure 5.7: Evolution of PL peaks for different samples

Here, we have compared five different cases: Si NCs without any additional gas injection, SiNCs with H<sub>2</sub> injection (two different flow rates) and SiNCs with N<sub>2</sub> gas injection (two different flow rates). Data has been recorded for a month and during that period all the samples were stored in atmospheric conditions. Both the nitride samples exhibited a more rapid blueshift as compared to other three samples for first few days, but then stayed almost flat. From the plot, we found out that SiNCs synthesized with 100 sccm N<sub>2</sub> was the sample with least oxidation and more stable amongst all.

The NC diameter was also calculated after oxidation of 31 days using the same model introduced by Ledoux et al<sup>19</sup> based on the emission peak position and is estimated to be ~ 3.8 nm. So, after 31 days of oxidation, there was ~ 0.6 nm decrease in NC diameter, indicating that part of the SiN<sub>x</sub> layer was converted into a SiO<sub>x</sub>N<sub>y</sub> layer. For the complete prevention of oxidation and to keep the properties of the core intact, one must achieve the critical thickness of nitride layer<sup>220–222</sup>. It is also reported in the literature that only an ordered Si<sub>3</sub>N<sub>4</sub> coating suppressed oxidation under atmospheric conditions<sup>220</sup>. Thus, we surmise that the above mentioned nitride layer is less than the critical thickness to completely suppress the oxidation.

In order to get an idea about the nitride film quality and any possible surface contamination or impurities, XPS measurements were performed. Figure 5.8 shows a comparison of SiNC surface synthesized with and without N<sub>2</sub>. SiN<sub>x</sub> coated SiNCs were synthesized by flowing 120 sccm of N<sub>2</sub> through the sidearm into the SiH<sub>4</sub>/Ar plasma with reactor design shown in Figure 5.1(b). Figure 5.8 (b) and (d) with binding energy ranging from 392 – 412 eV shows the N(1s) spectra whereas Si(2p) spectra from 92 – 112 eV are displayed in Figure 5.8 (a) and (c).

The Si 2p spectra clearly indicate the presence of the Si NCs (~ 99.5 eV), as well as a Si–N feature (~ 101.9 eV)<sup>220</sup>. We can get an idea about how many N atoms are bound to Si atoms from the shifting of Si 2p peak position and based on the literature, the values are 2.7, 1.5, 0.8 and 0.3 eV for four, three, two and one N atom respectively<sup>199,223</sup>. Thus, we can assume that for our film Si atom is bound to four N atoms based on a shift of 2.4 eV. For stoichiometric Si<sub>3</sub>N<sub>4</sub>, each Si atoms is bound to four N atoms and they are arranged in a tetrahedron arrangement<sup>223</sup>. For intermediate nitrides of Si, one, two or three N atoms are replaced by Si atoms. The associated N 1s region also confirms the formation of a nitride at the surface with a binding

energy at  $\sim 397.8$  eV<sup>224</sup>. This binding energy is close to the measured value for Si $\equiv$ N bonds in Si<sub>3</sub>N<sub>4</sub><sup>202</sup>. The atomic ratio of Si and N for this nitride film was calculated from the XPS analysis and was found to be 1:1.22, which is very close to the stoichiometric ratio of 1:1.33. Si 2*p* peak at 99.5 eV is not included in this estimation. This difference between these two ratios is likely due to the presence of some nonstoichiometric nitride species<sup>199</sup>. We still see the Si 2*p* peak, meaning either the nitride is thin enough for the XPS to penetrate to the core, or that some surface atoms are unaffected by our process.

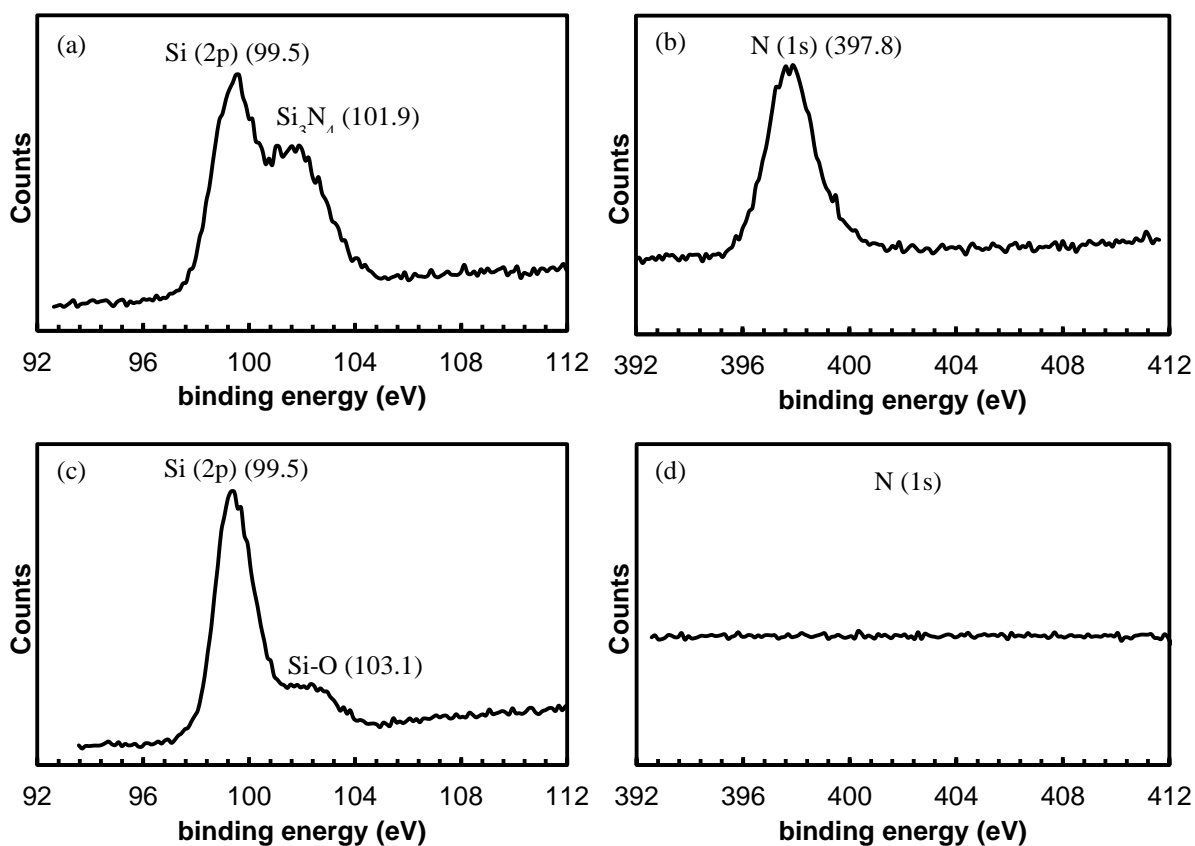


Figure 5.8: XPS measurements of (a) & (b) SiNCs synthesized with 120 sccm of N<sub>2</sub>, (c) & (d) SiNCs without any additional gas injection.

For SiNCs without any additional gas injection, with Si 2*p* peak ( $\sim 99.5$  eV), there was a shoulder at  $\sim 103.1$  eV which can be attributed to silicon oxide<sup>225</sup> ( see Fig. 5.8 (c) & (d)). The

XPS spectra was taken at the film surface and the measured oxygen impurity was due to the surface oxidation as the sample was exposed to air while transferring from the reactor to XPS instrument. Probable bonding configurations for our  $\text{SiN}_x$  film could be represented by the Figure 5.9<sup>207</sup>.

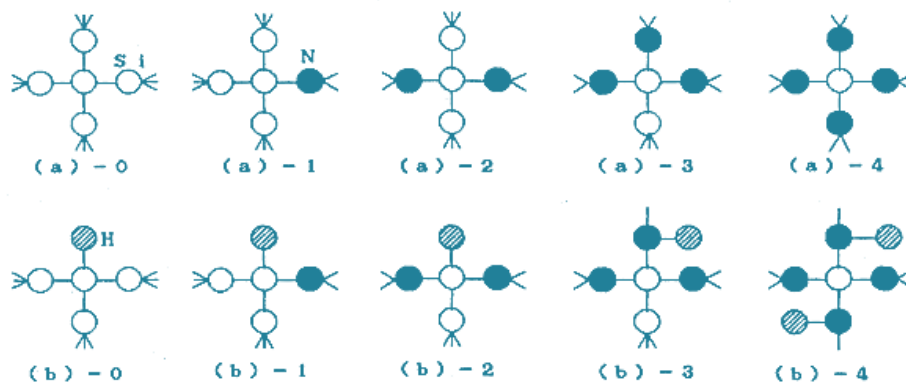


Figure 5.9: Schematic showing possible bonding configurations near a Si-N bond. (a) without hydrogen ( $\text{SiN}_x$  group), and (b) with SiH and NH bonds ( $\text{SiN}_x$  (H) group). (Adapted from Hasegawa et al.<sup>207</sup>)

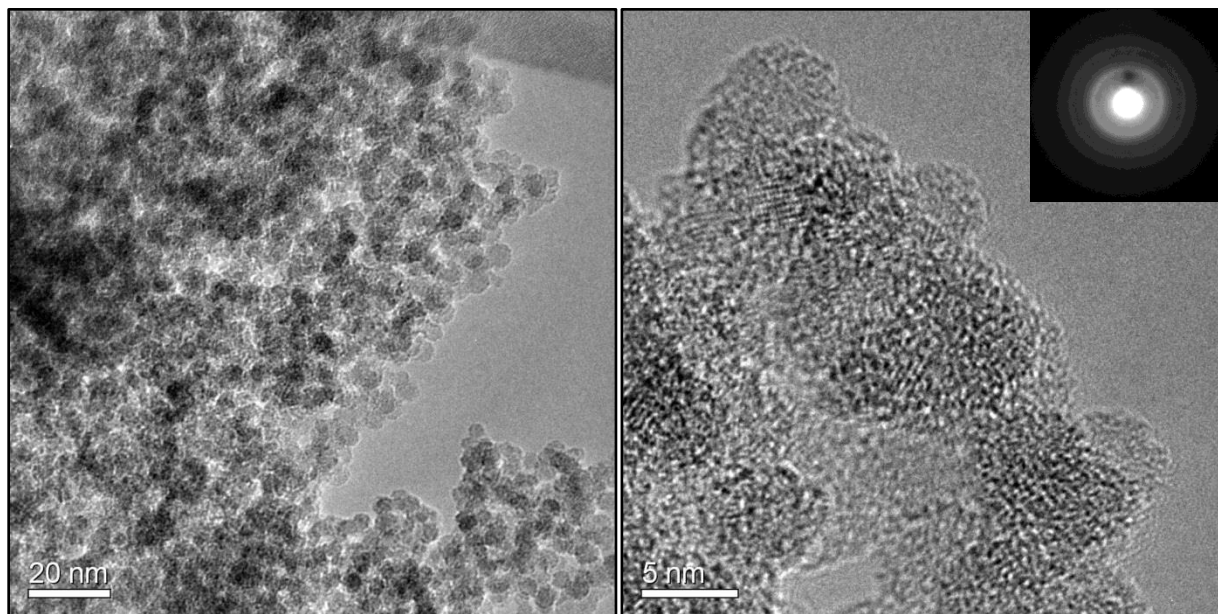


Figure 5.10: TEM images of  $\text{SiN}_x$  coated SiNCs synthesized with 120 sccm  $\text{N}_2$  using reactor design shown in Figure 5.1(b). The inset shows the SAED pattern.

TEM and SAED analysis were performed using a JEOL 2200 FS ultra-high resolution microscope. Bright-field TEM images are shown in Figure 5.10 alongwith SAED pattern. These TEM images confirmed the formation of Si NCs in the nitride film and the corresponding SAED pattern showed the silicon (111), (220), and (311) diffraction rings, consistent with other results.

The formations of defect states at the passivation layer or at the interface can be examined by electron paramagnetic resonance (EPR) spectroscopy given the defects are paramagnetic. This condition is mainly applicable for silicon dangling bonds present at the SiN<sub>x</sub> surfaces<sup>226</sup>. As discussed earlier, EPR technique works under the principle of free electron energy level splitting in an given magnetic field and subsequent resonance under applied microwave frequency. Dangling bonds can be detected using this technique as they have a particular resonance at a given magnetic field and microwave frequency. The governing equation for resonance can be written as<sup>49</sup>:

$$\Delta E = h\nu = g \times \mu_B \times B$$

where  $\Delta E$  represents energy splitting of the electrons based on its spin direction,  $h\nu$  stands for the microwave radiation energy;  $\mu_B$  indicates the Bohr magnetron, applied magnetic field is represented by  $B$  and the  $g$  is a dangling bond specific value.

The EPR spectra from our samples are shown in Figure 5.11 and the magnetic field used for these two cases were different: 9862.382 MHz and 9815.484 MHz for SiNCs and SiN<sub>x</sub> coated SiNCs respectively. But, the  $g$ -value for both the cases is very close. It is known that the defects related to disorder in silicon is represented by D-defect with a corresponding  $g$ -value of 2.0052<sup>57,227</sup>. Whereas the defects found at the interfaces of Si-SiO<sub>2</sub> is known as P<sub>b</sub> defects and

has two g-values: 2.0019 and 2.0086 for parallel and anti-parallel cases respectively<sup>57,227</sup>. Si and N dangling bonds can also be found in N-rich SiN<sub>x</sub> thin films<sup>228</sup>. In contrast to Si dangling bond, N dangling bond is metastable and were only observed at extreme conditions<sup>228</sup>. The defects that we found for our sample was mainly P<sub>b</sub>-defects: for SiNCs with g = 2.0076 correlates to P<sub>b1</sub> (100), whereas, g = 2.0081 represents P<sub>b</sub> (110) for SiN<sub>x</sub> coated SiNCs.

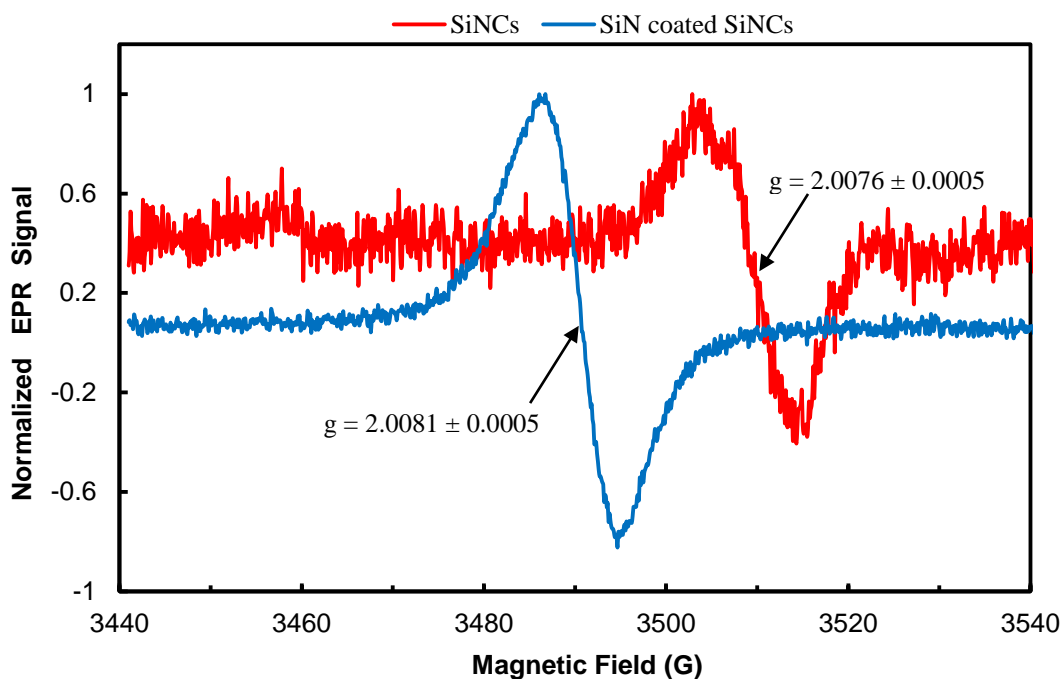


Figure 5.11: Comparison of EPR signals from SiNCs with SiN<sub>x</sub> coated SiNCs. (Note: the signals were acquired under different microwave frequency, accounting for the large offset in magnetic field.)

#### 5.4 Dual Plasma Synthesis

As discussed in the previous chapter, similar dual plasma system has been designed for the synthesis of SiNCs with a goal to grow a silicon nitride (SiN<sub>x</sub>) shell around those NCs. Main purposes of using dual plasma system was to take advantage of heterogeneous nucleation (growth of SiN<sub>x</sub> on SiNCs) and to have control on the crystallinity of nanoparticles and its surface properties. Two different reactor configurations have been used and the schematics are shown in Figure 5.12.

To grow a  $\text{SiN}_x$  shell around SiNCs, dual RF plasma setup was used with  $\text{N}_2$  flowing through the sidearm for both the cases as shown in Figure 5.12. For first case, both plasmas were in the main tube simultaneously, whereas, case 2 had primary plasma in the main tube and secondary plasma in the sidearm. The Primary plasma (Top) was used for the production of Si NCs and the secondary plasma (Bottom) for nitridation of those produced SiNCs.

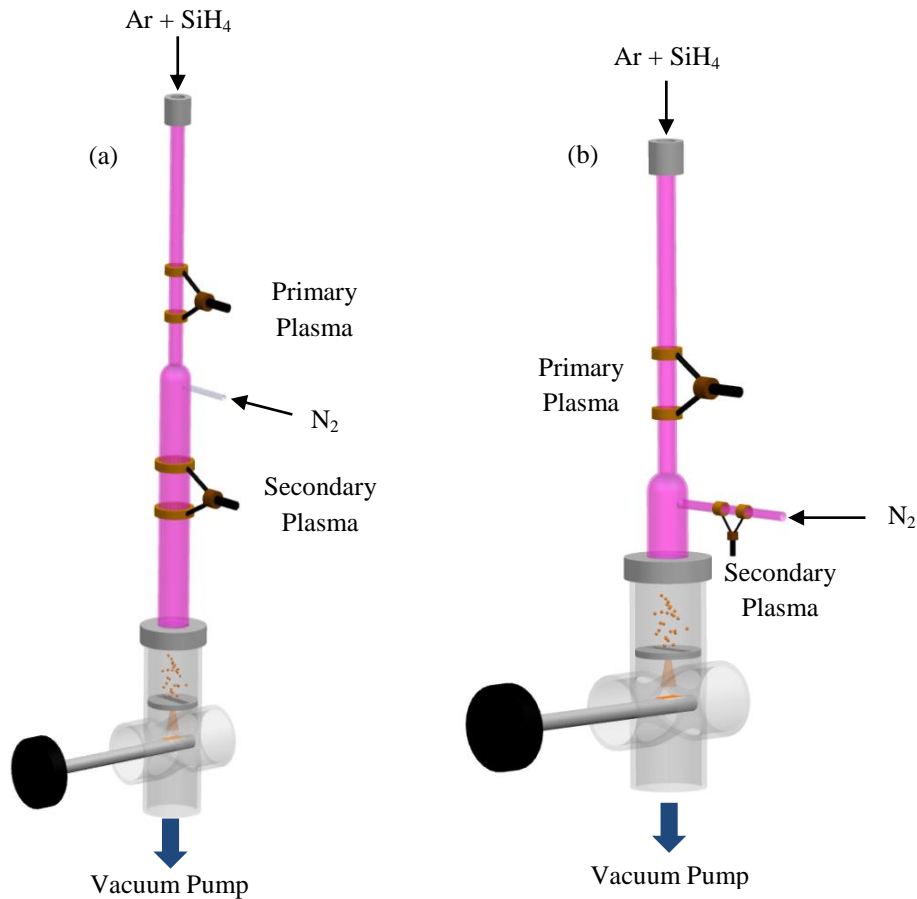


Figure 5.12: Schematics of the dual plasma reactor for (a) Case 1 and (b) Case 2.

The flow-through reactor consists of a pyrex tube with an outer diameter (O.D.) of 12.7 mm in the top portion and 25.4mm in the bottom portion. For case 1, the tube is 381 mm long and the expansion region is 177.8mm from the top. While for case 2, the tube is 304.8 mm long and the expansion region is also 177.8 mm from the top. Ar and SiH<sub>4</sub> (1% in Ar) are flown through the

pyrex tube (entered through the reaction zone with O.D. 12.7 mm, primary plasma) and a pair of ring copper electrodes is wrapped around that tube. The ring electrodes are positioned in such a way that the bottom edge of the ground electrode will be 5 cm and 2.54 cm above from the starting point of the expansion region for case 1 and case 2 respectively.

The thickness of the electrodes is around 1cm and the distance between the inside edges of the electrodes are 2.54 cm. The side arm has an O.D. of 6.35 cm and is located 2.5 cm below the junction point of the reaction zone and the expansion region. For case 1, side arm has 2.54 cm length, whereas, for case 2, it is 15.24 cm long. Another pair of electrodes with same thickness was used for the secondary plasma and the gap between the inside edges of the electrodes is 2.54 cm for case 1 and 4.2 cm for case 2. For case 1, the top electrode is located 3.8 cm below the sidearm, whereas, for case 2, the electrode closer to the main tube is located 5.1 cm away from it.

Two plasmas can be distinguished based on the emission color, where Ar/SiH<sub>4</sub> plasma looks purple, N<sub>2</sub> plasma is pink. Si NCs were nucleated, grew in Ar/SiH<sub>4</sub> plasma (primary) and were transported to the downstream region by the gas flow. The purpose of using secondary plasma was to provide enough energy for the dissociation of nitrogen atoms (N radicals) so that they can react and form bonds with silicon to create a shell of SiN<sub>x</sub> around SiNCs. N radicals for nitridation, which were produced by the secondary plasma, were irradiated to surface of Si NCs during their transportation to the downstream region. Case 1 was straightforward as both the plasmas were in the main tube. For case 2, we had to make sure that the N radicals coming out of secondary plasma should enter the main tube at the afterglow part of the primary plasma for the reaction to occur.

Ar and SiH<sub>4</sub> flow rate was fixed with 30 sccm and 80 sccm respectively, whereas N<sub>2</sub> flowrate was varied from 0 – 100 sccm. The pressure therefore, varied from 2.7 – 4.5 Torr. The supplied power was 25 W and 20W for primary and secondary plasma respectively. We performed a power study analysis to get this optimum power. For some experiments, we have flown 10 sccm SiH<sub>4</sub> along with N<sub>2</sub> through the sidearm in addition to flowing through the main tube. The purpose of using extra silane was to get better nitridation through more SiN<sub>x</sub> formation. The generated Si nanoparticles were collected on different substrates using impaction technique and then stored in air or in N<sub>2</sub> purged glove box depending on characterization requirement.

These synthesized NCs were characterized with FTIR, XPS, PL and EPR measurements. We started with comparing two different reactor configurations (case 1: straight tube dual plasma and case 2: side arm dual plasma). FTIR measurements were performed just after deposition to figure out the better nitridation amongst them and the results are shown in Figure 5.13.

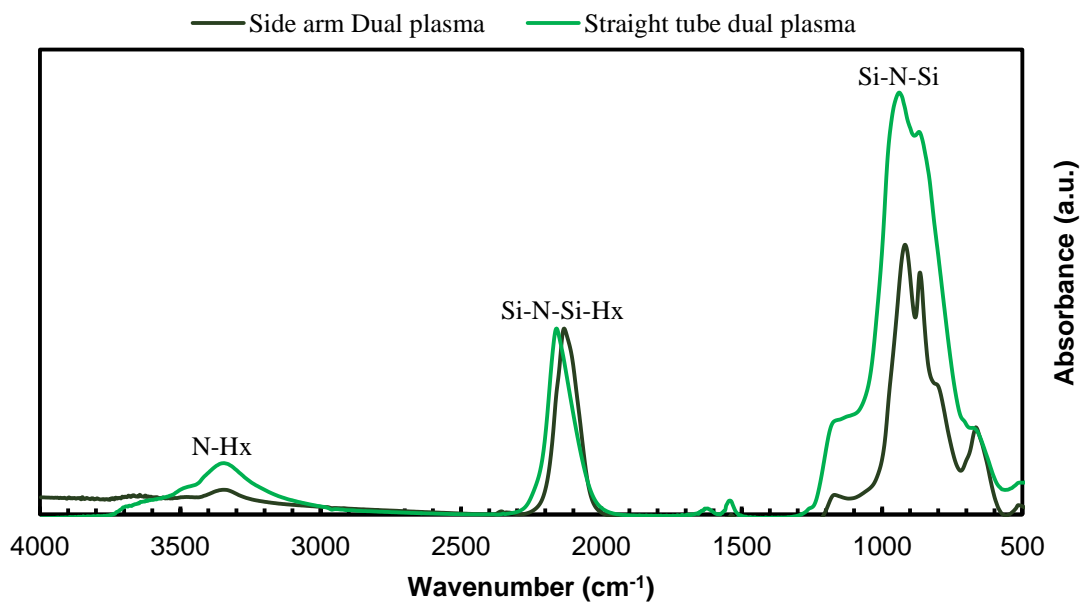


Figure 5.13: Comparison of FTIR spectra for two different reactor configurations

Samples were prepared with  $N_2 = 50$  sccm for both the cases with extra 10 sccm  $SiH_4$  for case 2. For both the cases, the Si–N–Si stretching band is prominent, broad and is centered at  $\sim 950\text{ cm}^{-1}$  and  $930\text{ cm}^{-1}$  for case 1 and case 2 respectively (see Fig. 5.13). Usually, absorbance features close to  $970\text{ cm}^{-1}$  is observed for N-rich films<sup>205</sup> and therefore straight tube dual plasma looks better in terms of nitridation. Also, there is a shift of Si–N–Si–H<sub>x</sub> peak towards higher wavenumber ( $\sim 30\text{ cm}^{-1}$ ) for the straight tube dual plasma compared to side arm dual plasma. Considering this result, we performed a parametric study on  $N_2$  flow rates for straight tube dual plasma. FTIR measurement for this study is shown in Figure 5.14. Three different flowrates were used: 25 sccm, 50 sccm, 100 sccm and out of these 25 sccm and 50 sccm sample looked promising in terms of nitridation. Both had the highest peak shift towards higher wavenumber for Si–N–Si–H<sub>x</sub> ( $\sim 60\text{ cm}^{-1}$ ) compared to plain SiNCs (no  $N_2$ ). Also, the Si–N–Si stretching band is found to be centered at  $962\text{ cm}^{-1}$  and  $950\text{ cm}^{-1}$  for 100 sccm and 50 sccm sample respectively indicating N-rich films. But, as 100 sccm  $N_2$  flowrate created instability in the secondary plasma, we opted for 50 sccm  $N_2$  flowrates.

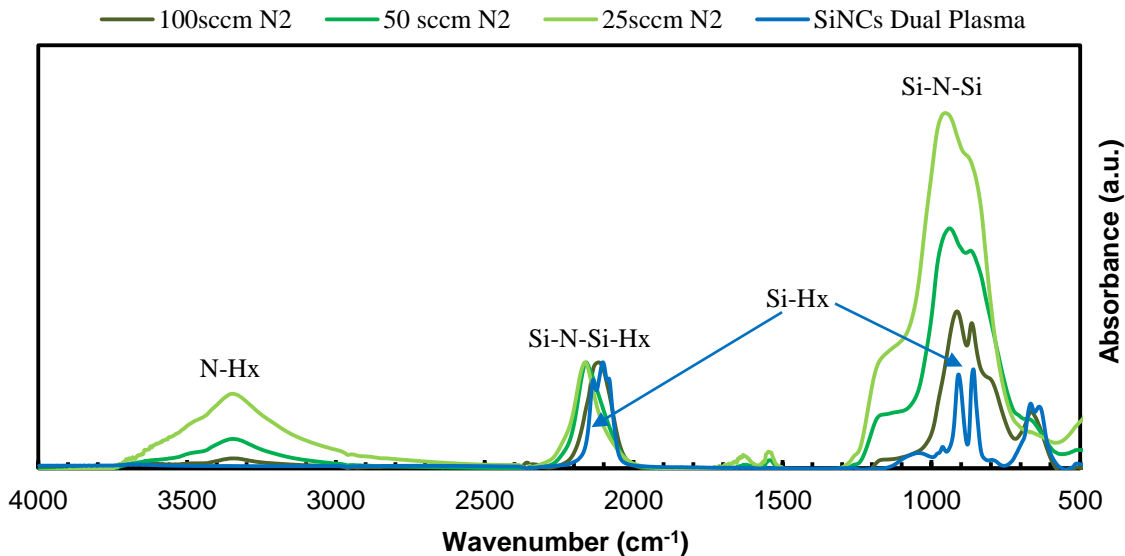


Figure 5.14: Comparison of FTIR spectra with different flow rates for case 1

To determine the qualities of our nitride films, we have performed the XPS measurement.

Figure 5.15 shows a comparison of nitride film synthesized from straight tube dual plasma with and without extra 10 sccm  $\text{SiH}_4$  flown through the side arm along with 50 sccm of  $\text{N}_2$ .

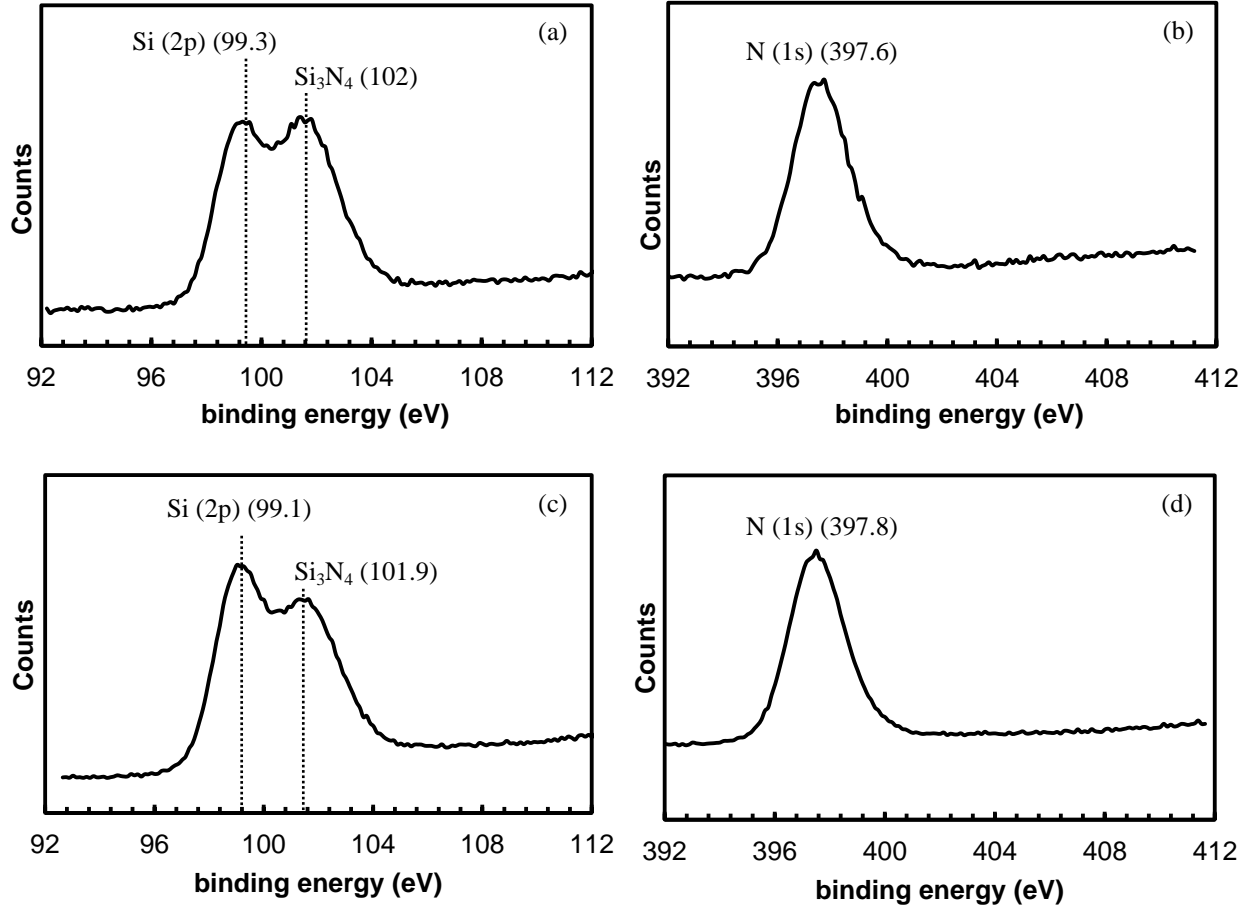


Figure 5.15: XPS measurements of  $\text{SiN}_x$  coated SiNCs from straight tube dual plasma (a) & (b) 50 sccm  $\text{N}_2$  through the side arm, (c) & (d) 50 sccm  $\text{N}_2$  with 10 sccm  $\text{SiH}_4$  through the side arm.

The Si 2p spectra clearly indicate the presence of SiNCs ( $\sim 99.3$  eV and  $\sim 99.1$  eV for two cases), along with a Si–N feature ( $\sim 102$  eV and  $\sim 101.9$  eV for two cases)<sup>220</sup>. Also, based on the shift of Si 2p peak ( $\sim 2.7$  eV and  $\sim 2.8$  eV respectively), we can assume that Si atom is bound to four N atoms<sup>199,223</sup>. N1s region also confirms the presence of a nitride at the surface<sup>224</sup>. The atomic ratios of Si and N for these two nitride films were calculated and were found out to be  $\sim$

1: 1.28 and ~ 1: 1.27 for without 10 sccm SiH<sub>4</sub> and with 10 sccm SiH<sub>4</sub> sample respectively (Si 2*p* peak was not considered for this calculation). These atomic ratios for both the cases has improved compared to single plasma nitridation process (see Fig. 5.8) and is closer to the stoichiometric ratio i.e. 1: 1.33<sup>199</sup>. As we can still see the Si 2*p* peak along with Si<sub>3</sub>N<sub>4</sub> peak, we can assume that either the nitride shell is very thin for XPS to penetrate or some surface Si atoms are still unaffected by this process. Comparing the Si 2*p* and Si<sub>3</sub>N<sub>4</sub> peak amplitude and atomic ratios of Si and N for both the cases, SiN<sub>x</sub> coated SiNCs without 10 sccm extra SiH<sub>4</sub> looks better in terms effective nitridation.

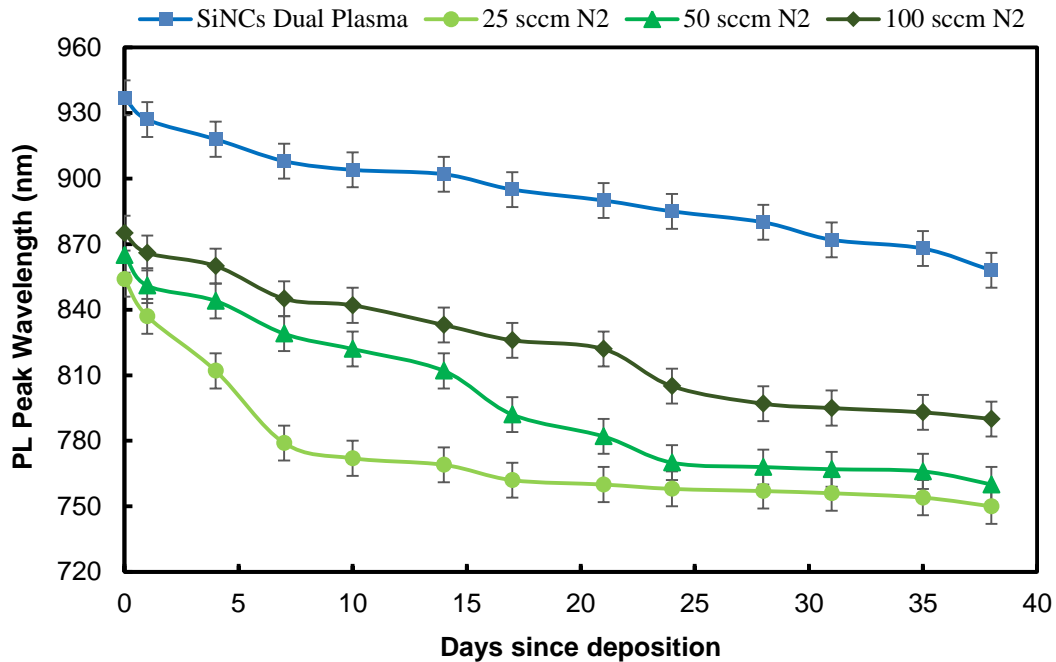


Figure 5.16: Evolution of PL peak for samples with varying N<sub>2</sub> flow rates

The stability of these SiN<sub>x</sub> coated SiNCs were studied using PL measurement. We have shown in Figure 5.16 how the PL peak evolves with days since deposition for the samples with different N<sub>2</sub> flowrates. We have recorded the data for 38 days since deposition and after analyzing, we found out that all the samples prepared with nitrogen were less blue shifted

compared to plain SiNCs from single plasma (without N<sub>2</sub>). 100 sccm N<sub>2</sub> sample looked better as compared to 50 sccm or 25 sccm sample in terms of total PL peak shift and could indicate better SiN<sub>x</sub> shell growth. To give a better idea about our nitridation process, we have measured the PL from samples produced with different reactor configurations and the data were recorded for 39 days. The results are shown in Figure 5.17.

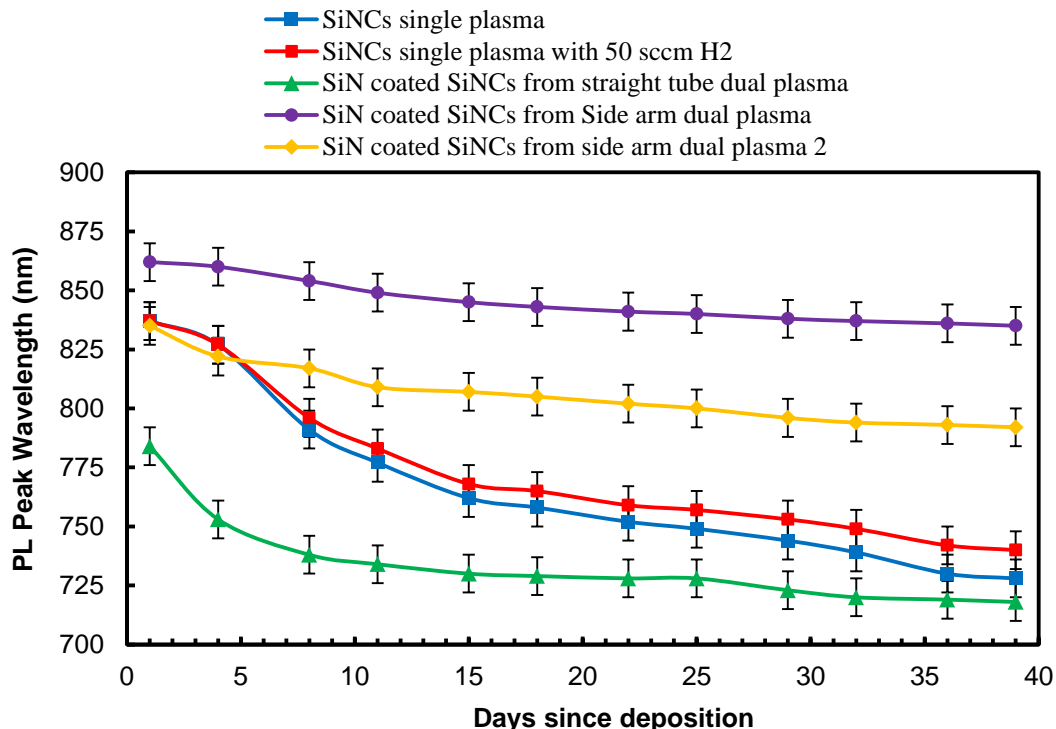


Figure 5.17: Evolution of PL peak for samples with different reactor configurations

Based on the data shown in Figure 5.17, we can surmise that SiNCs produced from the side arm dual plasma had least blue shifting in PL peak. But, based on the reactor configurations, we preferred the straight tube dual plasma as it had higher chances of creating better SiN<sub>x</sub> shell growth around SiNCs according to our hypothesis/understanding. Additionally, straight tube dual plasma was very close to side arm dual plasma in terms of PL peak shifting. To prove the effectiveness of our nitridation process and also to verify this data, we have performed EPR measurement.

Table 5.1: PL peak shifting data along with nanoparticle size for different samples

Sample Specification	PL Peak shift (nm)	Initial Nanoparticle Size (nm) <sup>19</sup>	Final Nanoparticle Size (nm) <sup>19</sup>	Change in Size (nm)
SiNCs single plasma	109	5.128	3.94	1.188
SiNCs single plasma with 50sccm H2	97	5.128	4.06	1.068
SiN coated SiNCs from straight tube dual plasma	66	4.51	3.85	0.66
SiN coated SiNCs from side arm dual plasma	27	5.462	5.11	0.352
SiN coated SiNCs from side arm dual plasma 2	43	5.126	4.59	0.5360

We have performed EPR study using a Bruker ELEXSYS–II E580 EPR spectrometer. Three different samples were tested: SiN<sub>x</sub> coated SiNCs using straight tube dual plasma, SiN<sub>x</sub> coated SiNCs using side arm dual plasma, and SiNCs from single plasma without N<sub>2</sub>. Dual plasma samples were prepared using 30 sccm Ar, 80 sccm SiH<sub>4</sub>, 50 sccm N<sub>2</sub> along with extra 10 sccm SiH<sub>4</sub> through the side arm. Single plasma sample was prepared by using only 30 sccm Ar and 80 sccm SiH<sub>4</sub>. First phase of EPR study was performed just after deposition and the samples were kept air free until the measurement. After the first phase of measurement, all three samples were kept in open air condition for 7 days and then the second EPR measurement was performed. All the measurement was performed under room conditions. The EPR spectra are shown in Figure 5.18 and the corresponding g values of each sample were also displayed. All the EPR signals were normalized by their respective nanoparticle weight.

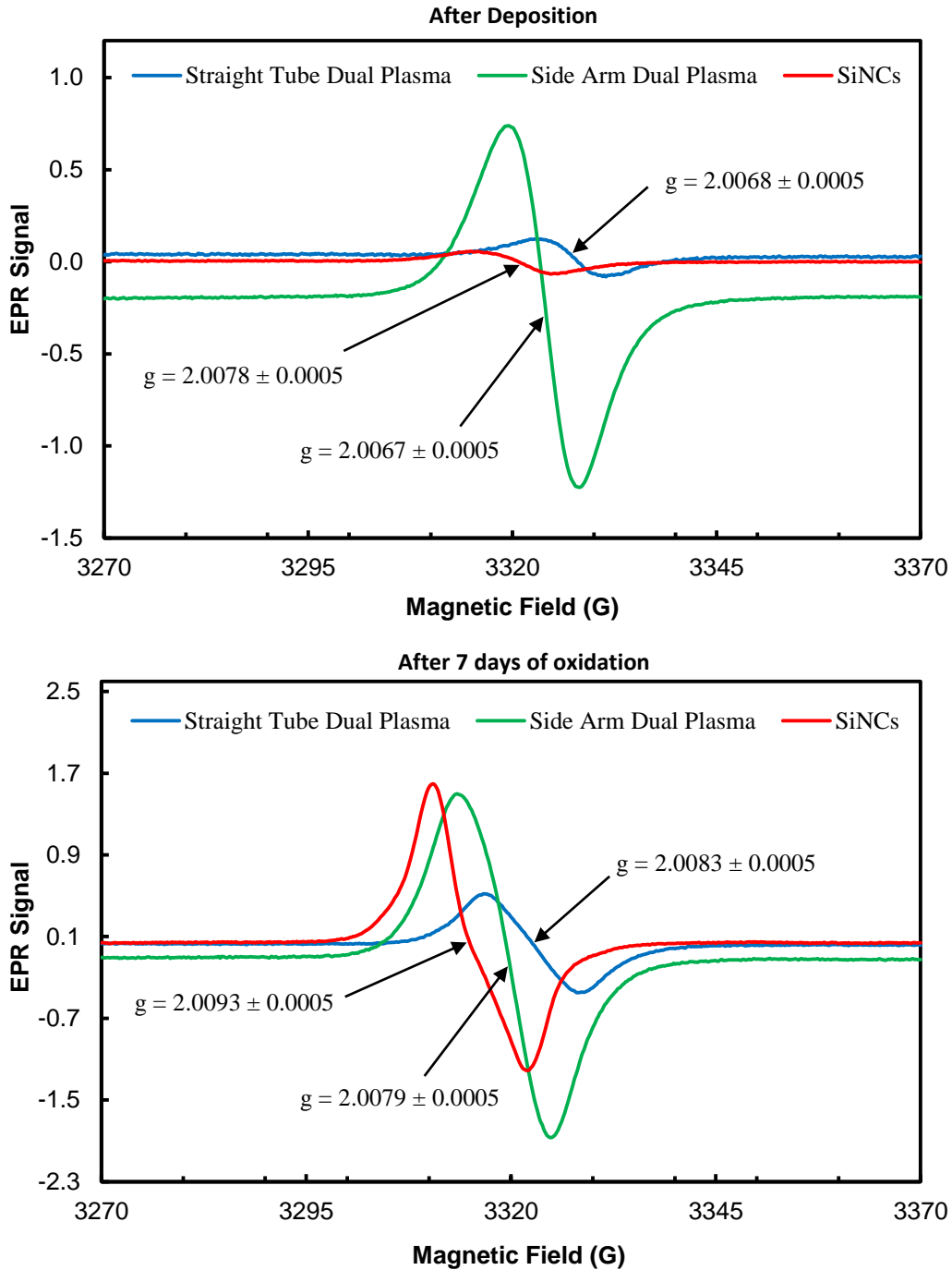


Figure 5.18: Comparison of EPR spectra for three different samples

Dangling bond defects or D-defects are very common in Si NCs and it represents disorder in a Si matrix and has a corresponding  $g$ -value of  $2.0053^{57,227}$ .  $P_b$  defect on the other hand has two  $g$ -values:  $2.0019$  and  $2.0086^{57,227}$ . Therefore, based on the  $g$ -values, we can surmise that both the

dual plasma sample had D-defects, whereas, the single plasma sample had  $P_b$  defects indicating the presence of  $SiO_2$ . In terms of EPR signals or amplitude, straight tube dual plasma sample and single plasma SiNCs had similar range of amplitude and is much lower than the side arm dual plasma sample indicating less defects content.

After 7 days of atmospheric exposure, all three samples' g-values verified that all the samples got oxidized. Also, the change in line shape for single plasma SiNC sample indicated that it was the most affected sample by oxidation. Comparing the EPR signals, we can say that the straight tube dual plasma had least oxidation, which in turn justifies our hypothesis that coating a  $SiN_x$  layer around SiNCs can prevent its oxidation and can make it more stable.

## 5.5 Conclusions

In this chapter, we have demonstrated surface nitridation of Si NCs in a single step process using non-thermal plasma. In an attempt to prevent the oxidation of Si NCs and to enhance its luminescence properties, we have successfully grown a shell of  $SiN_x$  around Si NCs. Two different plasma reactor configurations were tested: single plasma and dual plasma (primary plasma for the synthesis of Si NCs and secondary plasma for the growth of silicon nitride around Si NCs). With the help of a parametric study involving different reactor configurations, RF power, location of  $N_2$  injection, electrode positioning,  $N_2$  flowrate, we found out that maximum PL, better nitride shell growth and minimum oxidation occurs when these NCs are synthesized using a dual plasma process with  $N_2$  gas being injected in between two plasmas. These nanocrystals were characterized thoroughly using FTIR, XPS, TEM, PL measurement and found out to be oxidized when exposed to open air conditions thereby decreasing the SiNC core size (~ 1.2 nm decrease in NC core diameter for Si NCs over a period of 40 days, whereas, for  $SiN_x$

coated Si NCs, it was  $\sim 0.6$  nm over the same period). In order to prevent the oxidation, a critical thickness of  $\text{SiN}_x$  layer is to be achieved. We have discussed some on-going work in order to achieve this critical thickness. Upon successful synthesis, these NCs can be used in different applications like lithium-ion batteries, solar cells, LEDs etc.

## APPENDICES

# APPENDIX A

## Collaborative Projects

### **Part 1: Femtosecond Dephasing of Silicon Nanoparticles using a Total Internal Reflection**

**(TIR) Microscope:** This project is in collaboration with Prof. Marcos Dantus and his research group from the Department of Chemistry, MSU. Major portion of this project is done and is currently in progress for publication.

Nano-sized silicon has been one of the most interesting research topics after the discovery of its luminescence by Canham et al.<sup>155</sup>. Due to the “quasi-direct” electron-hole recombination process<sup>229</sup>, nano-sized silicon behaves like a direct band gap material, whereas bulk silicon is an indirect band gap material. The present study is about the dephasing of silicon nanoparticles (both oxidized and non-oxidized) and its coherence using a femtosecond laser, a pulse shaper, and a total internal reflection microscope (TIR)<sup>230</sup>.

We were responsible for preparing all the samples for this project. The dephasing analysis was done by Prof. Dantus’s Group, MSU. The silicon nanoparticles studied were synthesized in our lab using a flow-through plasma reactor in a fully gas-phase process<sup>50</sup>. Silane (1% in Argon) was used as a precursor gas and argon as a background gas. The flowrates were 80 sccm and 30 sccm respectively. The pressure was kept constant at 2.75 Torr using an orifice plate. The supplied power was 25W from a 13.56 MHz radiofrequency (rf) power supply via a matching network. The detailed description of Si NC synthesis was already discussed in Chapter 2. Three different types of Si NC films were studied in this case: Hydrogenated, Oxidized and surface functionalized Si NCs.

Hydrogenated films were synthesized by flowing 50 sccm of H<sub>2</sub> through the sidearm into the afterglow part of the plasma in addition to Ar and SiH<sub>4</sub> as discussed in the earlier chapters. These films were characterized just after the deposition and were kept air-free until the characterization. For oxidized sample, SiNCs were synthesized without any hydrogen injection and were left in open air for a week. For functionalized SiNC film, SiNCs were produced using the same recipe of hydrogenated samples. These SiNCs were then functionalized in a liquid-phase thermal hydrosilylation reaction<sup>77</sup> using 1-decene. Detailed functionalization procedure is already discussed in Chapter 2. PL QYs of the functionalized SiNCs was measured and found out to be ~ 50%, whereas for hydrogenated and oxidized Si NC film, it was ~ 2% and ~ 4% respectively.

The substrates used for this purpose was microscope glass cover slides. Before deposition, these glass slides were cleaned thoroughly using spectrometric grade methanol. For hydrogenated and oxidized samples, SiNCs were directly deposited from gas-phase onto glass slides using impaction techniques. The deposition time was 30 sec for both cases. As surface functionalization involved liquid-phase, those functionalized SiNCs were drop-casted onto glass cover slides. After deposition, all the cover slides were then covered with cleaned cover slides for image processing using microscope.

PL spectra were collected from all three Si NC films right after the deposition (Fig. A.1(a)). PL peak for both hydrogenated and oxidized sample were close, whereas functionalized SiNCs had PL peak blue shifted due to functionalization scheme. Absorption spectra were also collected and are shown in Figure A.1(b). The functionalized SiNC film demonstrated absorption of light below 600nm, beyond which there was little absorption. However, for hydrogenated and oxidized SiNC films, they absorbed light below 800nm.

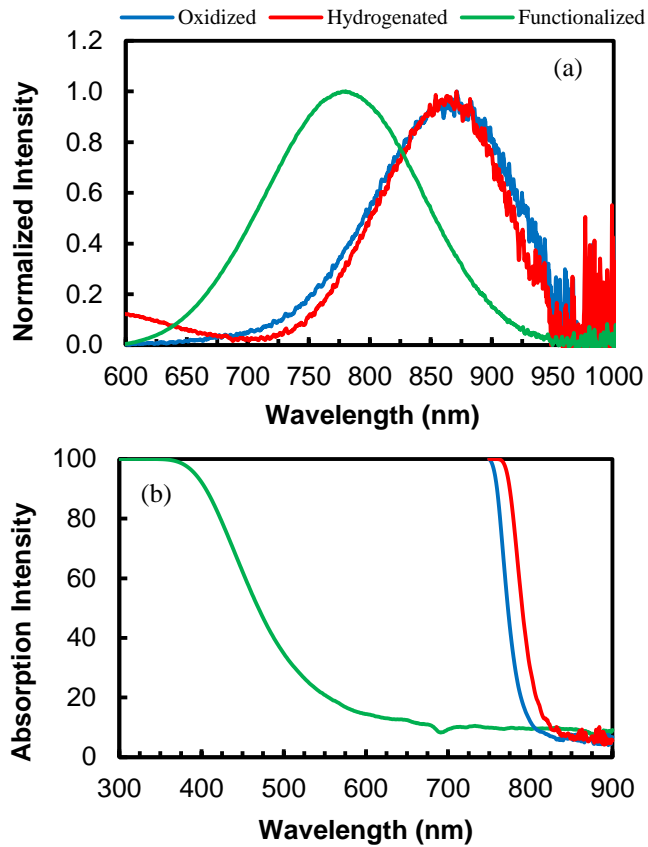


Figure A.1: (a) Photoluminescence spectra and (b) absorption spectra from three different types of SiNC films.

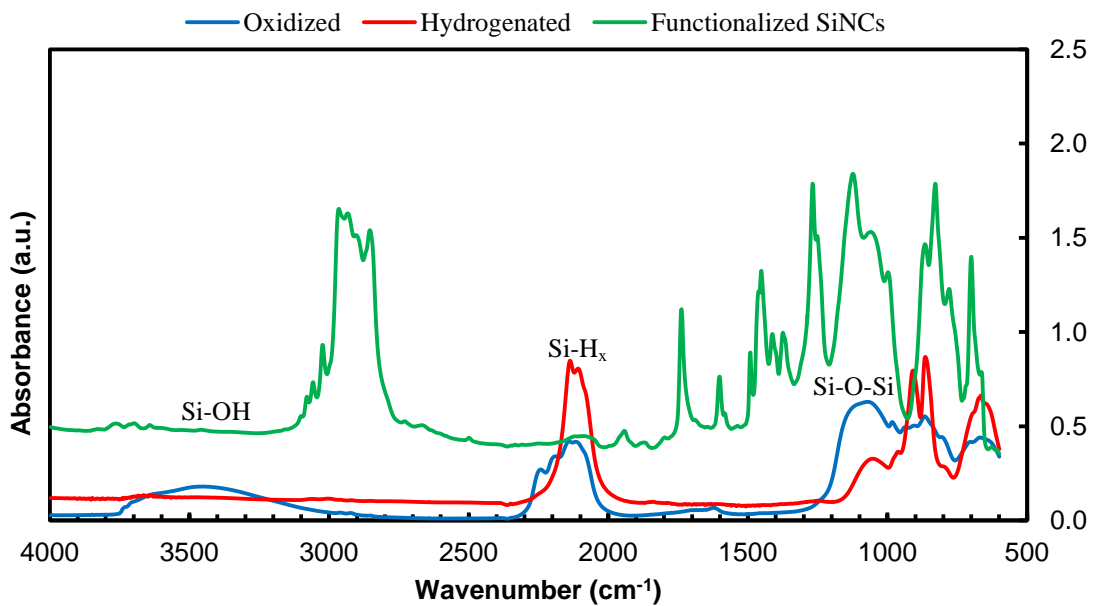


Figure A.2: FTIR spectra from three different types of Si NC films.

FTIR spectra from all the samples are displayed in Figure A.2. The oxidation peak is prominent for the oxidized sample at  $1050\text{ cm}^{-1}$  for the oxidized sample. However, for hydrogenated sample, there is a little shoulder of oxidation peak as the sample was exposed to open air while transferring the sample from the reactor to instrument. For functionalized SiNC film, there was no such oxidation peak as well as SiHx peak was almost gone as compared to non-functionalized Si NC film.

**Part 2: Fabrication of Photonic Crystal Structures by coupling Silicon Nanocrystals with Polymer Nanolattices:** This project is in collaboration with Prof. Julia R. Greer and her research group from the Department of Materials Science and Mechanics, California Institute of Technology. The project is currently in progress and hopefully would be ready for publication next year.

A photonic crystal can be defined as a periodically repeating structure made up of two distinct materials having different dielectric constants and was studied by several researchers to improve the LED efficiency<sup>231-233</sup>. This project can be divided into two parts: fabrication of polymer nanolattices and deposition of Si NCs on polymer nanolattices. Ryan Ng from Prof. Greer's Group is working on the fabrication of nanolattices along with device fabrication. We were responsible for the coupling of Si NCs with polymer nanolattices. They have used the Direct Laser Writing (DLW) Two-Photon Lithography (TPL) method as reported in Chernow et al<sup>234</sup> to fabricate polymer nanolattices. Three different structures of nanolattices have been considered for this project.

Octahedron is an open structure, simple cubic analogue and unit cell is of the order of microns. Whereas, octet has face-centered cubic (FCC) analogue and unit cell is of the order of

microns. In terms of photonic properties, woodpile structure is the best amongst all three structures and its unit cell is of the order of nm (scale of visible light). Having diamond cubic analogue, woodpile structure exhibits full photonic band gap. Although, it is very difficult to deposit onto the woodpile structure as the inter-beam spacing is very small. However, octahedron being the simplest structure is the best in terms of ease of fabrication/deposition. Therefore, octahedron structure is mostly used for this project.

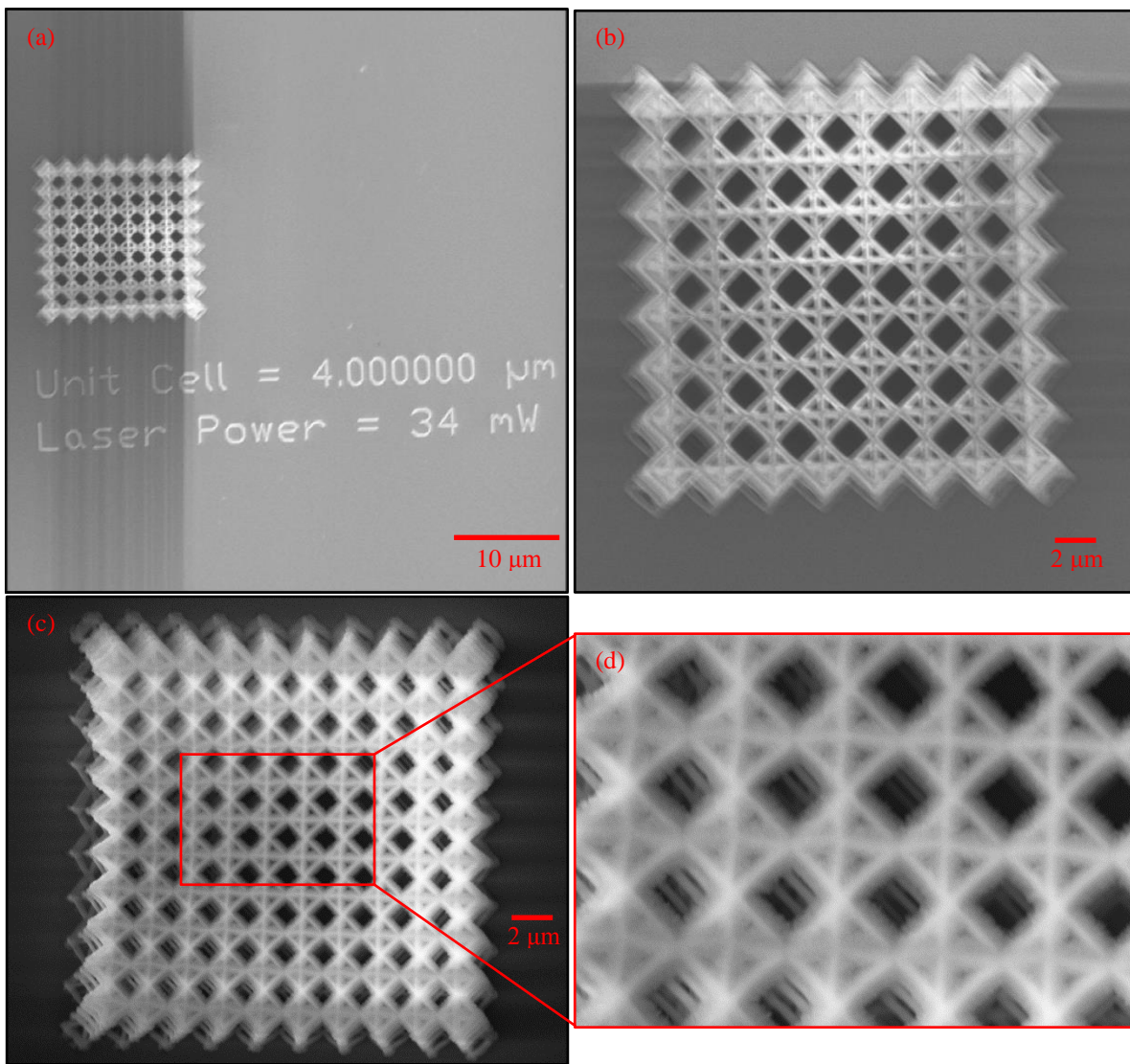


Figure A.3: SEM images of Octahedron Polymer Nanolattices on Si wafer: (a) and (b) before Si NC deposition, (c) and (d) after coated with Si NCs.

Characterization of these nanolattices was performed using SEM. SEM images of these polymer nanolattices are shown in Figure A.3. As explained in detail in Chapter 2, the deposition of Si NCs can be done in two ways: impaction and diffusion. When the gap between the orifice and substrate is comparatively high, it follows diffusion whereas, impaction of nanoparticle happens when the substrate is very close to the orifice. We have studied four different gap distances between the orifice and substrate: 3mm, 7.5mm, 12mm and 22mm. Then, we have performed SEM analysis of these samples having different gap distances. For the sample with gap of 3.5 mm, deposited layer came out to be really dense and thick. Being so close to the substrate, the deposition through orifice should follow impaction technique and won't be able to penetrate the nano trusses all the way to the bottom. We observed the same thing for this sample.

When the gap distance was really high, i.e. 22mm, it looked like there was almost no deposition at all. For the two intermediate gap distances, i.e. 7.5 mm and 10 mm, samples looked good both in terms of thickness and density. But, with 7.5 mm gap, penetration of SiNCs through the nano trusses were better (see Figure 7.3) and therefore, we have maintained the same gap for the rest of our study.

The possible contact fabrication (for Masking) technique to enable these nanolattices for photonic applications can be explained using the flow chart diagram as shown in Figure A.4. Out of these steps, only the deposition of Si NCs has been performed in our lab and rest of the steps are done by Ryan Ng from Prof. Greer's group.

This project is underway and involves a lot of future studies. We will mainly focus on octahedron nanolattices due to its ease of deposition but will eventually move towards woodpile structures. Also, we will try to explore band gap tunability effects.

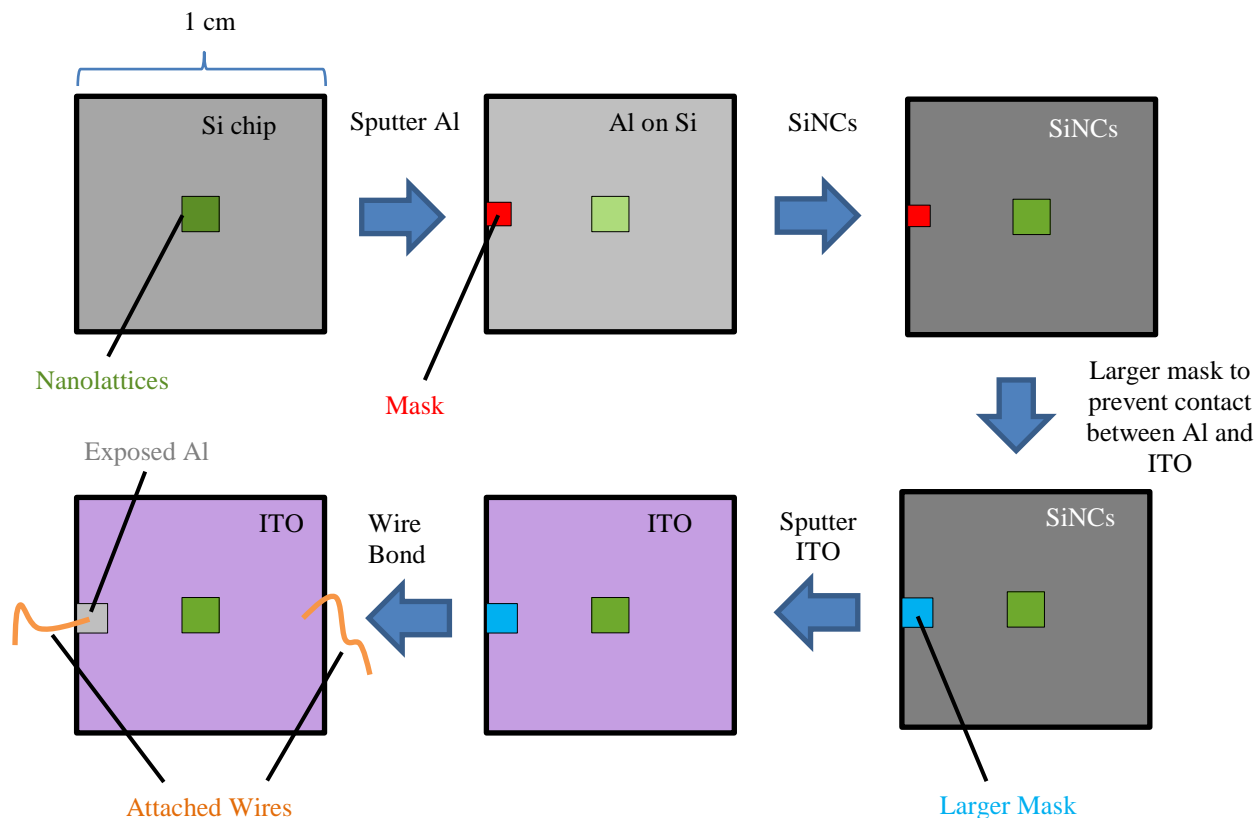


Figure A.4: Flow chart diagram showing different steps of Deposition and Masking. (Figure Credit: Ryan Ng, Caltech)

### Part 3: Liquid-Phase Surface Functionalization of Silicon Nanocrystals using different

**Ligands:** This project is in collaboration with Prof. Rémi Beaulac and his research group from the Department of Chemistry, MSU. The project is currently under progress and hopefully would be ready for publication next year.

The objective of this work is to enhance the luminescence from Si NCs and to get rid of defects (achieve better surface coverage) for application in LEDs. We have already discussed the liquid-phase surface passivation of Si NCs<sup>58,77</sup> using 1-decene in chapter 2. A lot of research has been done over the past decades on surface functionalization/termination of silicon surfaces using alkyl group (methyl, ethyl), chlorination and allyl group<sup>235-241</sup>. Besides 1-decene, Si NCs

were also functionalized with several other ligand groups, such as, amine group (10 carbon chain), methyl group and chlorine group. We were responsible for the synthesis of Si NCs and the functionalization part was performed in Prof. Beaulac's Lab. This study is about comparing the performances of several ligand groups in passivating Si NC surfaces.

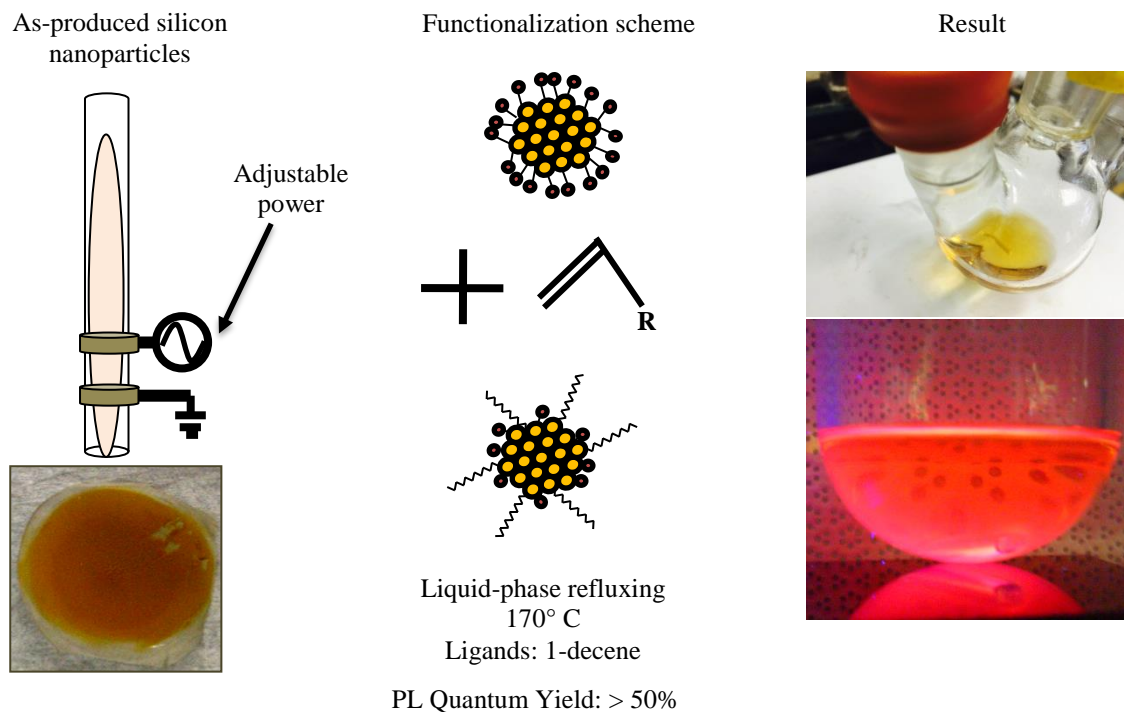


Figure A.5: Steps of surface functionalization of Si NCs with 1-decene<sup>49,58</sup>. (Figure Credit: Dr. Rebecca Anthony)

## APPENDIX B

### Plasma-induced Crystallization of Gallium Nitride (GaN) Nanoparticles

The heating mechanism behind the crystallization of silicon nanoparticles in a non-thermal plasma reactor has already been studied by Kramer et al.<sup>56</sup> Here, using the same model reported by Kramer et al.<sup>56</sup>, we have studied the effects of pressure, electron temperature, ion density and hydrogen density on GaN nanoparticle temperature eventually leading to its crystallization.

GaN nanoparticles were synthesized using a flow-through plasma reactor using argon-ammonia (NH<sub>3</sub>)-trimethylgallium (TMGa) gas mixture as discussed in detail in Chapter 4. Crystallization of these nanoparticles was verified using XRD, TEM and Raman spectroscopy. Ion density and electron temperature are the most important factors responsible for the heating and cooling mechanism for nanoparticle surface and hydrogen density should not be as important for GaN as it is for silicon nanoparticles. We have used the same transient particle energy balance<sup>55</sup> as it was used for Si NCs for the calculation of GaN nanoparticle temperature ( $T_p$ ),

$$\frac{4}{3}\pi r_p^3 \rho C \frac{dT_p}{dt} = G - L, \quad (\text{B. 1})$$

where,  $r_p$  is the particle radius,  $\rho$  represents the mass density of GaN and  $C$  is its specific heat,  $G$  and  $L$  represents the heating and cooling term respectively. We have assumed that the GaN nanoparticles and its bulk counterpart has the same mass density and specific heat and for the simplification of calculation we also assumed that the GaN nanoparticles were spherical<sup>55</sup> in shape. Electron-ion recombination process was mainly responsible for the heating of

nanoparticles and cooling happened due to the conduction heat transfer by Ar. We have used the Monte Carlo approach<sup>242</sup> and  $10^{-8}$  sec time step for this simulation. Initial conditions used were that the nanoparticle temperature was same as gas temperature and the nanoparticles were in neutral condition. The input parameters used in this case were calculated from theoretical analysis and might not be accurate. Due to experimental limitations, we couldn't perform the plasma diagnostics but we have a future plan of doing the same.

Nanoparticle characterization was performed with the help of TEM, XRD and Raman spectroscopy as discussed in detail in Chapter 4. The input parameters like electron temperature, ion density and hydrogen density were calculated (approx.) using the data from Kramer et al.<sup>56</sup> for the threshold plasma power required for crystallization of GaN nanoparticles in our case.

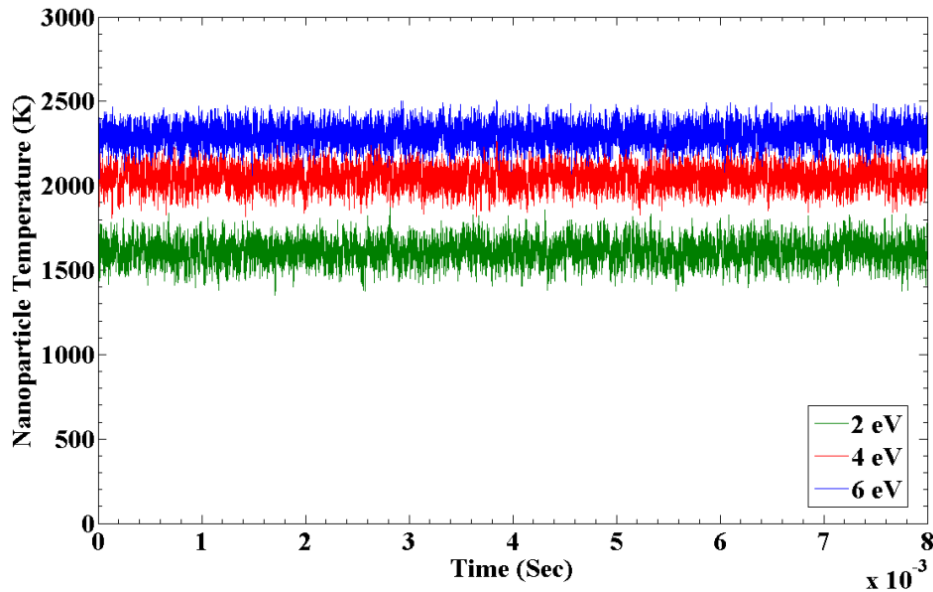


Figure B.1: Effect of electron temperature on nanoparticle temperature.

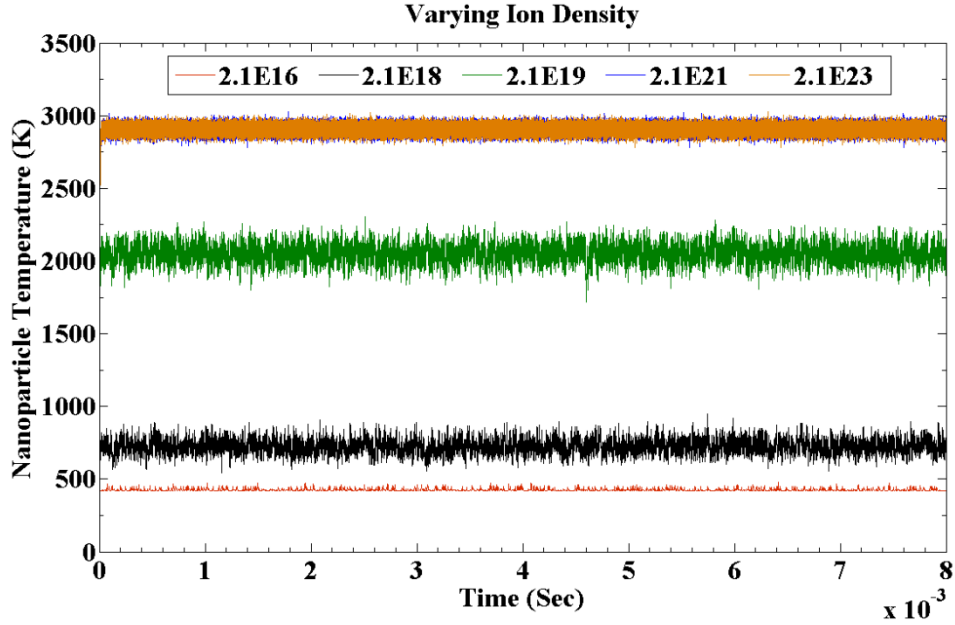


Figure B.2: Effect of ion density on nanoparticle temperature.

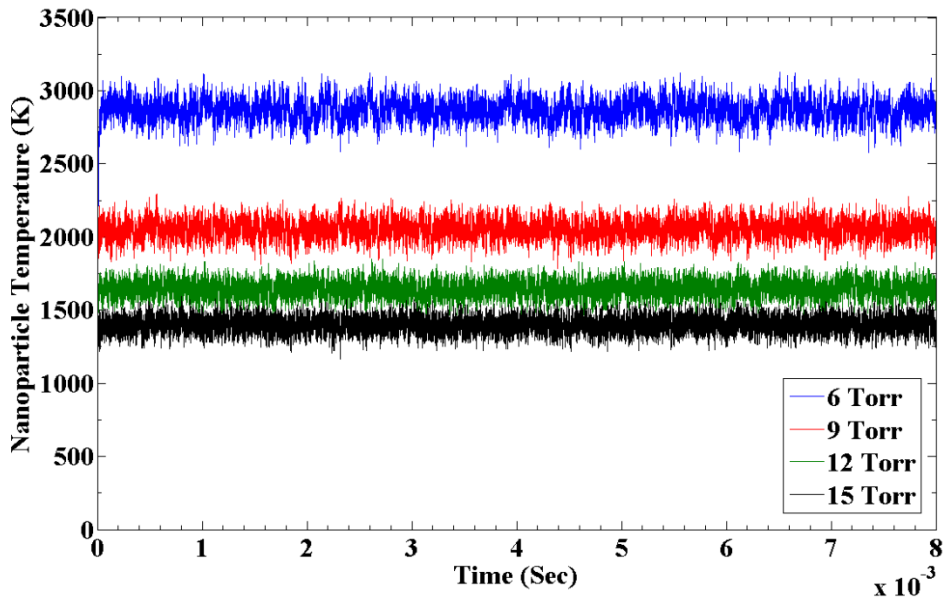


Figure B.3: Effect of reactor pressure on nanoparticle temperature.

Figure B.1–B.3 shows the effects of varying electron temperature, ion density, and pressure on nanoparticle temperature ( $T_p$ ). Initial gas temperature was assumed to be 420K, but the nanoparticles have reached much higher temperatures with increasing electron temperature, ion

density and reactor pressure. The electron temperature and ion density was 4 eV and  $2.1 \times 10^{19} \text{ m}^{-3}$  for most of our calculations and is very relevant for our plasma synthesis conditions. Reactor pressure is directly related to the total gas flowrate and it was 9 Torr for most of our calculations, although, it can be easily controlled by changing the gas flowrates and by keeping the same orifice plate. The effect of varying hydrogen density on the nanoparticle temperature is shown below (see Fig. B.4).

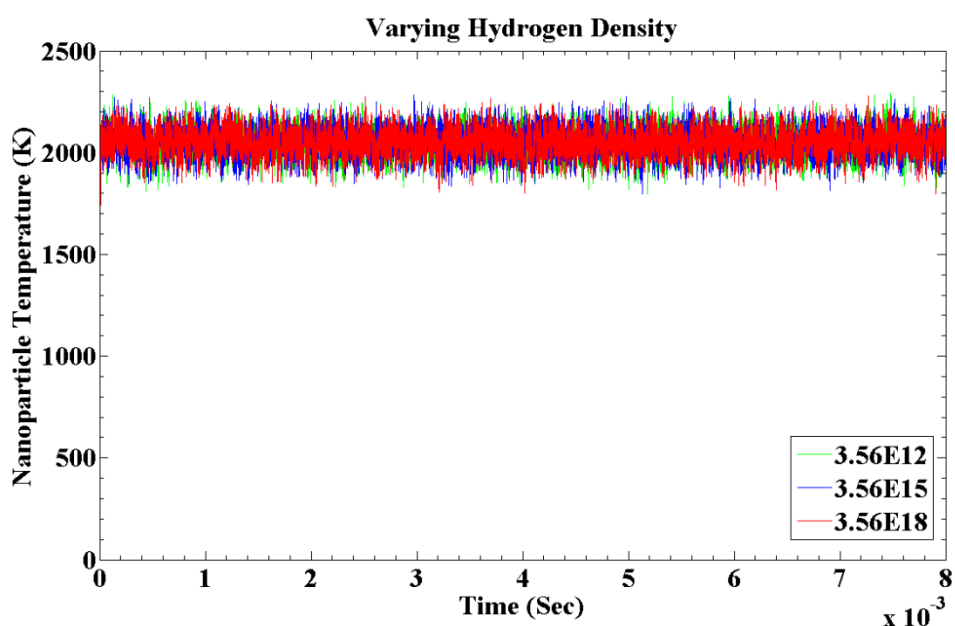


Figure B.4: Effect of hydrogen density on nanoparticle temperature.

The nanoparticle temperature did not seem to change much with varying hydrogen density, but with increasing hydrogen density, occurrence of number of events (temperature fluctuations) has increased. Ion density used for this case was  $2.1 \times 10^{19} \text{ m}^{-3}$ . Although, to get a better idea about the impact of hydrogen density on the nanoparticle temperature, we have calculated the nanoparticle temperature with and without hydrogen density at a fixed ion density (see Fig. B.5). Similar trend was observed and the nanoparticle temperature did not change after adding hydrogen density for a fixed ion density. Addition of hydrogen atoms has only increased the

temperature fluctuations. The nanoparticle temperature calculated based on our plasma reactor conditions was as high as 2200 K, which is sufficient for crystallization of GaN nanoparticles.

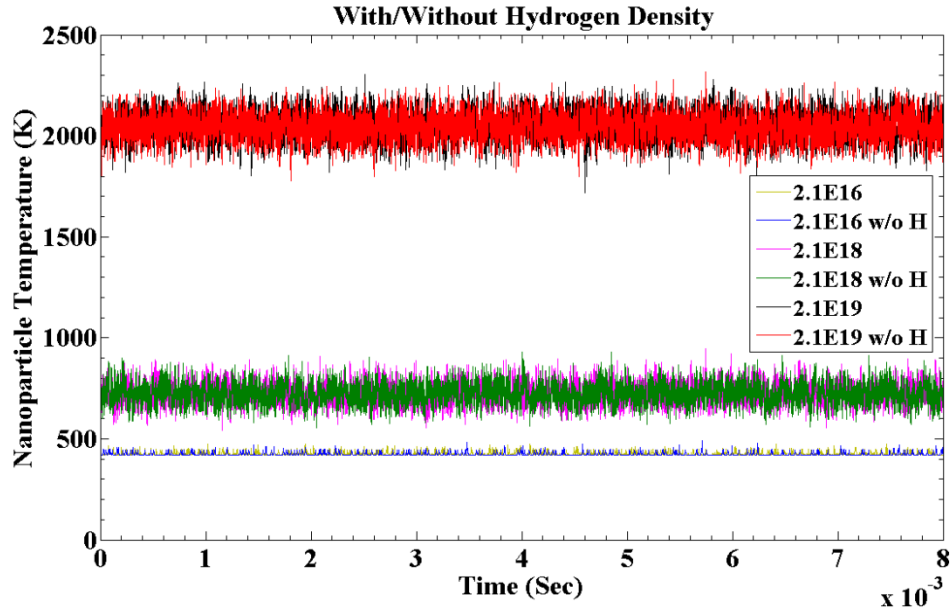


Figure B.5: Effect of hydrogen density on the nanoparticle temperature. The ion density is the most important parameter; changing H<sub>2</sub> density did not make large changes in the nanoparticle temperature.

By analyzing all the results, we got the idea about the GaN nanoparticle crystallization process and the role of input parameters in achieving crystallization temperature. However, we have a future plan to study the real-time plasma characteristics of GaN synthesis to predict more accurate nanoparticle temperature and its crystallization mechanism.

## APPENDIX C

### Nucleation and Crystal Growth in Gas-Phase Process

A fundamental understanding of the nucleation and growth mechanism of Si NCs and GaN NCs is essential to our ability to achieve high-quality films. During synthesis, these nanoparticles go through nucleation and growth phases. Usually, nucleation can be categorized into two types: homogeneous nucleation and heterogeneous nucleation. Homogeneous nucleation occurs in the absence of any foreign nuclei or free surfaces, while, heterogeneous nucleation refers to the nucleation process in which the new phase forms on preexisting foreign nuclei or free surfaces. Both the homogeneous and heterogeneous nucleation process may be either single-component (homomolecular) involving a single chemical species, or multicomponent (heteromolecular), which involves more than one chemical species.

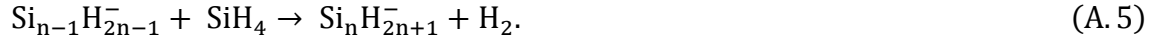
Synthesis of Si NCs and GaN NCs using plasma reactor in a fully gas-phase process was single component and multicomponent homogenous nucleation process respectively. However, surface nitridation of SiNCs using nitrogen with dual plasma process was a multicomponent heterogeneous process as the growth of silicon nitride (in secondary plasma) occurred on the pre-existing Si NCs from the primary plasma.

From experimental mass spectrometry measurements, it has been suggested that the earliest stages of particle formation in this system mainly involve the following sequence of ion-molecule reactions<sup>243-247</sup>:





·  
·  
·



It is a known fact that the hydrogen addition would suppress the particle nucleation in silane systems<sup>248,249</sup>. The possible reason could be that the hydrogen appears as a product species in the reaction sequence and therefore would suppress the cluster formation if the reactions were reversible.

Nucleation and crystal growth process of GaN nanoparticles in a non-thermal flow-through plasma reactor has not been investigated till date. Although, several studies has been performed on GaN growth process in a gas-phase mode in the past decades.

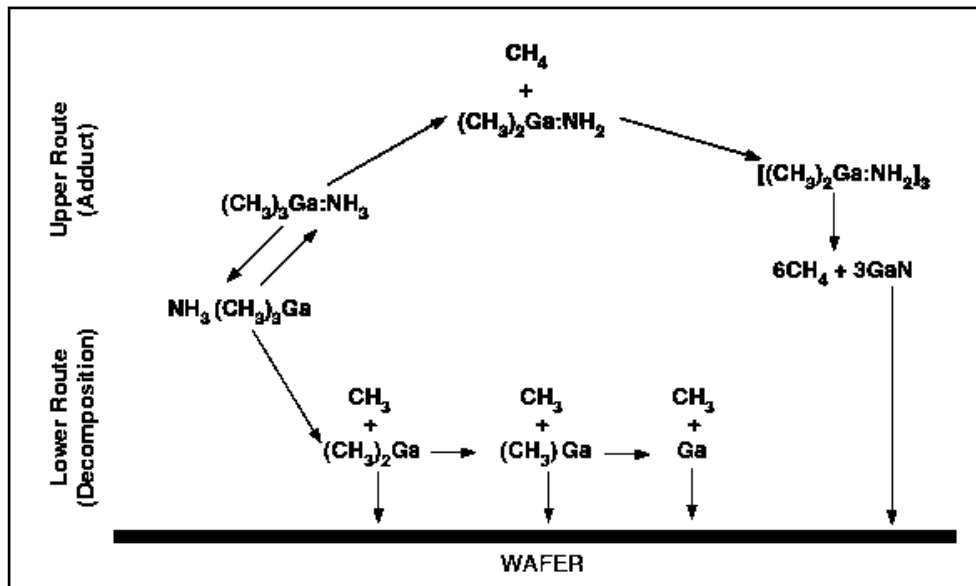


Figure C.1: Gallium Nitride synthesis route (Adapted from Parikh et al.<sup>250</sup>).

TMGa decomposition pathway was studied by Parikh et al<sup>250</sup> using a kinetic model and the reaction pathway is shown below:



They have used Metalorganic Vapor Phase Epitaxy (MOVPE) process for the synthesis of GaN nanoparticles for which adduct formation is very common. These adduct formation is shown in Figure C.1 and it can degrade the nanoparticle quality.

## BIBLIOGRAPHY

## BIBLIOGRAPHY

1. Independent Statistics & Analysis: U.S. Energy Information Administration FAQs. at <<http://www.eia.gov/tools/faqs/>>
2. ENERGY.GOV: Office of Energy Efficiency & Renewable Energy, Solid-State Lighting Program Homepage. at <<http://energy.gov/eere/ssl/solid-state-lighting>>
3. Navigant Consulting. 2010 U.S. Lighting Market Characterization. 100 (2012). at <<http://apps1.eere.energy.gov/buildings/publications/pdfs/ssl/2010-lmc-final-jan-2012.pdf>>
4. Narukawa, Y., Ichikawa, M., Sanga, D., Sano, M. & Mukai, T. White light emitting diodes with super-high luminous efficacy. *J. Phys. D. Appl. Phys.* **43**, 354002-1–6 (2010).
5. Hall, R. N., Fenner, G. E., Kingsley, J. D., Soltys, T. J. & Carlson, R. O. Coherent light emission from GaAs junctions. *Phys. Rev. Lett.* **9**, 366–368 (1962).
6. Nathan, M. I., Dumke, W. P., Burns, G., Dill, F. H. & Lasher, G. Stimulated emission of radiation from GaAs p-n junctions. *Appl. Phys. Lett.* **1**, 62–64 (1962).
7. Woodall, J. M. Ga<sub>1-x</sub>Al<sub>x</sub>As LED Structures Grown on GaP Substrates. *Appl. Phys. Lett.* **20**, 375 (1972).
8. Herzog, A. H., Groves, W. O. & Craford, M. G. Electroluminescence of diffused GaAs<sub>1-x</sub>P<sub>x</sub> Diodes with low donor concentrations. *J. Appl. Phys.* **40**, 1830–1838 (1969).
9. *Assessment of Advanced Solid State Lighting*. (2013). doi:10.17226/18279
10. Amano, H., Asahi, T. & Akasaki, I. Stimulated Emission Near Ultraviolet at Room Temperature from a GaN Film Grown on Sapphire by MOVPE Using an AlN Buffer Layer. *Jpn. J. Appl. Phys.* **29**, L205–L206 (1990).
11. Akasaki, I., Amano, H., Kito, M. & Hiramatsu, K. Photoluminescence of Mg-doped p-type GaN and electroluminescence of GaN p-n junction LED. **49**, 666–670 (1991).
12. Akasaki, I. & Amano, H. Widegap Column-III Nitride Semiconductors for UV/Blue Light Emitting Devices. *J. Electrochem. Soc.* **141**, 2266–2271 (1994).
13. Nakamura, S., Mukai, T. & Senoh, M. Candela-class high-brightness InGaN/AlGaIn double-heterostructure blue-light-emitting diodes. *Appl. Phys. Lett.* **64**, 1687–1689 (1994).
14. Canham, L. Progress Toward Crystalline Silicon-Based Light-Emitting Diodes. 22–28 (1993).
15. Ng, W. L. *et al.* An efficient room-temperature silicon-based light-emitting diode. *Nature* **410**, 192–4 (2001).
16. Kveder, V. *et al.* Room-temperature silicon light-emitting diodes based on dislocation luminescence. *Appl. Phys. Lett.* **84**, 2106–2108 (2004).

17. Takagahara, T. & Takeda, K. Theory of the quantum confinement effect on excitons in quantum dots of indirect-gap materials. *Phys. Rev. B* **46**, 15578–15581 (1992).
18. Proot, J. P., Delerue, C. & Allan, G. Electronic structure and optical properties of silicon crystallites: Application to porous silicon. *Appl. Phys. Lett.* **61**, 1948–1950 (1992).
19. Ledoux, G. *et al.* Photoluminescence properties of silicon nanocrystals as a function of their size. *Phys. Rev. B* **62**, 15942–15951 (2000).
20. Maier-Flaig, F. *et al.* Multicolor Silicon Light-Emitting Diodes (SiLEDs). *Nano Lett.* **13**, 475–480 (2013).
21. Fujita, S. & Sugiyama, N. Visible light-emitting devices with Schottky contacts on an ultrathin amorphous silicon layer containing silicon nanocrystals. *Appl. Phys. Lett.* **74**, 308–310 (1999).
22. De La Torre, J. *et al.* Optical properties of silicon nanocrystal LEDs. *Phys. E* **16**, 326–330 (2003).
23. Liu, C.-Y., Holman, Z. C. & Kortshagen, U. R. Hybrid Solar Cells from P3HT and Silicon Nanocrystals. *Nano Lett.* **9**, 449–452 (2009).
24. Tian, B. *et al.* Coaxial silicon nanowires as solar cells and nanoelectronic power sources. *Nature* **449**, 885–890 (2007).
25. Conibeer, G. *et al.* Silicon nanostructures for third generation photovoltaic solar cells. *Thin Solid Films* **511–512**, 654–662 (2006).
26. Timmerman, D., Izeddin, I., Stallinga, P., Yassievich, I. N. & Gregorkiewicz, T. Space-separated quantum cutting with silicon nanocrystals for photovoltaic applications. *Nat. Photonics* **2**, 105–109 (2008).
27. O'Farrell, N., Houlton, A. & Horrocks, B. R. Silicon nanoparticles: applications in cell biology and medicine. *Int. J. Nanomedicine* **1**, 451–472 (2006).
28. Fenollosa, R. *et al.* Silicon particles as trojan horses for potential cancer therapy. *J. Nanobiotechnology* **12**, 1–10 (2014).
29. Timoshenko, V. Y. *et al.* Silicon nanocrystals as photosensitizers of active oxygen for biomedical applications. *JETP Lett.* **83**, 423–426 (2006).
30. Debieu, O. Optical characterization of luminescent silicon nanocrystals embedded in glass matrices. (2008).
31. Canham, L. T. Silicon quantum wire array fabrication by electrochemical and chemical dissolution of wafers. *Appl. Phys. Lett.* **57**, 1046–1048 (1990).
32. Delerue, C., Allan, G. & Lannoo, M. Theoretical aspects of the luminescence of porous silicon. *Phys. Rev. B* **48**, 11024–11036 (1993).
33. Wölz, M. Control of the emission wavelength of gallium nitride-based nanowire light-

- emitting diodes. (2013).
34. Schubert, E. F. *Light-Emitting Diodes. Cambridge University Press* (2006). doi:<http://dx.doi.org/10.1017/CBO9780511790546>
  35. Holmes, J. D. *et al.* Highly luminescent silicon nanocrystals with discrete optical transitions. *J. Am. Chem. Soc.* **123**, 3743–3748 (2001).
  36. Liu, Q. & Kauzlarich, S. M. A new synthetic route for the synthesis of hydrogen terminated silicon nanoparticles. *Mater. Sci. Eng. B* **96**, 72–75 (2002).
  37. Littau, K. A., Szajowski, P. J., Muller, A. J., Kortan, A. R. & Brus, L. E. A Luminescent Silicon Nanocrystal Colloid Via a High-Temperature Aerosol Reaction. *J. Phys. Chem.* **97**, 1224–1230 (1993).
  38. Onischuk, A. A. *et al.* Aerosol formation under heterogeneous/homogeneous thermal decomposition of silane: experiment and numerical modeling. *J. Aerosol Sci.* **31**, 879–906 (2000).
  39. Li, X., He, Y., Talukdar, S. S. & Swihart, M. T. Process for preparing macroscopic quantities of brightly photoluminescent silicon nanoparticles with emission spanning the visible spectrum. *Langmuir* **19**, 8490–8496 (2003).
  40. Brus, L., Szajowski, P. & Wilson, W. Electronic spectroscopy and photophysics of Si nanocrystals: relationship to bulk c-Si and porous Si. *J. Am. Chem. Soc.* **117**, 2915–2922 (1995).
  41. Garrido Fernandez, B. *et al.* Influence of average size and interface passivation on the spectral emission of Si nanocrystals embedded in SiO<sub>2</sub>. *J. Appl. Phys.* **91**, 798–807 (2002).
  42. Irrera, A. *et al.* Electroluminescence and transport properties in amorphous silicon nanostructures. *Nanotechnology* **17**, 1428–1436 (2006).
  43. Pi, X. D. *et al.* Light emission from Si nanoclusters formed at low temperatures. *Appl. Phys. Lett.* **88**, (2006).
  44. Nozaki, T., Sasaki, K., Ogino, T., Asahi, D. & Okazaki, K. Microplasma synthesis of tunable photoluminescent silicon nanocrystals. *Nanotechnology* **18**, 235603 (2007).
  45. Gupta, A., Swihart, M. T. & Wiggers, H. Luminescent colloidal dispersion of silicon quantum dots from microwave plasma synthesis: Exploring the photoluminescence behavior across the visible spectrum. *Adv. Funct. Mater.* **19**, 696–703 (2009).
  46. Sankaran, R. M., Holunga, D., Flagan, R. C. & G. K. P. Synthesis of Blue Luminescent Si Nanoparticles Using Atmospheric-Pressure Microdischarges. *Nano Lett.* **5**, 537–541 (2005).
  47. Dogan, I. *et al.* Ultrahigh throughput plasma processing of free standing silicon nanocrystals with lognormal size distribution. *J. Appl. Phys.* **113**, 134306-1–10 (2013).

48. Dogan, I. & Van De Sanden, M. C. M. Direct characterization of nanocrystal size distribution using Raman spectroscopy. *J. Appl. Phys.* **114**, 134310-1–8 (2013).
49. Anthony, R. J. Structure and surface correlations to the optical properties of nonthermal plasma- produced silicon nanoparticles. (2011).
50. Mangolini, L., Thimsen, E. & Kortshagen, U. High-yield plasma synthesis of luminescent silicon nanocrystals. *Nano Lett.* **5**, 655–659 (2005).
51. Lopez, T. & Mangolini, L. On the nucleation and crystallization of nanoparticles in continuous-flow nonthermal plasma reactors. *J. Vac. Sci. Technol. B* **32**, 61802-1–8 (2014).
52. Askari, S., Levchenko, I., Ostrikov, K., Maguire, P. & Mariotti, D. Crystalline Si nanoparticles below crystallization threshold: Effects of collisional heating in non-thermal atmospheric-pressure microplasmas. *Appl. Phys. Lett.* **104**, 163103-1–5 (2014).
53. Le Picard, R., Markosyan, A. H., Porter, D. H., Girshick, S. L. & Kushner, M. J. Synthesis of Silicon Nanoparticles in Nonthermal Capacitively-Coupled Flowing Plasmas: Processes and Transport. *Plasma Chem. Plasma Process.* (2016). doi:10.1007/s11090-016-9721-6
54. Bapat, A. *et al.* Plasma synthesis of single-crystal silicon nanoparticles for novel electronic device applications. *Plasma Phys. Control. Fusion* **46**, B97–B109 (2004).
55. Mangolini, L. & Kortshagen, U. Selective nanoparticle heating: Another form of nonequilibrium in dusty plasmas. *Phys. Rev. E* **79**, 26405-1–8 (2009).
56. Kramer, N. J., Anthony, R. J., Mamunuru, M., Aydil, E. S. & Kortshagen, U. R. Plasma-induced crystallization of silicon nanoparticles. *J. Phys. D: Appl. Phys.* **47**, 1–8 (2014).
57. Pereira, R. N., Rowe, D. J., Anthony, R. J. & Kortshagen, U. Freestanding silicon nanocrystals with extremely low defect content. *Phys. Rev. B* **86**, 1–6 (2012).
58. Mangolini, L., Jurbergs, D., Rogojina, E. & Kortshagen, U. Plasma synthesis and liquid-phase surface passivation of brightly luminescent Si nanocrystals. *J. Lumin.* **121**, 327–334 (2006).
59. Anthony, R. & Kortshagen, U. Photoluminescence quantum yields of amorphous and crystalline silicon nanoparticles. *Phys. Rev. B* **80**, 115407 (2009).
60. Anthony, R. J., Cheng, K.-Y., Holman, Z. C., Holmes, R. J. & Kortshagen, U. R. An all-gas-phase approach for the fabrication of silicon nanocrystal light-emitting devices. *Nano Lett.* **12**, 2822–2825 (2012).
61. Anthony, R. J., Rowe, D. J., Stein, M., Yang, J. & Kortshagen, U. Routes to achieving high quantum yield luminescence from gas-phase-produced silicon nanocrystals. *Adv. Funct. Mater.* **21**, 4042–4046 (2011).
62. Weeks, S. L., MacCo, B., Van De Sanden, M. C. M. & Agarwal, S. Gas-phase hydrosilylation of plasma-synthesized silicon nanocrystals with short- and long-chain

- alkynes. *Langmuir* **28**, 17295–17301 (2012).
63. Agarwal, S., Quax, G. W. W., van de Sanden, M. C. M., Maroudas, D. & Aydil, E. S. Measurement of absolute radical densities in a plasma using modulated-beam line-of-sight threshold ionization mass spectrometry. *J. Vac. Sci. Technol. A* **22**, 71–81 (2004).
  64. Kramer, N. J., Schramke, K. S. & Kortshagen, U. R. Plasmonic Properties of Silicon Nanocrystals Doped with Boron and Phosphorus. *Nano Lett.* **15**, 5597–5603 (2015).
  65. Zhou, S. *et al.* Comparative Study on the Localized Surface Plasmon Resonance Silicon Nanocrystals. *ACS Nano* 378–386 (2015). doi:10.1021/nn505416r
  66. Wheeler, L. M., Neale, N. R., Chen, T. & Kortshagen, U. R. Hypervalent surface interactions for colloidal stability and doping of silicon nanocrystals. *Nat. Commun.* **4**, 1–10 (2013).
  67. Gresback, R., Holman, Z. & Kortshagen, U. Nonthermal plasma synthesis of size-controlled, monodisperse, freestanding germanium nanocrystals. *Appl. Phys. Lett.* **91**, 0–3 (2007).
  68. Gresback, R., Hue, R., Gladfelter, W. L. & Kortshagen, U. R. Combined plasma gas-phase synthesis and colloidal processing of InP/ZnS core/shell nanocrystals. *Nanoscale Res. Lett.* **6**, 68 (2011).
  69. Anthony, R., Thimsen, E., Johnson, J., Campbell, S. & Kortshagen, U. A Non-thermal plasma reactor for the synthesis of gallium nitride nanocrystals. *Mater. Res. Soc. Symp. Proc.* **892**, 5–8 (2006).
  70. Pi, X. D. & Kortshagen, U. Nonthermal plasma synthesized freestanding silicon-germanium alloy nanocrystals. *Nanotechnology* **20**, 295602 (2009).
  71. Holman, Z. C. & Kortshagen, U. R. A flexible method for depositing dense nanocrystal thin films: impaction of germanium nanocrystals. *Nanotechnology* **21**, 1–9 (2010).
  72. Nozaki, T., Sasaki, K., Ogino, T., Asahi, D. & Okazaki, K. Silicon Nanocrystal Synthesis in Microplasma Reactor. *J. Therm. Sci. Technol.* **2**, 192–199 (2007).
  73. Wu, J. J., Siva Santosh Kumar Kondeti, V., Bruggeman, P. J. & Kortshagen, U. R. Luminescent, water-soluble silicon quantum dots via micro-plasma surface treatment. *J. Phys. D. Appl. Phys.* **49**, 1–6 (2016).
  74. Bilik, N., Greenberg, B. L., Yang, J., Aydil, E. S. & Kortshagen, U. R. Atmospheric-pressure glow plasma synthesis of plasmonic and photoluminescent zinc oxide nanocrystals. *J. Appl. Phys.* **119**, 243302-1–6 (2016).
  75. Botas, A. M. P. *et al.* High Quantum Yield Dual-emission from Gas Phase Grown Crystalline Si Nanoparticles. *J. Phys. Chem. C* **118**, 10375–10383 (2014).
  76. Felbier, P. *et al.* Highly luminescent ZnO quantum dots made in a nonthermal plasma. *Adv. Funct. Mater.* **24**, 1988–1993 (2014).

77. Jurbergs, D., Rogojina, E., Mangolini, L. & Kortshagen, U. Silicon nanocrystals with ensemble quantum yields exceeding 60%. *Appl. Phys. Lett.* **88**, 60–63 (2006).
78. Buriak, J. M. Organometallic Chemistry on Silicon and Germanium Surface. *Chem. Rev.* **102**, 1271–1308 (2002).
79. Scalf, J. & West, P. *Part I: Introduction to Nanoparticle Characterization with AFM. Pacific nanotechnology* (2006). at <<http://www.nanoparticles.org/pdf/Scalf-West.pdf>>
80. Marangoni, A. G. & Peyronel, M. F. X-Ray Powder Diffractometry. *AOCS Lipid Library* at <<http://lipidlibrary.aocs.org/Biochemistry/content.cfm?ItemNumber=40299>>
81. XPS: Xray Photoelectron Spectroscopy. *Thermo Fisher Scientific* at <<http://www.lasurface.com/xps/>>
82. Bruker. [www.bruker-biospin.com](http://www.bruker-biospin.com).
83. Sangghaleh, F., Sychugov, I., Yang, Z., Veinot, J. G. C. & Linnros, J. Near-Unity Internal Quantum Efficiency of Luminescent Silicon Nanocrystals with Ligand Passivation. *ACS Nano* **9**, 7097–7104 (2015).
84. Di Fonzo, F. *et al.* Focused nanoparticle-beam deposition of patterned microstructures. *Appl. Phys. Lett.* **77**, 910–912 (2000).
85. Iqbal, Z. & Veprek, S. Raman scattering from hydrogenated microcrystalline and amorphous silicon. *J. Phys. C Solid State Phys.* **15**, 377–392 (1982).
86. Sirenko, a. a. *et al.* In situ Raman scattering studies of the amorphous and crystalline Si nanoparticles. *Solid State Commun.* **113**, 553–558 (2000).
87. Kapaklis, V., Politis, C., Pouloupoulos, P. & Schweiss, P. Photoluminescence from silicon nanoparticles prepared from bulk amorphous silicon monoxide by the disproportionation reaction. *Appl. Phys. Lett.* **87**, 1–3 (2005).
88. Knipping, J. *et al.* Synthesis of high purity silicon nanoparticles in a low pressure microwave reactor. *J. Nanosci. Nanotechnol.* **4**, 1039–1044 (2004).
89. Trwoga, P., Kenyon, A. & Pitt, C. Modeling the contribution of quantum confinement to luminescence from silicon nanoclusters. *J. Appl. Phys.* **83**, 3789–3794 (1998).
90. Beard, M. C. *et al.* Multiple exciton generation in colloidal silicon nanocrystals. *Nano Lett.* **7**, 2506–2512 (2007).
91. Carlisle, J. A., Dongol, M., Germanenko, I. N., Pithawalla, Y. B. & El-Shall, M. S. Evidence for changes in the electronic and photoluminescence properties of surface-oxidized silicon nanocrystals induced by shrinking the size of the silicon core. *Chem. Phys. Lett.* **326**, 335–340 (2000).
92. Yang, D.-Q., Gillet, J.-N., Meunier, M. & Sacher, E. Room temperature oxidation kinetics of Si nanoparticles in air, determined by x-ray photoelectron spectroscopy. *J. Appl. Phys.* **97**, 24303 (2005).

93. Shiku, H. *et al.* Oxygen Permeability of Surface-modified Poly(dimethylsiloxane) Characterized by Scanning Electrochemical Microscopy. *Chem. Lett.* **35**, 234–235 (2006).
94. Lamberti, A., Marasso, S. L. & Cocuzza, M. PDMS membranes with tunable gas permeability for microfluidic applications. *RSC Adv.* **4**, 61415–61419 (2014).
95. Lee, K. J. *et al.* A printable form of single-crystalline gallium nitride for flexible optoelectronic systems. *Small* **1**, 1164–1168 (2005).
96. Honda, T. *et al.* Fabrication of GaN nanocrystallites and their application to UV/blue electroluminescent devices. *Phys. Status Solidi(a)* **201**, 2814–2817 (2004).
97. Chitara, B., Venkataprasad Bhat, S., Vivekchand, S. R. C., Gomathi, A. & Rao, C. N. R. White-light sources based on composites of GaN nanocrystals with conducting polymers and nanophosphors. *Solid State Commun.* **147**, 409–413 (2008).
98. Slimane, A. Ben *et al.* On the phenomenon of large photoluminescence red shift in GaN nanoparticles. *Nanoscale Res. Lett.* **8**, 1–6 (2013).
99. Damilano, B., Grandjean, N., Massies, J. & Semond, F. GaN and GaInN quantum dots: an efficient way to get luminescence in the visible spectrum range. *Appl. Surf. Sci.* **164**, 241–245 (2000).
100. Kendrick, C. E. *et al.* Polycrystalline InGaN grown by MBE on fused silica glass. *Phys. Status Solidi(c)* **2**, 2236–2239 (2005).
101. Tang, H. *et al.* Properties of carbon-doped GaN. *Appl. Phys. Lett.* **78**, 757–759 (2001).
102. Ogi, T. *et al.* Fabrication and photoluminescence of highly crystalline GaN and GaN:Mg nanoparticles. *J. Cryst. Growth* **281**, 234–241 (2005).
103. Li, H. D. *et al.* Raman spectroscopy of nanocrystalline GaN synthesized by arc plasma. *J. Appl. Phys.* **91**, 4562–4567 (2002).
104. Sofer, Z. *et al.* Rapid thermal synthesis of GaN nanocrystals and nanodisks. *J. Nanoparticle Res.* **15**, 1–7 (2013).
105. Sinha, G., Ganguli, D. & Chaudhuri, S. Ga<sub>2</sub>O<sub>3</sub> and GaN nanocrystalline film: Reverse micelle assisted solvothermal synthesis and characterization. *J. Colloid Interface Sci.* **319**, 123–129 (2008).
106. Suresh Kumar, V., Kumar, J., Srivastava, R. K., Srivastava, A. & Srivastava, O. N. Growth and characterization of gallium nitride nanocrystals on carbon nanotubes. *J. Cryst. Growth* **310**, 2260–2263 (2008).
107. Jung, W. S. & Min, B. K. Synthesis of gallium nitride powders and nanowires from gallium oxyhydroxide under a flow of ammonia. *Mater. Lett.* **58**, 3058–3062 (2004).
108. Goodwin, T. J., Leppert, V. J., Risbud, S. H., Kennedy, I. M. & Lee, H. W. H. Synthesis of gallium nitride quantum dots through reactive laser ablation. *Appl. Phys. Lett.* **70**, 3122 (1997).

109. Azuma, Y., Shimada, M. & Okuyama, K. The synthesis of monodisperse ultrapure gallium nitride nanoparticles by MOCVD. *Chem. Vap. Depos.* **10**, 11–13 (2004).
110. Qiu, H., Cao, C. & Zhu, H. Synthesis of nanocrystalline GaN by the sol-gel method. *Mater. Sci. Eng. B* **136**, 33–36 (2007).
111. Mičić, O. I., Ahrenkiel, S. P., Bertram, D. & Nozik, A. J. Synthesis, structure, and optical properties of colloidal GaN quantum dots. *Appl. Phys. Lett.* **75**, 478–480 (1999).
112. Shimada, M., Azuma, Y., Okuyama, K., Hayashi, Y. & Tanabe, E. Plasma synthesis of light emitting gallium nitride nanoparticles using a novel microwave-resonant cavity. *Japanese J. Appl. Physics, Part* **45**, 328–332 (2006).
113. Greenberg, B. L. *et al.* Nonequilibrium-Plasma-Synthesized ZnO Nanocrystals with Plasmon Resonance Tunable via Al Doping and Quantum Confinement. *Nano Lett.* **15**, 8162–8169 (2015).
114. Abràmoff, M. D., Magalhães, P. J. & Ram, S. J. Image processing with imageJ. *Biophotonics Int.* **11**, 36–41 (2004).
115. Schneider, C. A., Rasband, W. S. & Eliceiri, K. W. NIH Image to ImageJ: 25 years of image analysis. *Nat. Methods* **9**, 671–675 (2012).
116. Levinshtein, M.E., Rumyantsev, S.L. & Shur, M. S. *Properties of Advanced Semiconductor Materials: GaN, AlN, InN, BN, and SiGe.* (John Wiley and Sons, 2001).
117. Porowski, S. Growth and properties of single crystalline GaN substrates and homoepitaxial layers. *Mater. Sci. Eng. B* **44**, 407–413 (1997).
118. Florescu, D. I. *et al.* Thermal conductivity of fully and partially coalesced lateral epitaxial overgrown GaN/sapphire (0001) by scanning thermal microscopy. *Appl. Phys. Lett.* **77**, 1464 (2000).
119. Krukowski, S., Leszcynski, M. & Porowski, S. *In: Properties, Processing and Applications of Gallium Nitride and Related Semiconductors.* (INSPEC, 1999).
120. Kucheyev, S. O. *et al.* Nanoindentation of epitaxial GaN films. *Appl. Phys. Lett.* **77**, 3373 (2000).
121. Guiquan, P., Kordesch, M. E. & Van Patten, P. G. Pyrolysis route to GaN quantum dots. *Chem. Mater.* **18**, 3915–3917 (2006).
122. Gyger, F., Bockstaller, P., Gröger, H., Gerthsen, D. & Feldmann, C. Quantum-confined GaN nanoparticles synthesized via liquid-ammonia-in-oil-microemulsions. *Chem. Commun.* **50**, 2939–42 (2014).
123. Giroire, B., Marre, S., Garcia, A., Cardinal, T. & Aymonier, C. Continuous supercritical route for quantum-confined GaN nanoparticles. *React. Chem. Eng.* **1**, 151–155 (2016).
124. Yu, L. *et al.* A soluble salt-assisted facile synthetic route to semiconducting GaN nanoparticles. *CrystEngComm* **12**, 2037–2039 (2010).

125. Bungaro, C., Rapcewicz, K. & Bernholc, J. Ab initio phonon dispersions of wurtzite AlN, GaN, and InN. *Phys. Rev. B* **61**, 6720–6725 (2000).
126. Trodahl, H. J. *et al.* Raman spectroscopy of nanocrystalline and amorphous GaN. *J. Appl. Phys.* **97**, 1–6 (2005).
127. Parkinson, B. G. *et al.* Quantitative measurement of Q3 species in silicate and borosilicate glasses using Raman spectroscopy. *J. Non. Cryst. Solids* **354**, 1936–1942 (2008).
128. Yadav, A. K. & Singh, P. A Review on Structure of Glasses by Raman Spectroscopy. *RSC Adv.* **5**, 67583–67609 (2015).
129. Bittar, A., Trodahl, H. J., Kemp, N. T. & Markwitz, A. Ion-assisted deposition of amorphous GaN: Raman and optical properties. *Appl. Phys. Lett.* **78**, 619–621 (2001).
130. Limmer, W. *et al.* Raman scattering in ion-implanted GaN. *Appl. Phys. Lett.* **72**, 2589–2591 (1998).
131. Wieser, N. *et al.* Disorder-activated scattering and two-mode behavior in Raman spectra of isotopic GaN and AlGaN. *Phys. Status Solidi(b)* **216**, 807–811 (1999).
132. Giehler, M., Ramsteiner, M., Brandt, O., Yang, H. & Ploog, K. H. Optical phonons of hexagonal and cubic GaN studied by infrared transmission and Raman spectroscopy. *Appl. Phys. Lett.* **67**, 733–735 (1995).
133. Tabata, a. *et al.* Comparative Raman studies of cubic and hexagonal GaN epitaxial layers. *J. Appl. Phys.* **79**, 4137–4140 (1996).
134. Bhaviripudi, S., Qi, J., Hu, E. L. & Belcher, A. M. Synthesis , Characterization , and Optical Properties of Ordered Arrays of III-Nitride Nanocrystals. *Nano Lett.* **7**, 3512–3517 (2007).
135. Kumar, M. *et al.* Facile synthesis and photoluminescence spectroscopy of 3D-triangular GaN nano prism islands. *Dalt. Trans.* **43**, 11855–61 (2014).
136. Jung, W. Reaction intermediate(s) in the conversion of  $\beta$ -gallium oxide to gallium nitride under a flow of ammonia. *Mater. Lett.* **57**, 110–114 (2002).
137. Cao, Y. G., Chen, X. L., Li, J. Y., Lan, Y. C. & Liang, J. K. Observation of a quantum-confinement effect with GaN nanoparticles synthesized through a new gas reaction route. *Appl. Phys. A* **71**, 229–231 (2000).
138. Kudrawiec, R. *et al.* Photoluminescence from GaN nanopowder: The size effect associated with the surface-to-volume ratio. *Appl. Phys. Lett.* **88**, 1–3 (2006).
139. Bondar, V. Properties of nanocrystalline gallium nitride thin films grown on monocrytalline substrates and buffer layers. *Phys. Status Solidi(a)* **176**, 635–638 (1999).
140. Reshchikov, M. A. *et al.* Unstable luminescence in GaN and ZnO. *Phys. B* **376–377**, 715–718 (2006).

141. Suzuki, M., Uenoyama, T. & Yanase, A. First-principles calculations of effective-mass parameters of AlN and GaN. *Phys. Rev. B* **52**, 8132–8139 (1995).
142. Yang, Y. *et al.* Blue luminescence from amorphous GaN nanoparticles synthesized in situ in a polymer. *Appl. Phys. Lett.* **74**, 2262–2264 (1999).
143. Stumm, P. & Drabold, D. Can Amorphous GaN Serve as a Useful Electronic Material? *Phys. Rev. Lett.* **79**, 677–680 (1997).
144. Park, J. K. *et al.* White light-emitting diodes of GaN-based Sr<sub>2</sub>SiO<sub>4</sub>:Eu and the luminescent properties. *Appl. Phys. Lett.* **82**, 683–685 (2003).
145. Sheu, J. K. *et al.* White-light emission from near UV InGaN-GaN LED chip precoated with blue/green/red phosphors. *IEEE Photonics Technol. Lett.* **15**, 18–20 (2003).
146. Mukai, T., Yamada, M. & Nakamura, S. Characteristics of InGaN-Based UV / Blue / Green / Amber / Red Light-Emitting Diodes. *Jpn. J. Appl. Phys.* **38**, 3976–3981 (1999).
147. Bouguerra, M. *et al.* Blue and yellow luminescence of GaN nanocrystals-doped SiO<sub>2</sub> matrix. *Phys. E* **41**, 292–298 (2008).
148. Mangolini, L. & Kortshagen, U. Plasma-assisted synthesis of silicon nanocrystal inks. *Adv. Mater.* **19**, 2513–2519 (2007).
149. Von Bardeleben, H. J. *et al.* Identification of the nitrogen split interstitial (N-N)N in GaN. *Phys. Rev. Lett.* **109**, 1–5 (2012).
150. Chow, K., Watkins, G., Usui, A. & Mizuta, M. Detection of Interstitial Ga in GaN. *Phys. Rev. Lett.* **85**, 2761–2764 (2000).
151. Chow, K. *et al.* Publisher's Note: Intrinsic defects in GaN. I. Ga sublattice defects observed by optical detection of electron paramagnetic resonance [Phys. Rev. B 69, 045207 (2004)]. *Phys. Rev. B* **69**, 1–9 (2004).
152. Saarinen, K., Suski, T., Grzegory, I. & Look, D. Thermal stability of isolated and complexed Ga vacancies in GaN bulk crystals. *Phys. Rev. B* **64**, 1–4 (2001).
153. Baranov, P. G. *et al.* Internet Journal Nitride Semiconductor Research. *MRS Internet J. Nitride Semicond. Res.* **3**, 1–17 (1998).
154. Qiu, C. H. & Pankove, J. I. Deep levels and persistent photoconductivity in GaN thin films. *Appl. Phys. Lett.* **70**, 1983–1985 (1997).
155. Cullis, A. G. & Canham, L. T. Visible light emission due to quantum size effects in highly porous crystalline silicon. *Nature* **353**, 335–338 (1991).
156. Wilson, W. L., Szajowski, P. F. & Brus, L. E. Quantum confinement in size-selected, surface-oxidized silicon nanocrystals. *Science (80-. )*. **262**, 1242–1244 (1993).
157. Lu, Z. H., Lockwood, D. J. & Baribeau, J.-M. Quantum confinement and light emission in SiO<sub>2</sub>/Si superlattices. *Nature* **378**, 258–260 (1995).

158. Lin, G. R., Pai, Y. H., Lin, C. T. & Chen, C. C. Comparison on the electroluminescence of Si-rich SiNx and SiOx based light-emitting diodes. *Appl. Phys. Lett.* **96**, 1–3 (2010).
159. Park, N.-M., Kim, T.-S. & Park, S.-J. Band gap engineering of amorphous silicon quantum dots for light-emitting diodes. *Appl. Phys. Lett.* **78**, 2575–2577 (2001).
160. Perálvarez, M. *et al.* Si-nanocrystal-based LEDs fabricated by ion implantation and plasma-enhanced chemical vapour deposition. *Nanotechnology* **20**, 1–10 (2009).
161. Cheng, K., Anthony, R., Kortshagen, U. R. & Holmes, R. J. High-Efficiency Silicon Nanocrystal Light-Emitting Devices. *Nano Lett.* **11**, 1952–1956 (2011).
162. Tamura, H., Rückschloss, M., Wirschem, T. & Vepřek, S. Origin of the green/blue luminescence from nanocrystalline silicon. *Appl. Phys. Lett.* **65**, 1537–1539 (1994).
163. Liao, L. S., Bao, X. M., Zheng, X. Q., Li, N. S. & Min, N. Ben. Blue luminescence from Si<sup>+</sup>-implanted SiO<sub>2</sub> films thermally grown on crystalline silicon. *Appl. Phys. Lett.* **68**, 850–852 (1996).
164. Park, N.-M., Choi, C.-J., Seong, T.-Y. & Park, S.-J. Quantum Confinement in Amorphous Silicon Quantum Dots Embedded in Silicon Nitride. *Phys. Rev. Lett.* **86**, 1355–1357 (2001).
165. Wang, Y. Q., Wang, Y. G., Cao, L. & Cao, Z. X. High-efficiency visible photoluminescence from amorphous silicon nanoparticles embedded in silicon nitride. *Appl. Phys. Lett.* **83**, 3474–3476 (2003).
166. Kim, T. Y. *et al.* Quantum confinement effect of silicon nanocrystals in situ grown in silicon nitride films. *Appl. Phys. Lett.* **85**, 5355–5357 (2004).
167. Rodriguez-Gómez, A., García-Valenzuela, A., Haro-Poniatowski, E. & Alonso-Huitrón, J. C. Effect of thickness on the photoluminescence of silicon quantum dots embedded in silicon nitride films. *J. Appl. Phys.* **113**, 1–10 (2013).
168. Goncharova, L. V. *et al.* Si quantum dots in silicon nitride: Quantum confinement and defects. *J. Appl. Phys.* **118**, 1–8 (2015).
169. Kim, T.-W., Cho, C.-H., Kim, B.-H. & Park, S.-J. Quantum confinement effect in crystalline silicon quantum dots in silicon nitride grown using SiH<sub>4</sub> and NH<sub>3</sub>. *Appl. Phys. Lett.* **88**, 1–3 (2006).
170. Chen, K., Huang, X., Xu, J. & Feng, D. Visible photoluminescence in crystallized amorphous Si:H/SiNx:H multiquantum-well structures. *Appl. Phys. Lett.* **61**, 2069–2071 (1992).
171. Huang, X. *et al.* Microstructures and optical properties in crystallized a-Si:H multi-quantum wells using excimer laser annealing. *J. Non. Cryst. Solids* **198–200**, 821–824 (1996).
172. Wang, M. *et al.* Observation of the size-dependent blueshifted electroluminescence from

- nanocrystalline Si fabricated by KrF excimer laser annealing of hydrogenated amorphous silicon/amorphous-SiN<sub>x</sub>:H superlattices. *Appl. Phys. Lett.* **72**, 722–724 (1998).
173. Kurokawa, Y., Miyajima, S., Yamada, A. & Konagai, M. Preparation of Nanocrystalline Silicon in Amorphous Silicon Carbide Matrix. *Jpn. J. Appl. Phys.* **45**, L1064–L1066 (2006).
  174. Song, D. *et al.* Fabrication and characterization of Si nanocrystals in SiC matrix produced by magnetron cosputtering. *J. Vac. Sci. Technol. B* **25**, 1327–1335 (2007).
  175. Eun-Chel, C. *et al.* Silicon quantum dot/crystalline silicon solar cells. *Nanotechnology* **19**, 1–5 (2008).
  176. Barbagioanni, E. G., Lockwood, D. J., Simpson, P. J. & Goncharova, L. V. Quantum confinement in Si and Ge nanostructures: Theory and experiment. *Appl. Phys. Rev.* **1**, 1–47 (2014).
  177. Barbagioanni, E., Goncharova, L. & Simpson, P. Electronic structure study of ion-implanted Si quantum dots in a SiO<sub>2</sub> matrix: Analysis of quantum confinement theories. *Phys. Rev. B* **83**, 1–11 (2011).
  178. Iacona, F., Franzo, G. & Spinella, C. Correlation between luminescence and structural properties of Si nanocrystals. *J. Appl. Phys.* **87**, 1295–1303 (2000).
  179. Lockwood, R. & Meldrum, A. Luminescence simulations of ensembles of silicon nanocrystals. *Phys. Status Solidi(a)* **206**, 965–968 (2009).
  180. Backman, M. & Djurabekova, F. Amorphization of Ge and Si nanocrystals embedded in amorphous SiO<sub>2</sub> by ion irradiation. *Phys. Rev. B* **80**, 1–12 (2009).
  181. Rezgui, B., Sibai, A., Nychyporuk, T., Lemiti, M. & Brémond, G. Luminescence mechanisms in Si quantum dots-SiN<sub>x</sub> nanocomposite structures. *J. Vac. Sci. Technol. B* **27**, 2238–2241 (2009).
  182. Rezgui, B., Sibai, A., Nychyporuk, T., Lemiti, M. & Brémond, G. Photoluminescence and optical absorption properties of silicon quantum dots embedded in Si-rich silicon nitride matrices. *J. Lumin.* **129**, 1744–1746 (2009).
  183. Tsybeskov, L. *et al.* A Si-based light-emitting diode with room-temperature electroluminescence at 1.1 eV. *Appl. Phys. Lett.* **69**, 3411–3413 (1996).
  184. Kanemitsu, Y., Futagi, T., Matsumoto, T. & Mimura, H. Origin of the blue and red photoluminescence from oxidized porous silicon. *Phys. Rev. B* **49**, 14732–14735 (1994).
  185. Conibeer, G. *et al.* Silicon quantum dot nanostructures for tandem photovoltaic cells. *Thin Solid Films* **516**, 6748–6756 (2008).
  186. Uchida, G. *et al.* Surface nitridation of silicon nano-particles using double multi-hollow discharge plasma CVD. *Phys. Status Solidi C* **8**, 3017–3020 (2011).
  187. Weeks, S. L., Leick, N. & Agarwal, S. Silicon Nitride Encapsulated Silicon Nanocrystals

- for Lithium Ion Batteries. *Plasma Process. Polym.* **13**, 116–123 (2016).
188. Hu, Y. S. *et al.* Superior storage performance of a Si@SiO<sub>x</sub>/C nanocomposite as anode material for lithium-ion batteries. *Angew. Chemie - Int. Ed.* **47**, 1645–1649 (2008).
  189. Kasavajjula, U., Wang, C. & Appleby, A. J. Nano- and bulk-silicon-based insertion anodes for lithium-ion secondary cells. *J. Power Sources* **163**, 1003–1039 (2007).
  190. Liu, W. R. *et al.* Effect of electrode structure on performance of Si anode in Li-ion batteries: Si particle size and conductive additive. *J. Power Sources* **140**, 139–144 (2005).
  191. McDowell, M. T., Lee, S. W., Nix, W. D. & Cui, Y. 25th anniversary article: Understanding the lithiation of silicon and other alloying anodes for lithium-ion batteries. *Adv. Mater.* **25**, 4966–4985 (2013).
  192. Guo, J., Chen, X. & Wang, C. Carbon scaffold structured silicon anodes for lithium-ion batteries. *J. Mater. Chem.* **20**, 5035–5040 (2010).
  193. Wu, H. & Cui, Y. Designing nanostructured Si anodes for high energy lithium ion batteries. *Nano Today* **7**, 414–429 (2012).
  194. Park, M. H. *et al.* Silicon nanotube battery anodes. *Nano Lett.* **9**, 3844–3847 (2009).
  195. Wu, H. *et al.* Engineering Empty Space between Si Nanoparticles for Lithium Ion Battery Anodes. *Nano Lett.* **12**, 904–909 (2012).
  196. Yoshio, M. *et al.* Carbon-Coated Si as a Lithium-Ion Battery Anode Material. *J. Electrochem. Soc.* **149**, A1598–A1603 (2002).
  197. Ng, S. H. *et al.* Highly reversible lithium storage in spheroidal carbon-coated silicon nanocomposites as anodes for lithium-ion batteries. *Angew. Chemie - Int. Ed.* **45**, 6896–6899 (2006).
  198. Li, X. *et al.* Hollow core–shell structured porous Si–C nanocomposites for Li-ion battery anodes. *J. Mater. Chem.* **22**, 11014–11017 (2012).
  199. Takeda, N., Kobayashi, H. & Tsubomura, H. Fast direct nitridation of silicon with nitrogen plasma and its effect on the shift of flat-band potential. *Chem. Mater.* **3**, 305–309 (1991).
  200. Mohamed, S. H., Raaif, M., Abd El-Rahman, A. M. A. & Shaaban, E. R. Properties of rf plasma nitrided silicon thin films at different rf plasma processing powers. *Acta Phys. Pol. A* **120**, 552–557 (2011).
  201. Moslehi, M. M., Fu, C. Y., Sigmon, T. W. & Saraswat, K. C. Low-temperature direct nitridation of silicon in nitrogen plasma generated by microwave discharge. *J. Appl. Phys.* **58**, 2416–2419 (1985).
  202. Bahari, A., Robenhagen, U., Morgen, P. & Li, Z. S. Growth of ultrathin silicon nitride on Si(111) at low temperatures. *Phys. Rev. B* **72**, 1–6 (2005).

203. Morgen, P., Bahari, A., Pedersen, K. and Li, Z. S. Plasma assisted growth of ultrathin nitrides on Si surfaces under ultrahigh vacuum conditions. *J. Phys. Conf. Ser.* **86**, 1–19 (2007).
204. Marra, D. C., Edelberg, E. A., Naone, R. L. & Aydil, E. S. Silicon hydride composition of plasma-deposited hydrogenated amorphous and nanocrystalline silicon films and surfaces. *J. Vac. Sci. Technol. A* **16**, 3199–3210 (1998).
205. Scardera, G., Puzzer, T., Conibeer, G. & Green, M. A. Fourier transform infrared spectroscopy of annealed silicon-rich silicon nitride thin films. *J. Appl. Phys.* **104**, 1–8 (2008).
206. Hasegawa, S., Matsuda, M. & Kurata, Y. Si-H and N-H vibrational properties in glow-discharge amorphous SiN<sub>x</sub>:H films (0<x<1.55). *Appl. Phys. Lett.* **57**, 2211–2213 (1990).
207. Hasegawa, S., He, L., Amano, Y. & Inokuma, T. Analysis of SiH and SiN vibrational absorption in amorphous SiN<sub>x</sub>:H films in terms of a charge-transfer model. *Phys. Rev. B* **48**, 5315–5325 (1993).
208. Parsons, G. N. & Lucovsky, G. Silicon-hydrogen bond-stretching vibrations in hydrogenated amorphous silicon-nitrogen alloys. *Phys. Rev. B* **41**, 1664–1667 (1990).
209. Hasegawa, S., Anbutsu, H. & Kurata, Y. Connection between Si–N and Si–H vibrational properties in amorphous SiN<sub>x</sub>:H films. *Philos. Mag. Part B* **59**, 365–375 (1989).
210. Debieu, O. *et al.* Structural and optical characterization of pure Si-rich nitride thin films. *Nanoscale Res. Lett.* **8**, 1–13 (2013).
211. Li, T. & Kanicki, J. Observation of incident angle dependent phonon absorption in hydrogenated amorphous silicon nitride thin films. *Appl. Phys. Lett.* **73**, 3866–3868 (1998).
212. Berreman, D. W. Infrared absorption at longitudinal optic frequency in cubic crystal films. *Phys. Rev.* **130**, 2193–2198 (1963).
213. Hanyaloglu, B. F. & Aydil, E. S. Low temperature plasma deposition of silicon nitride from silane and nitrogen plasmas. *J. Vac. Sci. Technol. A* **16**, 2794–2803 (1998).
214. Lucovsky, G., Yang, J., Chao, S., Tyler, J. & Czubytyj, W. Nitrogen-bonding environments in glow-discharge—deposited a-Si:H films. *Phys. Rev. B* **28**, 3234–3240 (1983).
215. Jariwala, B. N. *et al.* Surface hydride composition of plasma-synthesized si nanoparticles. *J. Phys. Chem. C* **115**, 20375–20379 (2011).
216. Lucovsky, G. Chemical effects on the frequencies of Si-H vibrations in amorphous solids. *Solid State Commun.* **29**, 571–576 (1979).
217. Sénémaud, C. *et al.* Local order and H-bonding in N-rich amorphous silicon nitride. *J. Non. Cryst. Solids* **164–166**, 1073–1076 (1993).

218. Ledoux, G., Gong, J. & Huisken, F. Effect of passivation and aging on the photoluminescence of silicon nanocrystals. *Appl. Phys. Lett.* **79**, 4028–4030 (2001).
219. Wolkin, M. M., Jorne, J., Fauchet, P., Allan, G. & Delerue, C. Electronic States and Luminescence in Porous Silicon Quantum Dots: The Role of Oxygen. *Phys. Rev. Lett.* **82**, 197–200 (1999).
220. Wallace, R. M. & Wei, Y. Dry oxidation resistance of ultrathin nitride films: Ordered and amorphous silicon nitride on Si(111). *J. Vac. Sci. Technol. B* **17**, 970–977 (1999).
221. Yoshimaru, M., Inoue, N., Tamura, H. & Ino, M. Effects of Deposition Temperature on the Oxidation Resistance and Electrical Characteristics of Silicon Nitride. *IEEE Trans. Electron Devices* **41**, 1747–1752 (1994).
222. Suzuki, E., Hiraishi, H., Ishii, K. & Hayashi, Y. Carrier conduction in thin silicon nitride films. *Appl. Phys. Lett.* **40**, 681–683 (1982).
223. Maillot, C., Roulet, H. & Dufour, G. Thermal nitridation of silicon: An XPS and LEED investigation. *J. Vac. Sci. Technol. B* **2**, 316–319 (1984).
224. Schulz, A. *et al.* Surface passivation of silicon with the Plasmodul. *Surf. Coatings Technol.* **142–144**, 771–775 (2001).
225. Suzuki, N., Cervera, R. B., Ohnishi, T. & Takada, K. Silicon nitride thin film electrode for lithium-ion batteries. *J. Power Sources* **231**, 186–189 (2013).
226. Jousse, D., Kanicki, J. & Stathis, J. H. Observation of multiple silicon dangling bond configurations in silicon nitride. *Appl. Phys. Lett.* **54**, 1043–1045 (1989).
227. Pereira, R. N., Rowe, D. J., Anthony, R. J. & Kortshagen, U. Oxidation of freestanding silicon nanocrystals probed with electron spin resonance of interfacial dangling bonds. *Phys. Rev. B* **83**, 1–9 (2011).
228. Warren, W. L., Robertson, J. & Kanicki, J. Si and N dangling bond creation in silicon nitride thin films. *Appl. Phys. Lett.* **63**, 2685–2687 (1993).
229. Židek, K. *et al.* Femtosecond luminescence spectroscopy of core states in silicon nanocrystals. *Opt. Express* **18**, 25241–9 (2010).
230. Mittal, R., Glenn, R., Saytashev, I., Lozovoy, V. V. & Dantus, M. Femtosecond nanoplasmonic dephasing of individual silver nanoparticles and small clusters. *J. Phys. Chem. Lett.* **6**, 1638–1644 (2015).
231. Mahdavi, A. *et al.* Maximizing Photoluminescence Extraction in Silicon Photonic Crystal Slabs. *Sci. Rep.* **6**, 1–6 (2016).
232. Iwamoto, S., Arakawa, Y. & Gomyo, A. Observation of enhanced photoluminescence from silicon photonic crystal nanocavity at room temperature. *Appl. Phys. Lett.* **91**, 10–13 (2007).
233. Zelsmann, M. *et al.* Seventy-fold enhancement of light extraction from a defectless

- photonic crystal made on silicon-on-insulator. *Appl. Phys. Lett.* **83**, 2542–2544 (2003).
234. Chernow, V. F., Alaeian, H., Dionne, J. A. & Greer, J. R. Polymer lattices as mechanically tunable 3-dimensional photonic crystals operating in the infrared. *Appl. Phys. Lett.* **107**, 1–5 (2015).
  235. Yu, H. *et al.* Low-Temperature STM Images of Methyl-Terminated Si (111) Surfaces. *J. Phys. Chem. B* **109**, 671–674 (2005).
  236. Royea, W. J., Juang, A. & Lewis, N. S. Preparation of air-stable, low recombination velocity Si(111) surfaces through alkyl termination. *Appl. Phys. Lett.* **77**, 1988–1990 (2000).
  237. Bansal, A., Li, X., Yi, S. I., Weinberg, W. H. & Lewis, N. S. Spectroscopic studies of the modification of crystalline si(111) surfaces with covalently-attached alkyl chains using a chlorination/alkylation method. *J. Phys. Chem. B* **105**, 10266–10277 (2001).
  238. Lewis, N. S., Plass, K. E., Liu, X. & Brunshwig, B. S. Passivation and secondary functionalization of allyl-terminated Si(111) surfaces. *Chem. Mater.* **20**, 2228–2233 (2008).
  239. Nemanick, E. J. *et al.* Chemical and Electrical Passivation of Single-Crystal Silicon ( 100 ) Surfaces through a Two-Step Chlorination / Alkylation Process. *J. Phys. Chem. B* **110**, 14770–14778 (2006).
  240. Webb, L. J., Rivillon, S., Michalak, D. J., Chabal, Y. J. & Lewis, N. S. Transmission infrared spectroscopy of methyl- and ethyl-terminated silicon(111) surfaces. *J. Phys. Chem. B* **110**, 7349–7356 (2006).
  241. Amy, S. R. *et al.* Investigation of the reactions during alkylation of chlorine-terminated silicon (111) surfaces. *J. Phys. Chem. C* **111**, 13053–13061 (2007).
  242. Cui, C. & Goree, J. Fluctuations of the charge on a dust grain in a plasma. *IEEE Trans. Plasma Sci.* **22**, 151–158 (1994).
  243. Fridman, A. A., Boufendi, L., Hbid, T., Potapkin, B. V. & Bouchoule, A. Dusty plasma formation: Physics and critical phenomena. Theoretical approach. *J. Appl. Phys.* **79**, 1303–1314 (1996).
  244. Perrin, J., Böhm, C., Etemadi, R. & Lloret, A. Possible routes for cluster growth and particle formation in RF silane discharges. *Plasma Sources Sci. Technol.* **3**, 252–261 (1994).
  245. Hollenstein, C. *et al.* Anionic clusters in dusty hydrocarbon and silane plasmas. *J. Vac. Sci. Technol. A* **14**, 535–539 (1996).
  246. Howling, A. A., Sansonnens, L., Dorier, J.-L. & Hollenstein, C. Negative hydrogenated silicon ion clusters as particle precursors in RF silane plasma deposition experiments. *J. Phys. D Appl. Phys.* **26**, 1003–1006 (1993).

247. Girshick, S. L. Theory of nucleation from the gas phase by a sequence of reversible chemical reactions. *J. Chem. Phys.* **107**, 1948–1952 (1997).
248. Rao, N. *et al.* Nanoparticle formation using a plasma expansion process. *Plasma Chem. Plasma Process.* **15**, 581–606 (1995).
249. Rao, N. *et al.* Synthesis of nanophase silicon, carbon, and silicon carbide powders using a plasma expansion process. *J. Mater. Res.* **10**, 2073–2084 (1995).
250. Parikh, R. P. & Adomaitis, R. A. An overview of gallium nitride growth chemistry and its effect on reactor design: Application to a planetary radial-flow CVD system. *J. Cryst. Growth* **286**, 259–278 (2006).